Laser Cooling and Magneto-Optical Trapping of Diatomic Metal Hydrides and Deuterides

Jinyu Dai

Submitted in partial fulfillment of the
requirements for the degree of
Doctor of Philosophy
under the Executive Committee
of the Graduate School of Arts and Sciences

COLUMBIA UNIVERSITY

2026

Abstract

Laser Cooling and Magneto-Optical Trapping of Diatomic Metal Hydrides and Deuterides

Jinyu Dai

Laser cooling plays an important role in modern atomic, molecular, and optical physics. Since its first demonstration, it has initiated a variety of research directions in quantum science and technology. The first Bose-Einstein condensate, multiple platforms for quantum simulation and computation, ultracold quantum chemistry, and high-precision measurements of fundamental constants, all rely on the ability to cool atoms to temperatures near absolute zero. However, laser cooling has long been limited to atoms, and molecular laser cooling techniques have only been developed in the past decade. In this thesis, I describe the extension of these techniques to a new class of molecules: diatomic metal hydrides. We demonstrate one-dimensional laser cooling of calcium monohydride (CaH) molecules and characterize their unique predissociative loss channels. With an optimal laser cooling scheme, efficient laser slowing is realized and a three-dimensional magneto-optical trap (MOT) of CaH is created. Future improvements of the MOT and prospects for cooling to ultracold temperatures are discussed. With a proposed coherent dissociation pathway, ultracold atomic hydrogen could be produced with even colder temperatures than the parent CaH molecules, potentially enabling optical trapping of hydrogen for precision spectroscopy. Additionally, given its relatively low number of electrons, CaH is one of the first molecules that could be treated fully quantum mechanically in computational quantum chemistry. Ultracold CaH is a powerful platform to benchmark such theoretical frameworks. Finally, I describe how a similar approach can be implemented for its fermionic isotopologue, calcium monodeuteride (CaD). One-dimensional laser cooling of the fermionic CaD is demonstrated for the first time.

Table of Contents

List of Figures vi

List of Tables xvi

Acknowledgments xviii

Dedication xxii

Chapter 1: Introduction 1

1.1 Why Cold Molecules 1

1.1.1 Precision Measurements 1

1.1.2 Cold and Ultracold Chemistry 3

1.1.3 Quantum Simulation and Computation 3

1.2 Production of Cold and Ultracold Molecules 4

1.2.1 Indirect Methods 4

1.2.2 Direct Methods 5

1.3 Ultracold Molecules for Exotic Ultracold Atoms 6

1.3.1 Hydrogen Spectroscopy 6

1.3.2 Ultracold CaH for Ultracold Hydrogen 7

1.4 This Thesis 9

Chapter 2: The Molecular Laser Cooling Technique 10
2.1 Diatomic Molecular Structure 10
2.1.1 Electronic Energy Levels 10
2.1.2 Vibrational Energy Levels 12
2.1.3 Rotational Energy Levels 12
2.1.4 Fine Structure, Spin-Rotation Coupling, and Hyperfine Structure 13
2.2 Laser Cooling Scheme 15
2.2.1 Vibrational Branching 15
2.2.2 Rotational Branching 16
2.3 Reference Tables for CaH Laser Cooling 18

Chapter 3: Cryogenic Buffer Gas Beam Source 21
3.1 CaH_2-Based Beam Source 21
3.1.1 Buffer Gas Cell 22
3.1.2 He Flow Dependence 24
3.1.3 Ablation Protocol 26
3.1.4 Two-Stage Cell 26
3.2 Chemical Production 27
3.2.1 Cell Design 29
3.2.2 Ca + H_2 Reaction 30
3.2.3 Rotational Temperature 32
3.2.4 Theoretical Interpretation 33
3.2.5 H_2 as a Buffer Gas Coolant 38

3.2.6 Collisional Cross Sections 40

3.3 Beam Source Comparison 41

Chapter 4: Laser Cooling of CaH 44

4.1 Relevant Experimental Hardware 44

4.1.1 Laser Systems 44

4.1.2 Beamline 45

4.2 FCF and VBR Measurements 46

4.3 Scattering Rate Measurement 48

4.4 Magnetically Assisted Sisyphus Cooling 52

Chapter 5: Predissociative Loss of CaH 56

5.1 Theoretical Model 58

5.1.1 Calculation of Molecular Potential Energies 58

5.1.2 Calculation of FCFs 59

5.1.3 $B^2\Sigma^+$ Predissociation Estimate 60

5.2 $B^2\Sigma^+$ Predissociation Measurement 60

5.2.1 $B^2\Sigma^+$ ($v' = 0$) Predissociation Measurement Method 62

5.2.2 $B^2\Sigma^+$ ($v' = 1$) Predissociation Measurement Method 62

5.2.3 Predissociation Measurement Analysis 63

5.2.4 Details of the Measurement Stages 66

5.3 $A^2\Pi_{1/2}$ Predissociation Estimate 68

5.4 Does Predissociation Limit Us? 69

Chapter 6: Laser Slowing of CaH 75
6.1 Relevant Experimental Hardware 75
6.1.1 Laser Systems 75
6.1.2 Ultrahigh Vacuum System 79
6.2 Two-Photon Background-Free Velocity Detection 82
6.3 White-Light Laser Slowing 84

Chapter 7: Magneto-Optical Trapping of CaH 90
7.1 Relevant Experimental Hardware 90
7.1.1 Laser Systems 90
7.1.2 Radio-Frequency MOT Configuration 91
7.2 To Observe a MOT Effect 93
7.2.1 $A^2\Pi_{1/2}(v = 0,\ J = 1/2,\ +)$ Hyperfine Splitting 94
7.2.2 MOT Force on the Molecular Beam 95
7.3 3D MOT of CaH 97
7.3.1 MOT Lifetime and Predissociation 99
7.3.2 MOT Characterization 100
7.4 Further Cooling and Trapping 102
7.4.1 Improvements on Slowing 102
7.4.2 Blue-Detuned MOT and Optical Dipole Trapping 104
7.4.3 To Improve the Overall Yield 105

Chapter 8: Extension to the Fermionic Isotopologue CaD 107
8.1 Why CaD 107

8.2 Synthesis of CaD_2 . . . 108

8.3 1D Cooling with MOT Chamber as Beamline . . . 110

8.4 Magnetically Assisted Sisyphus Cooling of CaD . . . 114

8.4.1 Characterization of the Sisyphus Effect . . . 116

8.4.2 Beam Temperature Estimation . . . 117

8.5 Doppler Cooling of CaD . . . 118

Chapter 9: Conclusion and Outlook . . . 119

References . . . 121

List of Figures

1.1 Proposed approach for producing ultracold hydrogen. CaH molecules are first laser cooled and trapped, followed by near-threshold dissociation to produce hydrogen atoms at ultracold temperatures. 8

2.1 Relevant Hund's cases in this thesis. The lowest excited $A^2\Pi_{1/2}$ state of CaH is described by Hund's case (a) as shown on the left, and the ground electronic state is described by Hund's case (b) on the right. The second excited $B^2\Sigma^+$ state is also described by Hund's case (b). 14

2.2 A vibrationally quasi-closed scheme in CaH. For molecules with diagonal FCFs like CaH, branching to higher vibrational states are suppressed exponentially. Two to three vibrational repump lasers are typically enough to achieve a photon budget of $\sim 10^4$–10^5. 16

2.3 Rotational closure for the $A^2\Pi_{1/2}(v' = 0) \leftarrow X^2\Sigma^+(v = 0)$ and $B^2\Sigma^+(v' = 0) \leftarrow X^2\Sigma^+(v = 0)$ transitions, shown as examples. Note that the spin-rotation and hyperfine splittings are slightly different for different vibrational states and need to be treated carefully. Hyperfine splittings for the excited states are expected to be unresolved within the MHz level. However, we do measure an 18 MHz splitting in the $A^2\Pi_{1/2}(v' = 0,\ J' = 1/2,\ +)$ state. This is very important in the context of a MOT and is discussed in more detail in the corresponding chapter. 17

3.1 (a) Schematic of the cryogenic buffer gas cell for the production of a CaH molecular beam. CaH molecules are generated through a pulsed Nd:YAG laser ablation on a CaH_2 target. The hot CaH molecules are then buffer gas cooled with He at ~6 K and extracted from the cell to form a molecular beam. The molecule production in cell can be monitored with laser absorption. (b) Image of a cell. (1) the aperture for molecular beam extraction; (2) a small window for the probe laser; (3) a snorkel to hold the window for the ablation laser; and (4) the gas fill line. 23

3.2 (a) LIF on the $4s4p\ ^1P_1 \leftarrow 4s^2\ ^1S_0$ transition of Ca at different velocities detected on a PMT, measured with 17.6 SCCM He flow rate and 12 mJ YAG ablation energy. The solid white line marks ballistic propagation from the cell and serves as a guide to the eye. (b) Normalized time-integrated LIF as a function of velocity at different He flow rates. An increase in the peak forward velocity is observed with increasing in He flow rate. 24

3.3 (a) Schematic of the two-stage cell. Before the second-stage cell, there exists a small gap to reduce the He density. The molecules then get further thermalized in the second stage and extracted to form a molecular beam in the effusive regime (b) Image of the design. (1) the target holder; (2) a small window for the probe laser; (3) the second-stage cell; and (4) the window for the ablation laser. 27

3.4 Velocity performance with two-stage cell. With increasing He flow rate, very minimal peak velocity change is observed, signaling the output molecular beam in the effusive regime. 28

3.5 Horizontal cross section of the buffer gas cell modified for chemical production. An thermally isolated gas fill line is added to the back of the cell, where we can flow in various reactants such as H_2, D_2, and HD. Hot Ca atoms are generated via laser ablation of a solid Ca target and subsequently react to form CaH or CaD. Additionally, He flows in at ~6 K for efficient buffer gas cooling. The Ca atoms and the product molecules are probed through laser absorption. 29

3.6 Chemical reaction in the buffer gas cell. Time-averaged CaH densities measured within 0–1 ms after ablation, plotted against Ca density for 10 SCCM of H_2 (red circles) and 20 SCCM of H_2 (blue squares), both under 2.2 SCCM of He. The lines denote theoretical results at the same conditions at a collision temperature of 2400 K, showing qualitative agreement. The inset shows the reaction efficiency, defined as the ratio of CaH to Ca densities. A notable decrease in reaction efficiency is observed experimentally at higher Ca densities, whereas the theoretical model does not capture this trend, showing the need for further refinement. Error bars on the experimental data correspond to 1-σ statistical uncertainties. 30

3.7 (a) Relative in-cell absorption for $X^2\Sigma^+(N = 0)$ and $X^2\Sigma^+(N = 2)$ states with respect to $X^2\Sigma^+(N = 1)$, versus ablation pulse energy. Absorption for $X^2\Sigma^+(N = 3)$ and higher rovibrational states is below the detection limit and therefore neglected. Solid lines are fitted quadratic functions to guide the eye. (b) Fitted rotational temperature versus ablation pulse energy. Temperatures are extracted from a least-squares fit according to Eq. (3.1), as shown in inset (c). The wide green band represents the 2-σ uncertainties from the fit. 32

3.8 (a) QCT calculated temperature-dependent state-to-state vibrational rate constants for H_2 ($k^q_{v\to v'}$), where the subscripts denote the initial and final vibrational states, and formation of CaH (k^r_v), where the subscript denotes the initial vibrational state of H_2. (b) Sample solution to the reaction model at 2400 K showing the change in number density over time relative to the initial densities. The Ca and CaH densities are scaled up by a factor of 500 for visualization. (c) Kinetic temperature of Ca over time, decaying due to elastic collisions with buffer gases H_2 and He. 35

3.9 (a) Ca absorption spectra at different ablation energies. The data is fitted with the Gaussian function. (b) The Ca plume temperature versus ablation energy (error bars not visible at this scale). The gray shaded area represents the theoretical temperature 2400(60) K that optimally matches the experimental results in Fig. 3.6. 37

3.10 Time-averaged densities (0–1 ms after ablation) of Ca and CaH (or CaD) under different gas flow configurations. Reactant gases H_2, HD, or D_2 are supplied at 20 SCCM, with He (if used) added at 8.8 SCCM. Ablation energy is 19 mJ per pulse. Green, yellow, and red bars represent results for H_2, HD, and D_2, respectively, while black-framed bars show the yields with He added. Dashed lines indicate the detection limits, defined as the lowest density detectable with SNR > 2, below which measurements are statistically consistent with zero. Relative errors are larger when signals are close to the detection limit. Here the measured densities of CaH and CaD are those in the $X^2\Sigma^+(v = 0,\ N = 1,\ J = 1/2,\ -)$ states. . . . 39

3.11 (a) A Ca density trace as a function of time after the ablation pulse (average of 30 shots). The blue curve is the original data, the orange line highlights the data used for fitting, and the green dashed line indicates the fitted single exponential decay result. This data is obtained with 8.8 SCCM He flow. (b) Measured collisional cross sections of He, H_2, HD, and D_2 with Ca and CaH. 41

3.12 CaH_2-based and chemically produced source detected in cell and in beam. (a) CaH density measured with laser absorption in cell. Chemically produced CaH shows a faster extraction. (b) In-beam LIF measured ∼1 m downstream from the cell. 42

4.1 (a) Schematic for the 1D cooling experiment. CaH molecules are produced via ablation of a solid target of CaH_2. The ejected molecules thermalize to the ∼ 6 K He buffer gas and are extracted through a 3 mm diameter aperture. An additional 5 mm aperture is placed just before the molecular beam enters the interaction region to limit the transverse velocity distribution. The cooling chamber consists of 12 cm of optical access followed by a cleanup region and a detection region. (b) A sample image of molecules in the beam taken with the EMCCD camera. Photons are collected for 7 ms during imaging. Arrow indicates the direction of the molecular beam. 46

4.2 Measurement of the VBRs for CaH molecules. (a) An example of PMT traces used to calculate the VBRs. These two time traces correspond to background-subtracted fluorescence from the decay to $X(v'' = 0)$ for PMTs P_1 (orange, dashed) and P_2 (blue, solid) while the $B^2\Sigma^+(v' = 0) \leftarrow X^2\Sigma^+(v'' = 0)$ transition is excited. The cell was performing suboptimally during this data taking, the molecular beam velocity is faster at ~400 m/s, leading to an earlier arrival time. The inset denotes how the ratio of integrated signals, R_0, is computed. We perform a one-parameter fit of the dashed trace to the solid trace. The result of the fit produces the orange points that can be seen to overlap temporally with the blue trace. (b)–(c) The resulting VBRs from the measured ratio $R_{v''}$, obtained by evaluating Eq. (4.3), for the A and B states. Each point represents an average of at least 200 shots with background subtraction, while the higher vibrational decays require ~700 shots for an appreciable SNR due to the low probability of decaying to these excited states. Error bars are statistical standard errors. 48

4.3 Scattering rate measurement. The fraction of molecules remaining in the $X(v'' = 0)$ state when cycling on the $A(v' = 0) \leftarrow X(v'' = 0)$ transition (orange circles) and the fraction remaining in $X(v'' = 0) + X(v'' = 1)$ states when cycling simultaneously on the $A(v' = 0) \leftarrow X(v'' = 0)$ and the $B(v' = 0) \leftarrow X(v'' = 1)$ transitions (blue squares) are measured as a function of the interaction time. Lines are fits to exponential decay curves with finite offsets. The offset is due to detected molecules that are only weakly addressed in the interaction region. The exponential decay time constant τ from the fit is $5.5(3) \times 10^4\ s^{-1}$ for the orange curve and $3.92(13) \times 10^3\ s^{-1}$ for the blue curve. 51

4.4 Magnetically assisted Sisyphus effect in CaH. (a) Molecular beam profiles obtained for an unperturbed beam (green), Sisyphus cooled beam (purple) at $\delta = +20$ MHz, and Sisyphus heated beam (blue) at $\delta = -20$ MHz. The y-axis is normalized to the unperturbed beam maximum and no other scale factors are used. Lines are fits to a 1D Gaussian function to obtain the $1/e$ cloud radius σ. The increase in on-axis molecule number seen in the cooling configuration is a clear signature of Sisyphus cooling. Statistical error for each point is represented by the bar on top right and is depicted separately for clarity. (b) Change in σ as a function of detuning, where $\Delta\sigma > 0$ implies heating and vice versa. The detuning is applied globally to each spin-rotation and hyperfine addressing lasers. The data was taken at an intensity of 200 mW/cm^2. The band represents the result of OBE and MC simulations for our experimental system. (c) Change in beam size $\Delta\sigma$ as a function of laser intensity. Detuning has been fixed at $\delta = +20$ MHz. We do not saturate the Sisyphus cooling effect even at the largest available laser intensity (∼300 mW/cm^2). The simulations shown as a band suggest that an intensity of >600 mW/cm^2 is required for saturation. (d) Change in beam size $\Delta\sigma$ as a function of magnetic field strength. Detuning is $\delta = +20$ MHz and intensity is 200 mW/cm^2. Maximum cooling is seen for $B \approx 1$ G. Note that the scattering rate is maximized at $B \approx 3$ G. The Sisyphus effect is expected to be nulled at $B = 0$, but due to the presence of the Earth's magnetic field and the low laser intensity we do not resolve the dip. The simulation shows the same behavior. The bands shown in simulations encompass the spatial variation in laser intensity we expect in the experiment. Each point is a result of 200 repetitions of the experiment, and the experimental error bars are standard errors of Gaussian fitting. 54

5.1 (a) PES for the 4 lowest electronic states of CaH: $X^2\Sigma^+$, $A^2\Pi$, $B^2\Sigma^+$, and $D^2\Sigma^+$. Spin-orbit interaction is omitted. The x-axis is the internuclear separation r in Bohr radii (a_0) and the y-axis is energy in cm^{-1} (1 cm^{-1} ≈ 30 GHz). The energy origin is chosen as the Ca(^1S)+H(^2S) continuum threshold (ν_{th}). Superimposed are the wavefunctions (bottom to top) for the $X(\nu'' = 0)$ absolute ground state, $X(\nu'' = 15)$ least-bound state, and $B(\nu' = 4)$ excited state. (b) Experimental layout for predissociation measurement. The CaH molecular beam encounters 4 spatially separated regions: state preparation (S), interaction (I), cleanup (C), and detection (D). Each region includes multipassed lasers described in the text. The diagram is not aligned to scale. (c) Relevant VBRs (squiggly arrows) calculated for the $B^2\Sigma^+$ state. The hyperfine structure of the excited states is unresolved. Measured predissociation probabilities for $B(\nu' = 0)$ and $B(\nu' = 1)$ are denoted by dashed lines. 57

5.2 Illustration of the ratio extraction process for the $B^2\Sigma^+$ ($v' = 0$) predissociation measurement. We run the stages sequentially with an interlaced reference stage, and collect LIF with an EMCCD. We integrate the images along both axes to obtain the signals, which we then used to calculate ratios. By repeating the entire sequence N times, we collect N sets of five ratios. Here we first show examples of one-shot camera images. We then present the integrated signal along one axis, using colored traces for science stages and black for reference stages (horizontal lines are the baselines). Finally we show the histograms of the five ratios. Vertical dashed lines represent the means of the ratios. 64

5.3 CaH predissociation. Red squares are theoretical results for nonradiative decay rates of different vibrational states of $B^2\Sigma^+$. Blue circles are experimental results, where error bars represent the 95% confidence interval. 65

6.1 Slowing lasers modulated by different EOMs detected on a FPC. (a) The ($v = 0$) cycling laser modulated by a 947.1 MHz spin-rotation EOM and a 50.83 MHz hyperfine EOM. Periodic structure arises from the 1.5 GHz FSR of the FPC. (b) The ($v = 0$) cycling laser modulated by a white-light (WL) EOM operating at 4.335 MHz and a 50.83 MHz hyperfine EOM. 77

6.2 Optical path layout for slowing lasers. Different EOMs are used to generate the frequency sidebands for spin-rotation splitting, hyperfine splitting, and WL. This figure is reproduced from Ref. [137], with corrected frequencies and order of the acousto-optic modulator (AOM). 79

6.3 Pictures of the MOT chamber. (a) In-vacuum MOT coils after painted. Molecules travel through the middle of the two plates, which are spaced by 1 inch. The spiral in the middle of the plate is the coil, and the elliptical holes are for optical access of the small windows on the chamber. The MOT coils are thermally connected to outside the vacuum through the holding structure. (b) Kimball Physics chamber. (c) During assembly, a picture from a different angle of the MOT coil for a better vision of the structure. 80

6.4 In-vacuum lens for higher photon collection efficiency. Top is a rough drawing of how the lens is mounted. The coil and lens holder designs are modified slightly for the final version used in the experiment. Bottom is a picture after the lens was installed. 81

6.5 Two-photon BGF velocity measurement. (a) Measurement scheme. The molecules are excited with two lasers, with the first addressing an $A \leftarrow X$ transition, and the second addressing an $E \leftarrow A$ transition. The LIF of the decay from the E state back to X state at ~490 nm is detected on a PMT. (b) Spectrum of the $E^2\Pi_{1/2}(v' = 0,\ J' = 3/2,\ -) \leftarrow A^2\Pi_{1/2}(v = 0,\ J = 3/2,\ +)$ transition. Hyperfine structure remains unresolved at this precision. (c) A sample velocity measurement of the chemically produced CaH molecular beam, with the $E \leftarrow A$ laser applied in a velocity sensitive configuration (45°with respect to the molecular beam in this measurement). LIF from the $E \rightarrow X$ decay detected on a PMT. x-axis is the time of arrival on the PMT, while y-axis is the velocity group selected with detuning from the $E \leftarrow A$ transition. Solid white line is a guide to eye of a ballistic propagation from the cell to the detection region. 83

6.6 Beam velocity with double ablation. (a) Measured forward velocity of the CaH molecular beam with single and double ablation. The prefire time for double ablation is 20 ms. An improvement of molecule number in the 100–200 m/s velocity group is observed with double ablation. (b) Arrival time of the molecules detected through LIF on the slowing lasers. Later arrival time with double ablation also indicates a slower velocity. 85

6.7 Laser slowing with full (free-space) and 60% (fiber coupled) of power. (a) Differential LIF (unperturbed molecular beam subtracted from slowed molecular beam) with free-space slowing lasers. With laser slowing, a substantial molecule population is observed with low velocities (red region). (b) Differential LIF with fiber coupled slowing lasers. (c) Time-integrated LIF at different velocities for the two configurations. (d) Differential (unperturbed subtracted from slowed) time-integrated LIF for the two configurations. 88

6.8 Laser slowing measured in the MOT region. (a) Differential LIF obtained by subtracting the unperturbed molecular beam from the slowed molecular beam. Decent slowing effect is observed. (b) Time-integrated LIF at different velocities. With laser slowing, molecules near zero velocity are observed, as in the inset. 89

7.1 Optical path layout for MOT lasers. We use a 650 MHz AOM, a double-passed 342 MHz AOM, and a double-passed 272 MHz AOM to cover the spin-rotation splitting. The 82 MHz and 53.2 MHz AOMs are for the hyperfine splittings. This figure is reproduced from Ref. [137], with corrected frequencies and AOM orders. . 91

7.2 (a) Schematic of the MOT experiment. CaH molecules are generated with a CBGB source at ∼6 K, and they are subsequently laser slowed and reach the MOT region to be trapped. (b) Laser configuration for the MOT. At a certain magnetic field gradient, the polarization for the ($J = 1/2$) and ($J = 3/2$) states are orthogonal because of the opposite g-factors. The $A^2\Pi_{1/2}(v = 0,\ J = 1/2,\ +)$ state has a hyperfine splitting $\delta_A \approx 18$ MHz. (c) Radio-frequency MOT configuration. Trapping and anti-trapping can be achieved by tuning the relative phase between the magnetic field gradient and the polarization of the MOT lasers. 92

7.3 Measurement of the $A^2\Pi_{1/2}(v = 0,\ J = 1/2,\ +)$ hyperfine splitting. (a) Spectroscopy with laser at around the $A^2\Pi_{1/2}(v' = 0,\ J' = 1/2,\ +) \leftarrow X^2\Sigma^+(v = 0,\ N = 1,\ J = 1/2,\ -)$ transition. (b) Spectroscopy with laser at around the $A^2\Pi_{1/2}(v' = 0,\ J' = 1/2,\ +) \leftarrow X^2\Sigma^+(v = 0,\ N = 1,\ J = 3/2,\ -)$ transition. According to the fit, the $A^2\Pi_{1/2}(v = 0,\ J = 1/2,\ +)$ hyperfine splitting $\delta_A \approx 18$ MHz. 95

7.4 MOT compression on the molecular beam. The orange and green trace show the LIF of the MOT lasers in the MOT and antiMOT configurations. A change in LIF is observed, indicating a MOT compression force on the molecular beam. 96

7.5 "2D MOT" effect as a function of (a) MOT laser detuning and (b) relative phase between the Pockels cell and the magnetic field gradient. 97

7.6 MOT LIF measured on PMT and EMCCD camera. The PMT data are taken in three configurations: slowing only (gray), MOT (red), and antiMOT (blue). The existence of molecules after the molecular beam flying by demonstrate a successful magneto-optical trapping. Insets show the camera images of the MOT and antiMOT, integrating from 25 to 55 ms after ablation. The images are smoothed with a Gaussian filter of 0.6 mm standard deviation. 98

7.7 MOT lifetime measurement. (a) LIF of the antiMOT configuration subtracted from that of the MOT configuration. The tail of the resulting time trace can be fitted to an exponential day, from which $1/e$ MOT lifetime can be extracted. (b) $1/e$ MOT lifetime as a function of MOT laser power. Lifetime of ∼30 ms is achieved with a few milliwatts of MOT laser power per beam. 99

7.8 MOT trapping and cooling force measurement. The MOT is pushed by the slowing laser for 0.5 ms after thermalized. The resulting oscillation of MOT position is measured. (ii)–(v) are sample camera images of the MOT at 3.5, 9, 13, and 16 ms after the push, while (i) represents the unperturbed MOT position. The images are smoothed with a Gaussian filter of 0.6 mm standard deviation and normalized to the same scale for better visualization. Error bars represent 1-σ uncertainties. From the fit, $\omega = 2\pi \times 48(3)$ Hz and $\beta = 510(110)$ s^{-1}. 101

7.9 MOT size and temperature measurements. Geometric mean MOT size is measured as a function of MOT laser power. An increase in the MOT size at higher laser power due to a stronger sub-Doppler heating is observed. The temperature of the MOT is measured at two characteristic powers using the release-and-recapture method. 102

7.10 Schematic of the AOM-based polarization switching setup. With an appropriate AOM control sequence, the design shown here is compatible for both rf MOT and dc blue-detuned conveyor-belt MOT. 104

8.1 Synthesis of CaD_2. (a) Illustration of the home-built setup used for the synthesis. The main reactor is a standard CF 2.75", 5" long 304 stainless steel nipple. The base is wrapped with heating tape connected to a variac via a temperature controller (Extech 48VFL). A standard J-type thermocouple attached to the base is used for temperature stabilization. A high-pressure gauge (MG1-100-A-9V-R) is placed close to the top of the reactor. All connections henceforth are VCR type. The reactor connects to a scroll pump and a Convectron gauge (MKS 275) via a tee. The other end of the tee connects to a D_2 cylinder using a long flexible hose. The regulator on the cylinder allows for control of the charging pressure, while the valves shown are used to direct the flow. (b) Pressure measured on the high-pressure gauge as a function of time at 450 °C. The reactor contains 3 g of Ca pieces. From an exponential fit, we obtain a reaction rate of $k = 0.11$ min^{-1}. (c) Powder x-ray diffraction study of the resulting sample. Red lines are the known CaD_2 peaks. Almost all measured peaks match with the known CaD_2 values except for the peak at $2\theta = 37°$. This peak could be attributed to CaO or $Ca(OH)_2$, possibly resulting from short contact with air. The results suggest very high conversion efficiency from Ca to CaD_2. 109

8.2 (a) Schematic of the experiment viewed from above. CaD molecules are generated in a ∼6 K CBGB source. The molecular beam is collimated by a 2.5 mm diameter aperture and enters the interaction region where it is addressed by the main cooling laser, copropagating with the ($v = 1$) repump laser. The laser beam is expanded to (10.8 mm × 5.4 mm) $1/e^2$ diameter and retroreflected to form a standing wave. The molecules then enter the clean-up region where only the ($v = 1$) repump laser is applied in a multipass configuration and are finally detected in the ($v = 0$) state. (b) Level structure of the main cycling transition $A^2\Pi_{1/2}(v' = 0,\ J' = 1/2,\ +) \leftarrow X^2\Sigma^+(v'' = 0,\ N'' = 1,\ -)$. The hyperfine splittings are adapted from Ref. [186]. (c) In-beam spectroscopy of the transition. The inset shows signal enhancement with rotational closure. 111

8.3 Molecular-beam profile with Sisyphus cooling and heating. (a)–(c) Beam images under unperturbed, Sisyphus cooling at +40 MHz, and Sisyphus heating at −40 MHz configurations, respectively. (d) Integrated 1D profile. Sisyphus cooling narrows the width of the center of the molecular beam (blue), while Sisyphus heating expels molecules away from the center (red). Unperturbed beam is shown as gray. Solid lines show the fits to the beam profile. 115

8.4 Parameter scans of the Sisyphus effect. (a) Peak height change as a function of the main laser detuning, taken with magnetic field $|\vec{B}| = 1.7$ G and at 45° with respect to laser polarization. (b) Sisyphus cooling (blue circles) and heating (red squares) as a function of the main laser intensity, taken at ±40 MHz detuning and the same magnetic field configuration as in (a). Saturation is not observed. The gray lines are guides to the eye for the unperturbed scenario (horizontal) and zero detuning [vertical in (a)]. (c) Sisyphus cooling (blue circles) and heating (red squares) as a function of applied magnetic field, taken at ±40 MHz detuning and maximum laser intensity. A sharp decrease in the strength of Sisyphus effect is observed when $|\vec{B}| \approx 0$. Error bars represent the 95% confidence intervals. 116

8.5 Doppler cooling and heating as a function of laser detuning, A change in the molecular-beam width demonstrates Doppler cooling (negative) and heating (positive). Error bars represent the 95% confidence intervals. 118

9.1 Suggested controlled dissociation pathway for CaH molecules. Line strengths ($S_{v'v''}$) in atomic units for dipole allowed transitions: (a) $X^2\Sigma^+$ (v'') $\rightarrow A^2\Pi_{1/2}$ (v') and (b) $X^2\Sigma^+$ (v'') $\rightarrow B^2\Sigma^+$ (v'). The A state potential is more harmonic as is reflected by the diagonal $S_{v'v''}$. The B state, however, significantly deviates from the diagonal starting around $v' = 4$ because of the second potential minimum at ∼6 a_0 [Fig. 5.1(a)]. Note that $B(v' = 4)$ has comparable line strengths between $X(v'' = 0)$ and $X(v'' = 15)$. (c) Intensity-normalized Rabi rate ($\Omega/\sqrt{I} = \sqrt{S_{v'v''}}/\hbar$) for dipole transitions $X(v'' = 0) \rightarrow B(v')$ (red squares) and $B(v') \rightarrow X(v = 15)$ (blue circles). Around $v' = 4$ (shaded points), the Rabi rates are comparable. (d) Wavelengths in nanometers for optical transitions $X(v'' = 0) \rightarrow B(v')$ (blue circles) and $B(v') \rightarrow X$(continuum) (red squares). The theoretical energy differences were adjusted by a common offset of 240 cm^{-1} to match experimental data for $X(v'' = 0) \rightarrow B(v' = 0,\ 1,\ 2)$ transitions [108]. The wavelengths corresponding to $v' = 4$ (shaded points) are 512.7 nm and 1744.7 nm. 120

List of Tables

2.1 State notations for atoms and molecules, reproduced from Ref. [104]. 11

2.2 FCFs and VBRs with excited state vibrational quantum number $v' = 0$. The experimental radiative lifetime τ for the A state was obtained from Ref. [106] and for the B state from Ref. [107]. In this table, the transition wavelengths of $A(v' = 0) \leftarrow X(v = 0)$, $B(v' = 0) \leftarrow X(v = 0)$, and $B(v' = 0) \leftarrow X(v = 1)$ are determined experimentally. The other transition wavelengths are derived using measured vibrational energies given in Ref. [108]. The calculated FCFs are obtained from Ref. [109] for the $A \rightarrow X$ decay and from Ref. [110] for the $B \rightarrow X$ decay. Error bars for the measured FCFs and VBRs represent 1-σ uncertainties. This table is reproduced from Ref. [66]. 18

2.3 Diagonal ($v' = v$) transition frequencies of relevance to laser cooling. The frequencies are measured with a HighFinesse WS7-60 wavemeter, which has a systematic uncertainty of ~60 MHz. Statistical uncertainties from the measurements are at the ~10 MHz level. 19

2.4 Off-diagonal ($v' \neq v$) transition frequencies of relevance to laser cooling. The frequencies are measured with a HighFinesse WS7-60 wavemeter, which has a systematic uncertainty of ~60 MHz. Statistical uncertainties from the measurements are at the ~10 MHz level. 20

5.1 The calculated FCFs for CaH, compared to experimental FCFs [66]. The experimental FCFs are derived from measured VBRs. Note that the active space was optimized for the B state. 59

5.2 Experimental stages for $B(v' = 0)$ state predissociation measurement. In the second column, $M^R_{v'-v''}$ denotes the laser information. M is A or B, representing the electronic excited state. R is the region S, I, or C (see text). The third column contains the normalized ground-state populations using unknown variables and calculated VBRs. The five variables n_1, κ, F_{B0a}, d_A and d_B represent $X(v'' = 1)$ state natural population, cleanup efficiency of laser B^C_{1-0}, $B(v' = 0)$ state predissociation probability, depletion efficiency of laser A^I_{0-0} and depletion efficiency of laser B^I_{0-0}. We denote the VBR normalization factors as $\mathcal{F}_{A_0} \equiv \sum_{i\neq 0} F_{A0i}$, $\mathcal{F}_{B_0} \equiv F_{B0a} + \sum_{i\neq 1} F_{B0i}$, and $\mathcal{F}_{B_1} \equiv F_{B0a} + \sum_{i\neq 0} F_{B0i}$. Additional information is in Sec. 5.2.4. 71

5.3 Method I of $B^2\Sigma^+$ $(v' = 1)$ predissociation measurement. Notation is similar to Table 5.2. In the third column, the variables include a, n_1, κ, F_{B1a} and d_B, representing state preparation (from $X(v'' = 0)$ to $X(v'' = 1)$) efficiency, $X(v'' = 1)$ natural population, cleanup efficiency of laser A^C_{0-1}, $B(v' = 1)$ predissociation probability and depletion efficiency of laser B^I_{1-1}. The VBR normalization factors are $\mathcal{F}_{A_1} \equiv \sum_{i\neq 1} F_{A0i}$, $\mathcal{F}_{A_2} \equiv \sum_{i\neq 0} F_{A1i}$, and $\mathcal{F}_{B_2} \equiv F_{B1a} + \sum_{i\neq 1} F_{B1i}$. 72

5.4 Method II of $B^2\Sigma^+$ $(v' = 1)$ predissociation measurement. In the third column, the 7 variables include a, n_1, κ_1, κ_2, F_{B1a}, d_A and d_B, representing state preparation [from $X(v'' = 0)$ to $X(v'' = 1)$] efficiency, $X(v'' = 1)$ natural population, cleanup efficiency of laser A^C_{1-0}, cleanup efficiency of laser A^C_{1-2}, $B(v' = 1)$ predissociation probability, depletion efficiency of laser A^I_{1-1} and depletion efficiency of laser B^I_{1-1}. The VBR normalization factors are $\mathcal{F}_{A_2} \equiv \sum_{i\neq 0} F_{A1i}$, $\mathcal{F}_{A_3} \equiv \sum_{i\neq 1} F_{A1i}$, $\mathcal{F}_{A_4} \equiv \sum_{i\neq 2} F_{A1i}$, and $\mathcal{F}_{B_2} \equiv F_{B1a} + \sum_{i\neq 1} F_{B1i}$. 73

5.5 Spin-orbit matrices accounting for vibrational mixing of the A and B states. The Π_x and Π_y basis states split under SOC to produce $\Pi_{1/2}$ and $\Pi_{3/2}$ states. The top matrix is for $A^2\Pi$ $(v' = 0)$ and $B^2\Sigma^+$ $(v' = 0)$, while the bottom one is for $A^2\Pi$ $(v' = 1)$, $B^2\Sigma^+$ $(v' = 1)$ and $B^2\Sigma^+$ $(v' = 0)$. The Franck-Condon factor f is introduced to account for the off-diagonal vibrational wavefunction overlap. The diagonal terms represent the energies of unperturbed states. All values are in cm^{-1}. 74

6.1 Center frequencies of the slowing lasers, measured on a HighFinesse WS7-60 wavemeter. 86

8.1 Measured CaH VBRs and calculated CaH and CaD VBRs [188]. The calculated VBRs for CaH are in good agreement with our own calculations in Chapter 5 and Ref. [97]. 112

8.2 CaD transition frequencies. The uncertainties are ~10 MHz statistical and ~60 MHz systematic from the wavemeter. 113

Acknowledgments

People always say one's PhD advisor determines the happiness of their life, as well as what they can accomplish during their PhD. I feel extremely lucky to have Prof. Tanya Zelevinsky as my advisor with her endless support and guidance. Tanya's support literally began from day one. When I first came in 2021 during COVID time and felt lost about what I wanted to do during my PhD, she offered to help reach out to other professors if I did not hear back from them. Now we know I stayed in Tanya's group, but her willingness to help always reminds me of her kindness and support. Along the way, there have been ups and downs in the experiments, but I was lucky to be always inspired and motivated by Tanya with her encouragement and belief in me. She also always gives her students the freedom to try whatever they want, magically, funding has never been a problem in her group. Without these, the work shown in this thesis would really not have been possible. Tanya's vision as a physicist greatly influences how I approach physics, and I am really grateful for her guidance and mentorship.

I would also like to thank our postdoc Debayan Mitra, who is now a professor at Indiana University, Bloomington. He was one of the closest role model I could learn from, and literally taught me every technical detail about molecular laser cooling and trapping. Most importantly, he taught us by example about how to be a good group leader and how to make the whole team move productively. He and I joined the experiment just a few months apart, when the team had just switched from BaH to CaH, and when the experiment was working suboptimally for this new molecule. His knowledge and leadership turned the experiment into a fast-moving pace. While not producing as many papers as the most successful projects, it was already impressive for a hard

experiment in its building phase. It is nice that we have been able to keep the momentum, producing at least a paper a year. Now the experiment is built and the MOT is working, there is no doubt anymore, only hope for a bright future.

When I first joined the group, I was lucky to be surrounded by a group of great scientists, whose inspiration was one of the reasons I am still trying to pursue a career in academia. Qi Sun was the one to introduce me to the group. He was one year above me, and we both graduated from the University of Science and Technology of China, and were even from the same group during undergrad. He and I worked together for the longest time, and I feel I can always learn from him, from technical details to life choices. His calmness and willingness to fix and improve things even in doubtful moments have been something I can always rely on. I am grateful that I was able to learn all these by example and pass them on to the team (hopefully I have!). Sebastián Francisco Vázquez-Carson was the more senior graduate student when I first joined. His passion for physics and his desire to always get hands-on have been really inspiring. Under Debayan's guidance, the time I spent learning machining from Sebastián and the manager of our machine shop Clara AR. Wilson has been very rewarding. I turned out to be the only resident machinist in the group in my later years. I always joked that if the experiment does not work out well, I could still survive by making screws in factories. I would not have that confidence without Sebastián's niche and Clara's training in machining. Special thanks to Clara for running the machine shop so well in the past few years. I also had the privilege to share the same lab space with Kon H. Leung, Emily Tiberi, and Brandon M. Iritani. Kon's insights in physics made him a really great resource for us as younger students. Emily was always there for us whenever we had any problems. Brandon and I are the same year, so we really shared a lot of ups and downs and have been the closest companion of each other during the journey of a PhD.

Time went on and more new faces joined the group. We were lucky to have Benjamin Riley for the next generation of the CaH experiment. Ben was one of the most motivated graduate students in their first few years and was able to help figure out a lot of problems. For the past year or two, it was basically me and him fighting for the MOT in the lab, and now that we have it, I

have no doubt that he will be successful and able to move the experiment forward to a great future. Around the same time, Mateusz Borkowski and Wenwei Xu joined the Sr experiment, really adding new energies to the group. I have no doubt Sr Gen II will turn out great in Wenwei's hands. Later we had Jingjing Huang and Hanwen Gao join us as postdocs on the Sr and the CaH experiments. Jingjing's joining gave us another resource of knowledge, which has been really valuable for the whole group. Although Hanwen was from a different background, he was able to fit in very fast and is already able to start leading the project. And I feel Hanwen and Ben will make a great team in the coming years.

There is also the CeNTREX team we always forgot to mention in the acknowledgment section in our DAMOP talks (they were sadly not in our group pictures because they are physically in Chicago). I would like to thank Jianhui Li and Perry Zhou for their passion and their eagerness to discuss and help. They somehow always have the magic to entertain people, even when they are talking about serious science. I really enjoyed the time we spent together during conferences, though very limited, and hoped we could have more interactions every day in the lab. I am also grateful to the newer group members Gisung Sim, Longxiang Jiang, and Koby Harding. Their joining made me start wondering what the group will be like in a few years, and I believe it will be great and full of energy.

During my PhD, I was also lucky to work with a lot of talented undergraduate and master's students. Instead of "mentoring", I also learned a lot and grew together with them. Isaac M. Pope, Carson Convery, Christine Zhang, Aleksandr Glamazdin, Andrii Shypachov, Shuqi Liu, Jintai Wu, Antoine Nadal, Xuanyi Meng, and the list is still growing. I also want to thank my undergraduate advisors, Prof. Zhengtian Lu, Prof. Tian Xia, Prof. Dong Sheng, Prof. Wei Yi, and Prof. Ronald Walsworth. Without their support, I would not be able to come to Columbia to do anything I am going to talk about in this thesis. Special thanks to Prof. Holger Müller, Prof. Zoe Z. Yan, and Prof. Vladan Vuletić, who gave me the chance to present my PhD work and provided the possibility to work in their group as a postdoc, and also to Prof. Sebastian Will who wrote me a letter for my fellowship application. My postdoc search has been really enjoyable because of

their support and also, perhaps needless to say, the support from Tanya and Debayan.

I would also like to thank the Will lab for their friendship, including Aaron Holman, Ximo Sun, Weijun Yuan, Siwei Zhang, and everyone else in the group. There have been really stimulating conversations during lunchtime. Outside the lab, I was also surrounded by warmth provided by all of my friends. Siwei was the first one that I had the most conversations with in my cohort. Smart as he is, he always provided a role model I wanted to compare myself to. He was also the driving force behind our trip to Singapore to obtain visas during COVID time, so a lot of the time I felt myself being carried by my friends. Later Siwei and Yiliu Li got together, and we became friends as a group. For the past several years, they have been my therapists outside of the lab whenever things did not go well. We also went to brunches and dinners all the time, and I found myself learning a lot of interesting physics when discussing ideas with them. Yiliu also introduced me to a healthier lifestyle, I started training for half marathons and completed two successfully (Brooklyn Half and New Jersey Half). Along the way, we met many new friends in the "Butler Run Club", Jackie Xu, Yunfei Huang, Ruoyu Zhang, Wenxin Zhang, and Xiaoyu Song. Shenyang Shi and Yinjie Guo from our cohort also joined the running group. I feel very lucky to have all my friends with me through the journey of the PhD.

Lastly, I would like to thank my family for all their support throughout my PhD. Although they came from a working class background, they never hesitated to invest in my education, without which I really could not have gone this far. I would also like to thank my partner, Jiazhi Xu, for the support throughout. We have known each other for almost 12 years and have been together for almost 10 years now, we literally grew up together. Now we cannot wait to move on to the next chapter of life together. I would like to dedicate this thesis to my partner, my parents, as well as my late grandparents.

Luminous and wired, we'll be glowing in the dark.

— Coldplay, "Charlie Brown"

Chapter 1: Introduction

Laser cooling of atoms [1] has been a cornerstone of modern atomic, molecular, and optical (AMO) physics. The ability to laser cool, trap, and manipulate atoms at ultracold temperatures has greatly advanced precision measurements and metrology, enabling searches for physics beyond the Standard Model with tabletop experiments [2] and improving optical atomic clocks [3]. It has also enabled new platforms for quantum computation [4] and simulation [5]. With years of development, the field of ultracold atoms has progressed remarkably and remains one of the most promising candidates for quantum science applications. By contrast, efforts to control more complex quantum systems, such as molecules in the ultracold regime, have only emerged in the past few decades. While their richer internal structures make them more challenging to manipulate, they offer new opportunities.

1.1 Why Cold Molecules

Molecules make up most of the things we see everyday. There have been growing efforts devoted to understanding and controlling their properties. Thanks to the new techniques in modern AMO physics, it has become possible to cool, trap, and manipulate molecules at the quantum level. These advances have enabled a wide range of new research directions that were previously inaccessible, including new opportunities for precision measurements, cold and ultracold chemistry, and quantum simulation and computation.

1.1.1 Precision Measurements

The first natural improvement once molecules are at cold or even ultracold temperatures would be the precision to measure anything with them. Measurements of the permanent electric dipole

moments (EDMs) of electrons and nucleons are a notable example [6, 7, 8, 9]. In the current Standard Model of physics, the EDM is predicted to be extremely small, yet some new physics predicts larger values (depending on specific models). It has always been an interest of AMO physicists to measure the EDM to higher precision, which could in the end correspond to larger energy scale that may not be reachable at the Large Hadron Collider at CERN [10, 11]. The EDM was initially measured with atoms [12, 13, 14] where the targeted signal is proportional to the externally applied electric field achievable in the laboratory. Using molecules can greatly improve the sensitivity because of the strong internal electric field in molecules. Such measurements have been performed with cold molecular beams [6, 7] and trapped molecular ions [8, 9], and future experiments are expected to achieve order-of-magnitude higher precision.

The additional internal structures of molecules also give rise to enhanced sensitivities for precision measurements of fundamental constants. For example, vibrational and rotational transitions in molecular spectra scale with the electron-to-proton mass ratio μ, while electronic transitions do not. Nearly degenerate vibrational levels in certain diatomic and polyatomic molecules could be significantly shifted if there exists a temporal variation of μ [15, 16]. Such temporal variation has been proposed to originate from ultralight dark matter particles like axions and axionlike particles [17]. Measurements of the relevant energy levels in molecules could put constraints on these dark matter models.

Similar to atomic systems, molecular transitions can also be engineered for precise quantum clocks. In fact, the very first quantum clock was based on ammonia molecules [18]. Atomic clocks have advanced significantly because of the new techniques to cool and trap them in optical lattices [3]. Recently, a molecular lattice clock was demonstrated in the neighboring laboratory in our group [19], achieving the highest precision reported for molecule-based quantum clocks. Though not comparable to atomic clocks yet, the additional internal structures already promise interesting physics to explore, such as the temporal variation of μ and isotope shift measurements for searches of the fifth force [20]. Further exploration of these systems will be valuable and will benefit from the continued development of new techniques in the field.

1.1.2 Cold and Ultracold Chemistry

With molecules cooled to cold and ultracold temperatures, chemical processes in this new regime can be studied [21]. Unlike traditional chemical systems, where reactions occur over a broad distribution of collision energies and internal states, ultracold chemical systems allow one to prepare them in well-defined quantum states and study interactions governed by quantum statistics. One notable observation in this regime is the existence of long-lived complexes, formed by the so-called "sticky collisions" [22]. A thorough investigation of such processes is valuable as it not only gives us better understanding of how these processes occur, but also provides insights toward achieving quantum control of chemical reactions, and it has been an active research area for the past decades. Recent progress shows that coherence can be preserved during chemical reaction in the ultracold regime [23, 24]. Precise tuning of chemical reactions with external fields would also be valuable in order to perform sympathetic cooling with atoms to further cool the molecules [25, 26]. On the other hand, further investigations could shed light to fundamental chemical processes occurring in stellar and interstellar media, given their similar conditions.

1.1.3 Quantum Simulation and Computation

The tunable dipolar interactions in molecules offer a unique opportunity to simulate complex quantum system such as those in many-body physics [27]. These long-range interactions could be harnessed to realize a variety of Hamiltonians including those for lattice spin models [28], topological ordered states [29], and extended Hubbard models [30]. This list continues to grow. The additional internal structures in molecules could also be used to encode quantum information. At present, quantum computation with neutral atom arrays is limited by gate fidelities that remain below the threshold required for quantum error correction to achieve fault tolerance. The long lifetimes of molecules promise a robust qubit compared to atoms [31, 32]. Two-qubit gates have been demonstrated in various molecular systems recently [33, 34, 35, 36]. Future improvements, in part, require advances in cooling techniques [37, 38]. Once these challenges are addressed, molecules offer a promising platform for the future of quantum computation.

1.2 Production of Cold and Ultracold Molecules

The rich internal structures of molecules make their production tricky. Take diatomic molecules as an example, the characteristic energy scales of the rotational and vibrational excitations are on the order of a few kelvin and a few tens of kelvin, respectively. If one starts with a room temperature sample, the molecules could populate all possible states that are energetically accessible. However, all applications discussed in the previous section require addressability at the level of individual quantum states. To solve this problem, there are currently two main methods for producing cold and ultracold molecules: indirect and direct methods.

1.2.1 Indirect Methods

The indirect method involves first cooling the constituent atoms and then assembling them into ultracold molecules. This method does not require direct cooling of molecules, however, the molecular species are limited since the constituent atoms need to be laser-coolable in the first place. Despite this limitation, this method has been highly successful. There are generally two methods of assembling molecules: magnetoassociation and photoassociation. Magnetoassociation refers to assembling molecules through tuning a magnetic field to a Feshbach resonance. Weakly bond (at high vibrational levels) molecules could be created this way. These molecules can be transferred to the absolute ground (electronic, vibrational, and rotational) state through stimulated Raman adiabatic passage (STIRAP). A number of ultracold ground-state molecules are created this way, including KRb [39], RbCs [40], NaK [41], NaRb [42], NaLi [43], NaCs [44], and LiK [45]. Recent advances have enabled the realization of quantum degenerate gases some of some of these molecules [46, 47, 48]. Quantum simulation with these ultracold molecules may be possible in the near future [49]. Photoassociation, on the other hand, does not rely on the existence of Feshbach resonances. Instead, this method excites two atoms to a molecular bond state then part of them can decay back to a ground molecular bond state. The molecules can in principle decay to all dipole allowed rovibrational states, thus the efficiency would greatly rely on the branching ratios. The first

molecular lattice clock discussed in the previous section is based on this method, with ground-state Sr_2 molecules created [50]. Other indirect methods exist but are very limited to specific molecular species with their unique properties, such as the mergoassociation of RbCs molecules [51].

1.2.2 Direct Methods

If starting from a hot sample of molecules, one would need direct cooling methods to bring them to the ultracold regime. Most of the chemists' molecules, bigger molecules, or organic molecules need to be treated this way (we call most of molecules created with the indirect methods physicists' molecules since they only exist in physics laboratories). One of the most general cooling methods is buffer gas cooling [52]. This method relies on elastic collisions with buffer gases such as He or Ne at cryogenic temperatures. The external and internal temperatures of molecules can be cooled to the buffer gas temperatures efficiently. Cryogenic buffer gas beams of molecules ranging from big organic molecules to laser ablated radicals can be created this way. Although the lowest temperature achievable with this method is limited by the buffer gas properties, it provides a great starting point for further cooling with temperatures down to a few kelvin, where most molecules would only occupy a few quantum states.

To achieve ultracold temperatures, further cooling is required. One could take advantage of the dipolar nature of molecules and use electric field to slow and cool the molecules. With proper electric field configuration, molecules can made to be always experiencing potential hills, the translational energies can thus be removed by the electric field potentials [53, 54]. One can also make use of the Zeeman shifts under magnetic fields, slowing forces can also be engineered [55]. Zeeman-Sisyphus deceleration has also been demonstrated with molecules [56, 57]. Other methods include mechanical deceleration using centrifuges [58, 59] and optoelectrical cooling [60]. However, all these methods remain proof-of-principle demonstrations, and further experiments are limited because of the large field required. Laser cooling, though less general as these methods and requiring favorable Franck-Condon factors to establish a quasi-closed photon-cycling scheme, has led to many advances in the field and will be the main focus of this thesis.

Since the first demonstration of molecular laser cooling with SrF molecules [61], the field has expanded greatly. 2D magneto-optical compression of YO [62], 1D magneto-optical compression of CaF [63], 1D sub-Doppler cooling of YbF [64], 1D sub-Doppler cooling of BaH, CaH, and CaD [65, 66, 67], 1D Doppler and sub-Doppler cooling of BaF [68, 69], and the same technique has been demonstrated for polyatomic molecules [70, 71, 72, 73]. 3D magneto-optical trapping of molecules have also been demonstrated with SrF [74], CaF [75], YO [76], CaOH [77], BaF [78], SrOH [79], and AlF [80], opening the door for optical trapping and quantum control of molecules in the ultracold regime. In this thesis, I describe the extension of these techniques to a new class of molecules, diatomic metal hydrides. We demonstrate the first 3D magneto-optical trap (MOT) of CaH molecules [81].

1.3 Ultracold Molecules for Exotic Ultracold Atoms

Despite the tremendous success of atomic laser cooling, only a small fraction of the periodic table is amenable to this technique [82]. Many atomic species are excluded because of their deep ultraviolet (UV) transition wavelengths. One notable example is hydrogen atoms. It is technically challenging to obtain high power for laser cooling at ∼122 nm for hydrogen, and thus this technique has remained elusive. Recent experiments have focused on proof-of-principle demonstrations of the technique [83, 84], but cooling to the ultracold regime is still a distant goal. Laser-cooled molecules offer a possible pathway toward producing ultracold samples of otherwise inaccessible atomic species like hydrogen.

1.3.1 Hydrogen Spectroscopy

Hydrogen, as the simplest two-body system, has always been at the forefront of quantum related research. From Bohr's first quantum theory of atomic physics [85], Lamb shift and the birth of quantum electrodynamics [86], to nowadays' precision tests of the Standard Model [87], all rely on measuring the hydrogen spectroscopy to higher and higher precision. Over the past few decades, hydrogen spectroscopy has advanced remarkably. The narrow $1S$–$2S$ transition was

measured down to Hz-level precision [88, 89]. Other broader transitions were also measured to unprecedented precision [90, 91, 92, 93]. However, these measurements are still limited by velocity-dependent broadening arising from the finite temperature of the atomic beam. Further improvements would require the production of a trapped, dilute, and ultracold sample of hydrogen atoms. Additionally, there has been a decade-long "proton radius puzzle", where the proton charge radius extracted from electronic and muonic hydrogen spectroscopy are discrepant [87]. Recent measurements may suggest that the puzzle may originate from underestimated systematic uncertainties in earlier hydrogen atomic beam measurements [94, 95], further motivating the need for trapped hydrogen measurements. It is worth noting that a Bose-Einstein condensate of atomic hydrogen has been produced with magnetic traps [96], but the high-field environment makes it imperfect for high-precision spectroscopy. To circumvent these challenges, we propose an approach based on the dissociation of laser-cooled metal hydride molecules, such as CaH. The resulting hydrogen atoms can then be loaded into optical dipole traps, which provide an ideal platform for precision spectroscopy.

1.3.2 Ultracold CaH for Ultracold Hydrogen

Figure 1.1 shows a schematic of the proposed approach. We utilize the established molecular laser cooling technique to first cool and trap CaH molecules at submillikelvin to microkelvin temperatures, then apply a near-threshold dissociation to get the hydrogen atoms. At first glance, two key questions arise for this approach: first, whether CaH molecules can be laser cooled and trapped; and second, whether a suitable dissociation pathway can be identified, and if so, whether the resulting hydrogen atoms can remain cold.

In this thesis, we answer both questions. First, yes, CaH can be laser cooled and trapped at ultracold temperatures. CaH is not the most ideal laser-cooling candidate due to its weaker molecular bond. As a result, every time we scatter a photon, there is a finite chance that the molecule gest dissociated, called predissociation [97]. Additionally, CaH molecular beams are an order-of-magnitude weaker than other laser-cooled molecules for various reasons [98]. We show how

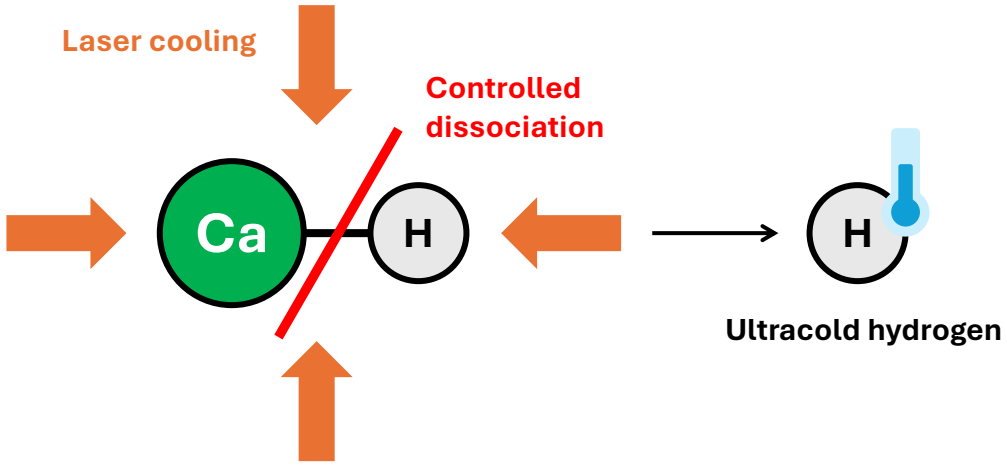

Figure 1.1: Proposed approach for producing ultracold hydrogen. CaH molecules are first laser cooled and trapped, followed by near-threshold dissociation to produce hydrogen atoms at ultracold temperatures.

we solve these problems and create a 3D MOT of CaH. Second, we show that predissociation, in turn, can facilitate controlled dissociation and identify a potential dissociation pathway that are readily accessible with existing laser technologies. Now the last question is, whether the resulting hydrogen atoms can remain cold, and the answer is also yes. Ultracold molecules created with the indirect methods have already paved the way for us. For either magnetoassociation and photoassociation, because of the lack of cycling transitions in those molecules, one has to dissociate the molecules and image the constituent atoms to gain information about the molecules. These processes typically only introduce negligible amount of energy from the noise of magnetic fields or lasers, or photon recoils. We do not expect dissociation of CaH being fundamentally different from other molecules, but if anything, the large mass imbalance could help on achieving colder temperatures. Assuming that the dissociated hydrogen atoms have comparable velocity distribution as the parent CaH molecules, the temperature of hydrogen could be even colder [99]. These demonstrations and considerations make this approach promising for producing hydrogen atoms at ultracold temperatures for high-precision spectroscopy in the near term.

1.4 This Thesis

This thesis is organized as follows. Chapter 2 introduces the basics for molecular laser cooling, relevant CaH properties are also provided. Chapter 3 discusses our molecular beam source and how we manage to improve it. Chapter 4 and Chapter 5 present our early demonstration of 1D laser cooling of CaH and studies of predissociation. Chapter 6 and 7 present our demonstration of white-light laser slowing and a 3D radio-frequency (rf) MOT of CaH. Chapter 8 presents the extension of the technique to the fermionic CaD. Finally, Chapter 9 provides a summary and outlook.

Chapter 2: The Molecular Laser Cooling Technique

Compared to atoms, molecules posses additional energy levels originating from vibration and rotation. In order to perform laser cooling, these additional energy levels need to be carefully addressed. This chapter provides the basics of the structure of diatomic molecules, and how we can engineer a quasi-closed transition to continuously scatter photon for laser cooling. I also list the relevant spectroscopy data for laser cooling of CaH.

2.1 Diatomic Molecular Structure

Fortunately, vibrational and rotational degrees of freedom in diatomic molecules are typically well separated in energy. Vibrational energies are on the order of tens of THz, while rotational energies are in the GHz range. As a result, they can be treated independently, or in other words, can be treated with Born-Oppenheimer approximation. The Hamiltonian for a diatomic molecule can thus be written as

$$H = H_{\mathrm{e}} + H_{\mathrm{vib}} + H_{\mathrm{SO}} + H_{\mathrm{rot}} + H_{\mathrm{SR}} + H_{\mathrm{HFS}} + H_{\Lambda\mathrm{d}}. \tag{2.1}$$

Here, H_{e}, H_{vib}, H_{SO}, H_{rot}, H_{SR}, H_{HFS}, and $H_{\Lambda\mathrm{d}}$ denote the electronic, vibrational, spin-orbit, rotational, spin-rotation, hyperfine, and Λ-doubling components of the Hamiltonian, respectively. The components are listed in a descending order of energy scale for clarity, with Λ doubling as an exception, as its magnitude can vary significantly in different electronic states.

2.1.1 Electronic Energy Levels

The largest energy scale in the Hamiltonian [Eq. (2.1)] is the electronic level H_{e}. The splittings in different electronic levels are on the order of several hundred THz. Electronic transitions

Table 2.1: State notations for atoms and molecules, reproduced from Ref. [104].

	Atoms		Molecules	
	Symbol	Values	Symbol	Values
Electronic spin	$\mathbf{S}$	$0, 1/2, 1, \ldots$	$\mathbf{\Sigma}$	$0, 1/2, 1, \ldots$
Orbital angular momentum	$\mathbf{L}$	$s, p, d, \ldots$	$\mathbf{\Lambda}$	$\Sigma, \Lambda, \Delta, \ldots$
Total angular momentum	$\mathbf{J}$	$0, 1/2, 1, \ldots$	$\mathbf{\Omega}$	$0, \pm 1/2, \pm 1, \ldots$

can thus be addressed with laser sources in the visible and near-infrared range. Some molecules like AlF [100], AlCl [101], and MgF [102, 103] even require lasers in the UV range. The "principal quantum number" of electronic levels in molecules are labeled by capital letters X, A, B, C, ... Here, X is used for ground states, while letters starting from A are used for electronically excited states. For historical reasons, the ordering does not strictly follow the energy levels, but instead reflects the order of discovery. Similar to atoms, molecules also have electronic spin $\mathbf{S}$, orbital angular momentum $\mathbf{L}$, and their resulting total angular momentum $\mathbf{J}$. The difference is that, atoms posses spherical symmetry, while diatomic molecules posses axial symmetry upon their internuclear axis. For $\mathbf{S}$, $\mathbf{L}$, and $\mathbf{J}$ in atoms, their molecular counterparts are $\mathbf{\Sigma}$, $\mathbf{\Lambda}$, and $\mathbf{\Omega}$, respectively. Table 2.1 summarizes the differences and connection between these notations in atoms and molecules.

With these notations, electronic energy levels in molecules can be labeled with the molecular term symbol:

$$^{2S+1}\Lambda_{\Omega}^{+/-}. \tag{2.2}$$

The additional $+/-$ denotes the reflection symmetry of the corresponding electronic state. To show an example of how this term symbol works, the ground electronic state of CaH is a spin doublet since it contains an uncoupled electron, the orbital angular momentum is zero for the ground state, thus $\Lambda = \Sigma$ (or 0), as a result, the ground electronic state of CaH is denoted as $X^2\Sigma^+$. Other relevant electronic states will be discussed in more details later.

2.1.2 Vibrational Energy Levels

The next energy scale after electronic levels comes from vibrational energy levels. At a given electronic energy level, the vibrational energy levels can be described using a power series as in Refs. [104, 105]:

$$G(v) = \omega_e(v + 1/2) - \omega_e x_e(v + 1/2)^2 + \omega_e y_e(v + 1/2)^3 + \cdots , \tag{2.3}$$

where v is the vibrational quantum number, ω_e is the vibrational constant, and $\omega_e x_e$ and $\omega_e y_e$ are constants for higher-order corrections. As one can tell from the notations, these constants are different for different electronic energy levels.

2.1.3 Rotational Energy Levels

The smallest energy scale in a diatomic molecule comes from rotational energy levels. For a given vibrational energy level v, the rotational energy levels can be expressed as in Refs. [104, 105]:

$$F_v(J) = B_v J(J + 1) - D_v J^2(J + 1)^2 + H_v J^3(J + 1)^3 + \cdots , \tag{2.4}$$

where J is the rotational quantum number, B_v is the rotational constant, and similar to vibrational energy levels, D_v and H_v are the higher-order correction terms. Detailed expressions of these constants can be found in Refs. [104, 105]. For the purpose of this thesis, we do not need to go into details on how these constants are derived or obtained with spectroscopic data. Again, interested readers are referred to Refs. [104, 105].

Most of the molecules of interest have been studied for decades and there have been extensive measured lines, although not measured to the precision that we need. In practice, we take the lines of interest and measure them ourselves, and they are typically within several hundred MHz. However, we do need to understand how the states are labeled after those with comparable energy scales couple to each other so we can read these spectroscopic data; this is discussed next.

2.1.4 Fine Structure, Spin-Rotation Coupling, and Hyperfine Structure

Similar to atoms, molecules with unpaired electronic spins also have additional splittings due to for example spin-orbit coupling. Since molecular rotation is also at a comparable energy scale, there is also spin-rotation coupling. And if there exist a nuclear spin, there would also be hyperfine splitting. For our molecule CaH, Ca has a unpaired electron, $S = 1/2$, though it does not have a nuclear spin, H has a nuclear spin of $I = 1/2$.

For the electronic ground state of CaH, $X^2\Sigma^+$, orbital angular momentum $L = 0$ and $\Lambda = 0$, the spin-orbit coupling is thus zero. The next term in the Hamiltonian is the spin-rotation coupling

$$H_{\mathrm{SR}} = \gamma_{vN}\mathbf{S}\cdot\mathbf{N}. \tag{2.5}$$

Here, rotation is denoted with **N**, because with an electronic spin, bare rotation **R** no longer represents a good quantum number, and **N** is the total angular momentum excluding spin. γ_{vN} is the spin-rotation constant. The result from this coupling is **J**, or the total angular momentum. Lastly, with nuclear spin **I**, we obtain the grand total angular momentum $\mathbf{F} = \mathbf{J} + \mathbf{I}$ through the hyperfine interaction. In this case, N, J, and F are the good quantum numbers, meaning these quantities are conserved under the discussed interactions, and this is described by the so-called Hund's case (b), as shown on the right of Fig. 2.1. In Hund's case (b), **L** is strongly coupled to the internuclear axis, then the resulting **Λ** couples with **R** to form **N**, and **N** couples with **S** and forms **J**. Note that since **L** does not couple with **S** first, **Ω** is poorly defined, which is the reason why we do not show the Ω number in the ground electronic state of CaH, $X^2\Sigma^+$. Another electronic state that is also described by Hund's case (b) and is discussed extensively in this thesis is the $B^2\Sigma^+$ state.

The lowest excited state of CaH is $A^2\Pi_{1/2}$, and is described by Hund's case (a). In Hund's case (a), as shown on the left of Fig. 2.1, **L** couples to **S** first, then they couple to rotation **R** to form **J**. For this electronic state, $\Omega = \Lambda - \Sigma = 1 - 1/2 = 1/2$, so it is written as $A^2\Pi_{1/2}$. The nonzero Λ

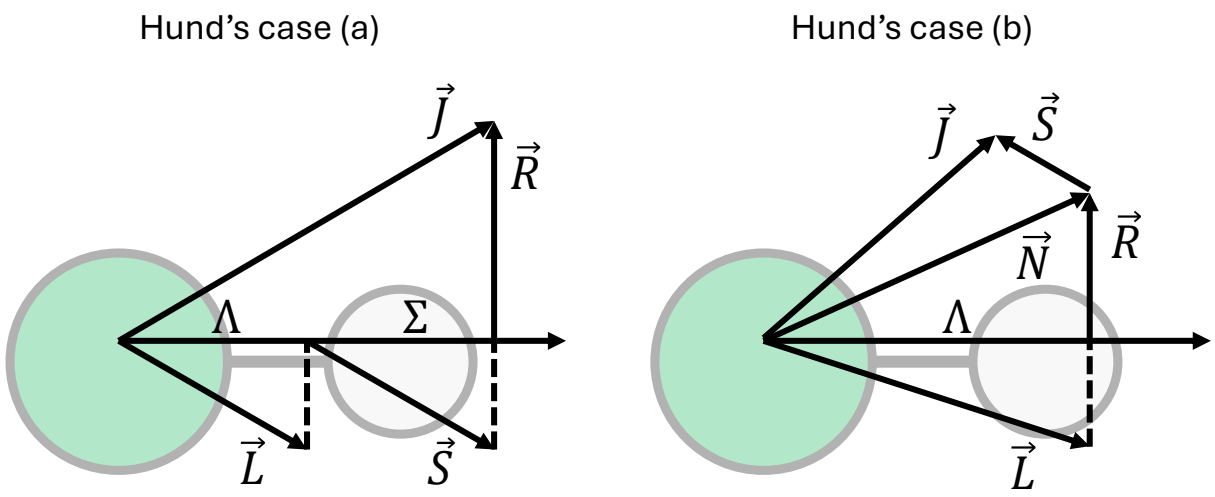

Figure 2.1: Relevant Hund's cases in this thesis. The lowest excited $A^2\Pi_{1/2}$ state of CaH is described by Hund's case (a) as shown on the left, and the ground electronic state is described by Hund's case (b) on the right. The second excited $B^2\Sigma^+$ state is also described by Hund's case (b).

here gives rise to the spin-coupling term

$$H_{\mathrm{SO}} = A\mathbf{L}\cdot\mathbf{S}, \tag{2.6}$$

and A here is the spin-orbit coupling constant. This term, if present, is typically much larger than the rotational and hyperfine levels. For $A^2\Pi$ states, spin-orbit coupling results in two multiplets of $A^2\Pi_{1/2}$ and $A^2\Pi_{3/2}$. We address transitions more on the $A^2\Pi_{1/2}$ states in the context of laser cooling.

For a nonzero Λ, there is another effect originating from the different directions of the electron's circulation around the internuclear axis, and is called Λ doubling. This will cause degeneracy if the resulting Ω is also nonzero and can be a positive or a negative value. The rotational degree of freedom lifts this degeneracy by adding the additional $H_{\Lambda\mathrm{d}}$ term in the Hamiltonian. The resulting states are noted with parity $+/-$. For $^2\Sigma^+$ states, parities are paired with N since they are split through the interaction with rotation, while for $^2\Pi_{1/2}$ states where N is not a good quantum number, parities are important to be presented in order to distinguish these doublet states.

2.2 Laser Cooling Scheme

Laser cooling relies on the ability to continuously scatter photons. For atoms, it is easy to find a "closed" or a "cycling" transition where the atoms always fall back to the same ground state after being excited by a laser. For molecules, as one can tell from the more complex level structure discussed in the previous subsection, it becomes a little tricky.

2.2.1 Vibrational Branching

Following the same order as when we introduce the energy levels, we first consider the vibrational levels. When excited, molecules can decay back to all the vibrational states that are electric-dipole allowed. The branching ratios to different vibrational states are proportional to the Franck-Condon factors (FCFs) defined as the wavefunction overlap:

$$q_{v'v''} = |\langle \psi_{v'} | \psi_{v''} \rangle|^2, \tag{2.7}$$

where $|\psi_{v''}\rangle$ and $|\psi_{v'}\rangle$ denote the vibrational eigenstates of the ground and excited states (in this thesis, we use $''$ to denote the ground states and $'$ to denote the excited states). In order to achieve a quasi-closed transition with a practical number of lasers, one would require the FCFs to be highly diagonal, meaning strong coupling only happens when $v' = v''$, and decays to other vibrational states are highly suppressed. CaH, including all other laser-cooled molecules, is of this type. The naive picture is that, if the wavefunction of the unpaired electron is sufficiently far away from the molecular bond, exciting that unpaired electron would not affect the bond significantly.

FCFs can be extracted from the potential energy curves [PECs, energy as a function of internuclear distance, or potential energy surfaces (PESs) if multidimensional] obtained with *ab initio* calculations [97]. Branching ratios to different vibrational states can be expressed as

$$\mathrm{VBR}_{v'v''} = \frac{q_{v'v''} \times \omega^3_{v'v''}}{\sum_{k=0}^{\infty} q_{v'k} \times \omega^3_{v'k}}, \tag{2.8}$$

where $\omega_{v'v''}$ is the energy difference between the corresponding ground and excited vibrational states. VBRs can be experimentally measured through the relative decay rate to different ground vibrational states. Table 2.2 summarizes the measured and calculated VBRs and FCFs of CaH with $v' = 0$ for both $A \rightarrow X$ and $B \rightarrow X$ transitions. To perform laser cooling, we excite CaH from the electronic and vibrational ground state $X(v = 0)$ to either $A(v' = 0)$ or $B(v' = 0)$. Because of the highly diagonal FCFs ($q_{00} > 95\%$), the molecules decay back to $X(v'' = 0)$ most of the time. However, to trap the molecules, one would need to scatter at least $\sim 10^4$ photons to slow a fast molecular beam at ~ 150 m/s down to near zero velocity. If only addressing a single transition, only $1/e$ of the total population could survive after scattering just $1/(1-\mathrm{VBR}_{00}) \sim 50$ photons. For molecules with diagonal FCFs, adding two to three repump lasers is typically enough to bridge this gap. Figure 2.2 shows the laser cooling scheme for CaH as an example, featuring a vibrationally quasi-closed scheme.

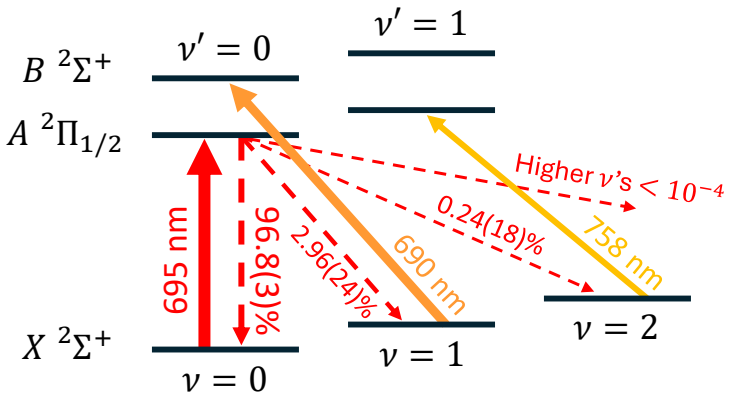

Figure 2.2: A vibrationally quasi-closed scheme in CaH. For molecules with diagonal FCFs like CaH, branching to higher vibrational states are suppressed exponentially. Two to three vibrational repump lasers are typically enough to achieve a photon budget of $\sim 10^4$–10^5.

2.2.2 Rotational Branching

The next aspect to consider is the rotational energy levels. Compared to vibrational branching, rotational branching follows parity and angular momentum selection rules strictly for electric-dipole transitions. The parities of the start and final states must be opposite, or if both in the $^2\Sigma^+$ manifold, $\Delta N = \pm 1$. Similar to atoms, molecules also have selection rules $\Delta J = 0, \pm 1$, $\Delta F =$

0, ±1, and $\Delta m_F = 0, \pm 1$. Rotational closure can be achieved if we start from $X^2\Sigma^+(N = 1, -)$ manifold. Figure 2.3 shows the two schemes for CaH that are used in this thesis. If exciting $X^2\Sigma^+(N = 1, -)$ to $A^2\Pi_{1/2}(J' = 1/2, +)$ as in (a), it can only find its way back to $X^2\Sigma^+(N = 1, -)$ because of the parity requirement [$(N = 0)$ and $(N = 2)$ states are + parity]. If exciting $X^2\Sigma^+(N = 1, -)$ to $B^2\Sigma^+(N = 0, +)$ as in (b), it can only go back to $X^2\Sigma^+(N = 1, -)$ as well since $\Delta N = \pm 1$.

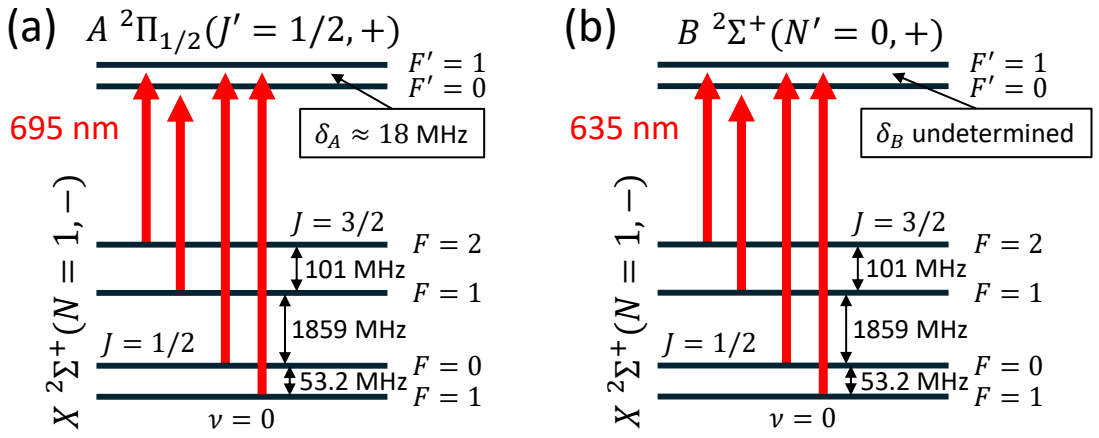

Figure 2.3: Rotational closure for the $A^2\Pi_{1/2}(v' = 0) \leftarrow X^2\Sigma^+(v = 0)$ and $B^2\Sigma^+(v' = 0) \leftarrow X^2\Sigma^+(v = 0)$ transitions, shown as examples. Note that the spin-rotation and hyperfine splittings are slightly different for different vibrational states and need to be treated carefully. Hyperfine splittings for the excited states are expected to be unresolved within the MHz level. However, we do measure an 18 MHz splitting in the $A^2\Pi_{1/2}(v' = 0, J' = 1/2, +)$ state. This is very important in the context of a MOT and is discussed in more detail in the corresponding chapter.

However, this scheme poses an additional challenge: dark states. For transitions with $F \geq F'$, a certain laser polarization can only address a subset of the magnetic sublevels in the ground state. To show an example, if $F = 1$ and $F' = 0$ and the laser is linearly polarized, states with $m_F = \pm 1$ become dark and cannot be addressed by the laser. Fortunately, this is a solvable problem and there have been various approaches to remix these dark states to make them appear bright again, including magnetic-field remixing and polarization switching.

2.3 Reference Tables for CaH Laser Cooling

Now that we have determined a photon-cycling scheme for laser cooling, here I summarize relevant information for CaH, including FCFs (Table 2.2) and transition frequencies (Table 2.3 and Table 2.4) used in this thesis. All data shown in these tables are experimentally measured in our laboratory, measurement schemes and key takeaways are provided when necessary.

Table 2.2: FCFs and VBRs with excited state vibrational quantum number $v' = 0$. The experimental radiative lifetime τ for the A state was obtained from Ref. [106] and for the B state from Ref. [107]. In this table, the transition wavelengths of $A(v' = 0) \leftarrow X(v = 0)$, $B(v' = 0) \leftarrow X(v = 0)$, and $B(v' = 0) \leftarrow X(v = 1)$ are determined experimentally. The other transition wavelengths are derived using measured vibrational energies given in Ref. [108]. The calculated FCFs are obtained from Ref. [109] for the $A \rightarrow X$ decay and from Ref. [110] for the $B \rightarrow X$ decay. Error bars for the measured FCFs and VBRs represent 1-σ uncertainties. This table is reproduced from Ref. [66].

Transition	τ (ns)	v''	Wavelength (nm)	$q_{0v''}$ theory	$q_{0v''}$ measured	$\mathrm{VBR}_{0v''}$ measured
$A \rightarrow X$	33(3)	0	695.13	0.953	0.9572(43)	0.9680(29)
		1	761.87	0.0439	0.0386(32)	0.0296(24)
		2	840.07	2.74×10^{-3}	$4.2(3.2) \times 10^{-3}$	$2.4(1.8) \times 10^{-3}$
		3	932.80	2.3×10^{-4}	–	–
$B \rightarrow X$	58(2)	0	635.12	0.9856	0.9807(13)	0.9853(11)
		1	690.37	0.0132	0.0173(13)	0.0135(11)
		2	753.97	1.1×10^{-3}	$2.0(3) \times 10^{-3}$	$1.2(2) \times 10^{-3}$
		3	827.84	1×10^{-4}	–	–

Table 2.3: Diagonal ($v' = v$) transition frequencies of relevance to laser cooling. The frequencies are measured with a HighFinesse WS7-60 wavemeter, which has a systematic uncertainty of ~60 MHz. Statistical uncertainties from the measurements are at the ~10 MHz level.

Ground	v	N	J	F	parity	Excited	v'	N'	J'	F'	parity	Frequency (THz)
$A^2\Pi_{1/2}(v'=0,\ J'=1/2,\ +) \leftarrow X^2\Sigma^+(v=0,\ N=1,\ -)$ cycling												
X	0	1	1/2	0	−	A	0	−	1/2	1	+	431.276550
X	0	1	1/2	1	−	A	0	−	1/2	1	+	431.276603
X	0	1	3/2	1	−	A	0	−	1/2	0	+	431.274672
X	0	1	3/2	2	−	A	0	−	1/2	1	+	431.274590
$B^2\Sigma^+(v'=0,\ N'=0,\ +) \leftarrow X^2\Sigma^+(v=0,\ N=1,\ -)$ cycling												
X	0	1	1/2	0	−	B	0	0	1/2	0, 1	+	472.028639
X	0	1	1/2	1	−	B	0	0	1/2	0, 1	+	472.028692
X	0	1	3/2	1	−	B	0	0	1/2	0, 1	+	472.026780
X	0	1	3/2	2	−	B	0	0	1/2	0, 1	+	472.026679
$A^2\Pi_{1/2}(v'=1,\ J'=1/2,\ +) \leftarrow X^2\Sigma^+(v=1,\ N=1,\ -)$ cycling												
X	1	1	1/2	0	−	A	1	−	1/2	0, 1	+	432.343902
X	1	1	1/2	1	−	A	1	−	1/2	0, 1	+	432.343958
X	1	1	3/2	1	−	A	1	−	1/2	0, 1	+	432.342120
X	1	1	3/2	2	−	A	1	−	1/2	0, 1	+	432.342011
$B^2\Sigma^+(v'=1,\ N'=0,\ +) \leftarrow X^2\Sigma^+(v=1,\ N=1,\ -)$ cycling												
X	1	1	1/2	0	−	B	1	0	1/2	0, 1	+	471.558969
X	1	1	1/2	1	−	B	1	0	1/2	0, 1	+	471.559025
X	1	1	3/2	1	−	B	1	0	1/2	0, 1	+	471.557178
X	1	1	3/2	2	−	B	1	0	1/2	0, 1	+	471.557078
$A^2\Pi_{1/2}(v'=0,\ J'=3/2,\ +) \leftarrow X^2\Sigma^+(v=0,\ N=1\&3,\ -)$ cycling												
X	0	1	1/2	0	−	A	0	−	3/2	1, 2	+	431.604611
X	0	1	1/2	1	−	A	0	−	3/2	1, 2	+	431.604664
X	0	1	3/2	1	−	A	0	−	3/2	1, 2	+	431.602751
X	0	1	3/2	2	−	A	0	−	3/2	1, 2	+	431.602651
X	0	3	5/2	2	−	A	0	−	3/2	1, 2	+	430.338953
X	0	3	5/2	3	−	A	0	−	3/2	1, 2	+	430.339023
$E^2\Pi_{1/2}(v'=0,\ J'=3/2,\ -) \leftarrow A^2\Pi_{1/2}(v=0,\ J=3/2,\ +)$ single-photon process												
A	0	−	3/2	1, 2	+	E	0	−	3/2	1, 2	−	179.685381

Table 2.4: Off-diagonal ($\nu' \neq \nu$) transition frequencies of relevance to laser cooling. The frequencies are measured with a HighFinesse WS7-60 wavemeter, which has a systematic uncertainty of ~60 MHz. Statistical uncertainties from the measurements are at the ~10 MHz level.

Ground	ν	N	J	F	parity	Excited	ν'	N'	J'	F'	parity	Frequency (THz)
$A^2\Pi_{1/2}(\nu'=0,\ J'=1/2,\ +) \leftarrow X^2\Sigma^+(\nu=1,\ N=1,\ -)$ repumping												
X	1	1	1/2	0	−	A	0	−	1/2	0, 1	+	393.504614
X	1	1	1/2	1	−	A	0	−	1/2	0, 1	+	393.504670
X	1	1	3/2	1	−	A	0	−	1/2	0, 1	+	393.502832
X	1	1	3/2	2	−	A	0	−	1/2	0, 1	+	393.502723
$B^2\Sigma^+(\nu'=0,\ N'=0,\ +) \leftarrow X^2\Sigma^+(\nu=1,\ N=1,\ -)$ repumping												
X	1	1	1/2	0	−	B	0	0	1/2	0, 1	+	434.256731
X	1	1	1/2	1	−	B	0	0	1/2	0, 1	+	434.256787
X	1	1	3/2	1	−	B	0	0	1/2	0, 1	+	434.254949
X	1	1	3/2	2	−	B	0	0	1/2	0, 1	+	434.254840
$A^2\Pi_{1/2}(\nu'=1,\ J'=1/2,\ +) \leftarrow X^2\Sigma^+(\nu=2,\ N=1,\ -)$ repumping												
X	2	1	1/2	0	−	A	1	−	1/2	0, 1	+	395.718928
X	2	1	1/2	1	−	A	1	−	1/2	0, 1	+	395.718978
X	2	1	3/2	1	−	A	1	−	1/2	0, 1	+	395.717218
X	2	1	3/2	2	−	A	1	−	1/2	0, 1	+	395.717108
$B^2\Sigma^+(\nu'=1,\ N'=0,\ +) \leftarrow X^2\Sigma^+(\nu=2,\ N=1,\ -)$ repumping												
X	2	1	1/2	0	−	B	1	0	1/2	0, 1	+	434.933995
X	2	1	1/2	1	−	B	1	0	1/2	0, 1	+	434.934045
X	2	1	3/2	1	−	B	1	0	1/2	0, 1	+	434.932285
X	2	1	3/2	2	−	B	1	0	1/2	0, 1	+	434.932175
$A^2\Pi_{1/2}(\nu'=1,\ J'=1/2,\ +) \leftarrow X^2\Sigma^+(\nu=0,\ N=1,\ -)$ off-diagonal pumping												
X	0	1	1/2	0	−	A	1	−	1/2	0, 1	+	470.115819
X	0	1	1/2	1	−	A	1	−	1/2	0, 1	+	470.115873
X	0	1	3/2	1	−	A	1	−	1/2	0, 1	+	470.113971
X	0	1	3/2	2	−	A	1	−	1/2	0, 1	+	470.113870

Chapter 3: Cryogenic Buffer Gas Beam Source

To perform laser cooling, we need to first prepare the molecules in a single quantum state, for CaH it is $X^2\Sigma^+(v = 0,\ N = 1,\ -)$. The rotational constant of CaH B_v is ~100 GHz, which corresponds to a temperature of ~10 K. In this case, if starting from a room temperature sample, many rotational states could be thermally populated. A cold, bright, and slow molecular beam is required. In this chapter, I describe our cryogenic buffer gas beam (CBGB) source, and how we managed to improve it to a level that ultimately enabled a MOT of CaH.

3.1 CaH_2-Based Beam Source

CBGB sources use buffer gas at cryogenic temperatures, typically at ~4 K if using He and ~15 K if using Ne, to cool the atoms or molecules of interest. For laser cooling and trapping experiments, people typically choose He for its colder temperature and potentially slower forward velocity. We use a CRYOMECH PT415 pulse tube refrigerator. There are two cooling stages in the system. The first goes down to ~40 K, which has a larger heat load capacity and serves as a radiation shield from the room temperature environment. The second stage goes down to ~3 K with a smaller heat load capacity. In practice, the coldest temperature that has been reached in our system is ~4.3 K, which corresponds to ~1 W of heat load on the first stage according to the capacity curve of the pulse tube. And the buffer gas cell (where the molecules are produced) is even hotter at ~6 K. Part of the reason is that our cryogenic system was originally designed with an unnecessarily large size, and it turned out that, no matter how much effort we put into improving the radiation shielding, we could not cool it below 4 K. Honestly, this has been a long-standing concern during my PhD, since CBGB sources typically work much better at ~3 K. The concern has been alleviated by further investigation. First, CaH has a larger rotational constant compared to all

other laser-cooled molecules, and as a result, the ($N = 1$) population peaks at a higher temperature ~10 K. We observe that the CaH production increases with higher temperatures (from 6 K to 10 K). Second, the forward velocity scales with $\sqrt{T}$, and we find that our forward velocity is not dramatically higher compared to those operating at ~3 K under similar experimental conditions. Nevertheless, these still do not justify operating at suboptimal conditions. For the next generation of the experiment, this problem should be solved as it should ultimately lead to the highest possible molecular beam flux.

3.1.1 Buffer Gas Cell

The CaH molecules are generated in a so-called cryogenic buffer gas cell. For the first attempt as other laser-cooled molecules, the molecules are generated through laser ablation of the corresponding chemically-stable compounds, in our case it is CaH_2. The ablation can break one of the Ca–H bond and produce CaH radicals. Since this is an explosive process, the resulting CaH molecules are at very hot temperatures ~10^3 K. The molecules could then be buffer gas cooled with the He introduced to the cell at ~6 K. With a hole in the front of the buffer gas cell, the molecules can be extracted with the buffer gas and form a molecular beam. This is illustrated in Fig. 3.1(a). Simple as it may seem, there are a considerable number of parameters that needs to be finely tuned for different types of experiments.

Buffer gas cells are evaluated in several aspects: production, extraction, and forward velocity. The molecule production in cell can be monitored through laser absorption, and the molecular beam properties can be measured with laser-induced fluorescence (LIF) on either electron-multiplying charge-coupled device (EMCCD) camera with spatial resolution or on a photomultiplier tube (PMT) with temporal resolution. During my PhD, we have tried several different designs of buffer gas cells for an optimized performance. The first one is an old design from the early time of this project [111]. Back then, the team was trying to laser cool and trap BaH molecules. However, due to some unfavorable properties of the molecule, including low molecular production, small optical force and the existence of metastable states that could potentially reduce the photon

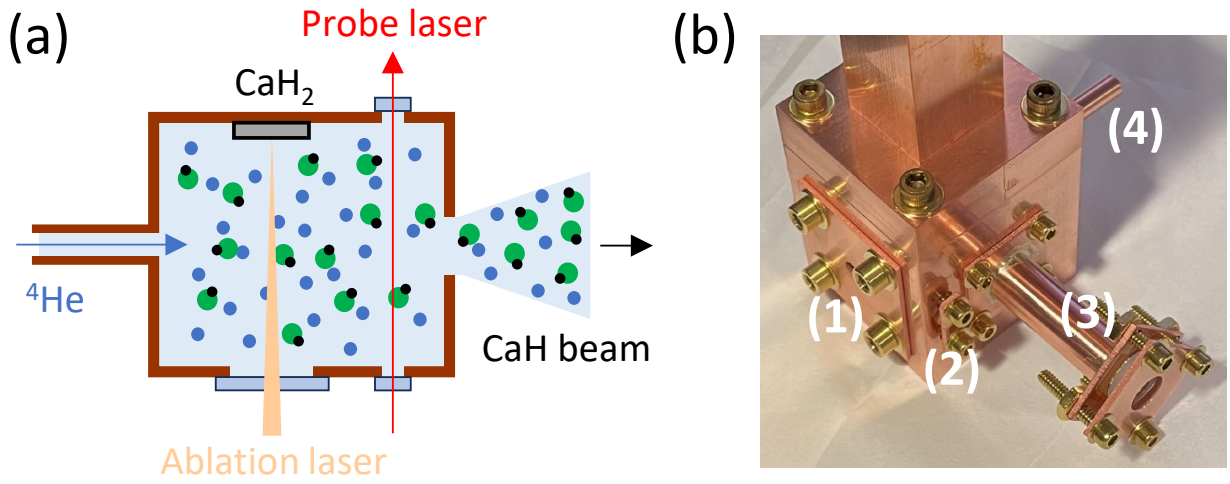

Figure 3.1: (a) Schematic of the cryogenic buffer gas cell for the production of a CaH molecular beam. CaH molecules are generated through a pulsed Nd:YAG laser ablation on a CaH_2 target. The hot CaH molecules are then buffer gas cooled with He at ~6 K and extracted from the cell to form a molecular beam. The molecule production in cell can be monitored with laser absorption. (b) Image of a cell. (1) the aperture for molecular beam extraction; (2) a small window for the probe laser; (3) a snorkel to hold the window for the ablation laser; and (4) the gas fill line.

budget, the team decided to switch to CaH. There were a few problems with this cell. First, the cell has not been cleaned for years and is coated with black Ba-containing compounds (Ba or BaH_2 oxidized by air). Second, it is not easily extendable, especially given the fact that the gas fill line is welded permanently to the cell body. There was a good reason to not clean it: some dirtiness in the cell helps with the overall molecule production. This can be more helpful for hydrides given the higher temperature needed for a higher ($N = 1$) population, the dirtiness might lead to a poor thermalization and thus increases the molecule production in the ($N = 1$) state. For BaH this is particularly important because of the already low molecule production. Because of its large mass, the forward velocity was not affected dramatically, and was peaking at ~150 m/s. However, when we changed to CaH, due to the smaller mass, the forward velocity is way faster, peaking at ~400 m/s, and cleaning the cell did decrease the velocity, but at the cost of dramatically lower molecule production. On the other hand, relying on an uncontrolled coating without proper cleaning is not a viable long-term solution. Considering these limitations, we adopted a newer design, similar to that of the CaF Gen II experiment in the Doyle group at Harvard University [112], and an image

of it is shown in Fig. 3.1(b). All characterization and optimization below are performed with this design.

3.1.2 He Flow Dependence

Our cell is similar to those of other well-established CBGB sources [52, 113, 114], with cell inner diameter and length at 1 inch and 2 inches, cell aperture diameter at 5 mm, He flow rates at several standard cubic centimeters per minute (SCCM), and YAG ablation energies at ~10 mJ. CBGB sources typically operate in between the effusive and supersonic regime, or the intermediate regime. This is because the intermediate regime allows decent buffer gas cooling to bring the hot molecules close to the buffer gas temperature, while not "boosting" the forward velocity of the molecular beam much by the collisions with the buffer gas near the cell aperture. In this regime, the forward velocity increases with the He buffer gas flow rate [52], as shown in Fig. 3.2. We measure Ca velocity through the LIF on the $4s4p\ ^1P_1 \leftarrow 4s^2\ ^1S_0$ transition at 423 nm, with the laser applied 45°with respect to the molecular beam and ~80 cm downstream from the cell. The LIF is measured on a PMT with temporal resolution. Figure 3.2(a) shows an example of the measurement, with He flow rate at 17.6 SCCM and YAG ablation energy at 12 mJ. Normalized

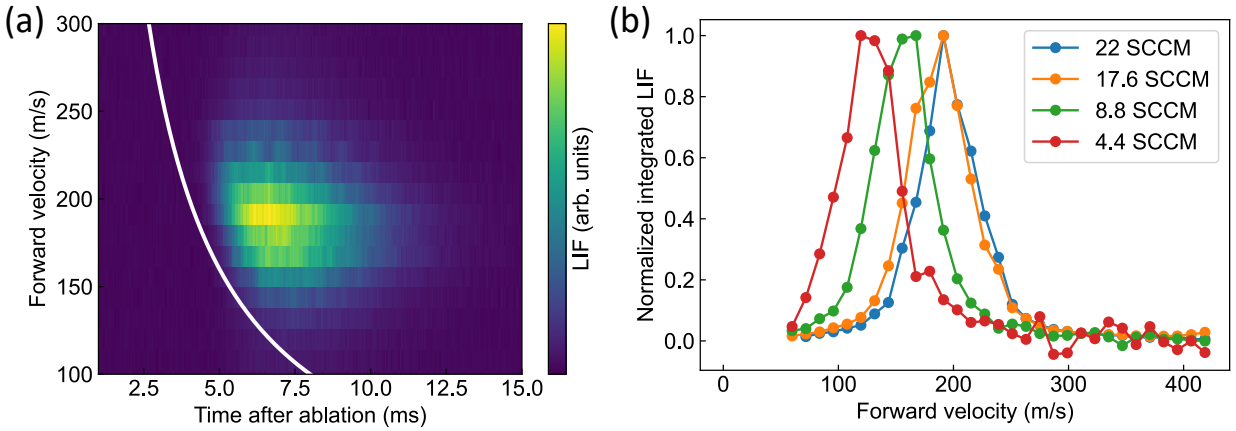

Figure 3.2: (a) LIF on the $4s4p\ ^1P_1 \leftarrow 4s^2\ ^1S_0$ transition of Ca at different velocities detected on a PMT, measured with 17.6 SCCM He flow rate and 12 mJ YAG ablation energy. The solid white line marks ballistic propagation from the cell and serves as a guide to the eye. (b) Normalized time-integrated LIF as a function of velocity at different He flow rates. An increase in the peak forward velocity is observed with increasing in He flow rate.

time-integrated LIF as a function of velocity at different He flow rates is summarized in Fig. 3.2(b). As expected, the peak forward velocity increases with He flow rate.

However, measurement of CaH velocity is nontrivial. The weak LIF for molecules is typically buried in the large scattering background in the vacuum chamber, especially if there is any in-vacuum parts such as in-vacuum magnetic-field coils and in-vacuum lens like in our system. A two-photon background-free (BGF) detection scheme is preferred for such measurements. Unfortunately, at the time when we performed these cell characterizations, we did not have the lasers necessary for the BGF measurement scheme. Details of this scheme will be discussed in Chapter 6: Laser Slowing of CaH. For now, we can assume CaH behaves similarly to Ca in terms of velocity given their similar mass, measuring Ca velocity is still an important benchmark.

In the intermediate regime, there is a zone of freezing, where the forward velocity of the molecular beam is boosted by the collision with the He buffer gas near the cell aperture. The higher the He flow rate, the longer this zone will be. And since the buffer gas density is very high in this region, laser cooling or slowing can not be performed as the molecules will be scrambled by the buffer gas. Ideally, one would want this region to be as short as possible. However, different from other laser-cooled molecules, CaH molecule production is at least an order-of-magnitude smaller, and we think this is probably due to the weaker Ca–H molecular bond and it is easy to break both bonds with ablation and leave only Ca atoms. As a result, we would need to operate at a higher He flow rate for a higher number of molecules. In practice, we would need to flow ~20 SCCM of He to have a decent signal-to-noise ratio (SNR) in the CaH beam, and the molecular beam flux is measured to be $\sim 10^{10}$ molecules/steradian/pulse in this case. For 1D laser cooling this high flow rate is fine since it is performed downstream anyway, but it might be a problem for slowing and MOT experiments since one would want to start slowing as early as possible. We learned from the SrF team that the MOT will vanish when the He flow rate exceeds ~10 SCCM [115]. This might seem hopeless at first glance, but in the end, laser slowing and MOT are performed with the chemical production method discussed later, let us not worry about it too early.

3.1.3 Ablation Protocol

The way we ablate also plays an important role in getting the highest molecular beam flux possible. To our surprises, tuning the focal point of the ablation laser in a specific way can help the overall production.

Starting from a new sample, the best molecule production occurs with the ablation laser tightly focused onto the surface of the sample (beam waist ~50 μm). However, we find that, if we keep ablating with a tightly focused laser in a small region without any He flow for a while, say for half an hour at a 10 Hz rate, defocusing the ablation laser later on will lead to an even higher number of molecules. We call this 10 Hz ablation process "surface preparation". One possible explanation of why this can work better is, the surface preparation "softens" the surface of the sample, and less fluence is required to ablate out the same amount of molecules per unit surface area, then the defocused ablation laser can address a larger area and produce more molecules. We have tried this for both CaH_2 and CaD_2 samples, we will see later that CaD_2 has a significantly higher production that could be attributed to the difference in the crystalline structure, but the surface preparation scheme works for both. We recommend anyone who struggles with molecule production to give it a try (well, hopefully the reader does not have to deal with this problem in the first place).

We have also tried different forms of CaH_2 samples, including rock samples and pressed powder samples. Interestingly, for hydrides, the denser rocks always work better, different from most other molecules that have been laser cooled.

3.1.4 Two-Stage Cell

An important technique that is now widely used in the community is the two-stage cell, where a second stage with a lower He density is attached to reduce the boosting effect near the cell aperture. Figure 3.3(a) shows a schematic of the two-stage cell. He density is reduced by the small gap after the first stage, then the molecules enter the second stage to get further thermalized. There is also opening on the side of the second stage to further reduce the He density. The extracted molecular beam from the second stage can then be in the effusive regime, where the boosting from He is

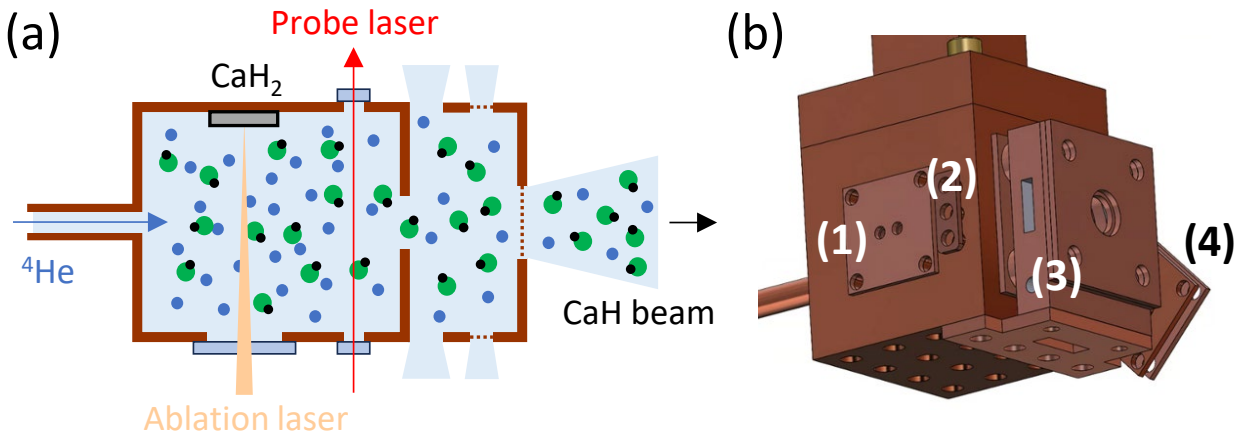

Figure 3.3: (a) Schematic of the two-stage cell. Before the second-stage cell, there exists a small gap to reduce the He density. The molecules then get further thermalized in the second stage and extracted to form a molecular beam in the effusive regime (b) Image of the design. (1) the target holder; (2) a small window for the probe laser; (3) the second-stage cell; and (4) the window for the ablation laser.

minimized. Figure 3.3(b) shows an image of the design viewed from a different angle compared to Fig. 3.1(b), and Fig. 3.3(b)(3) is the second-stage cell.

For the two-stage cell, we started with the parameters used in the CaF [116, 117] and CaOH [118] team in the Doyle group, including the length of the gap, dimensions of the second stage, pore sizes of the meshes. After several attempts to improve performance, we found that the gains, if any, are marginal to the level we care about, so we decided to keep the first version of the two-stage cell. In this configuration, Ca velocity at different He flow rates is measured in Fig. 3.4. The peak forward velocity is around 120–150 m/s, and it does not increase much with increasing He flow rates as what we would expect in the effusive regime. However, the two-stage cell cuts the CaH beam down by nearly an order of magnitude. This is not unexpected, but still, it turned out the SNR becomes too low in beam, we do not win much with two-stage cell for a CaH_2-based beam source.

3.2 Chemical Production

The CaH_2-based beam source not only produces a low flux, it is also not very stable. One spot on the target would not last for more than tens to hundreds of ablations, and the yield decays exponentially if keep ablating on the same spot. To solve this problem, following the community's

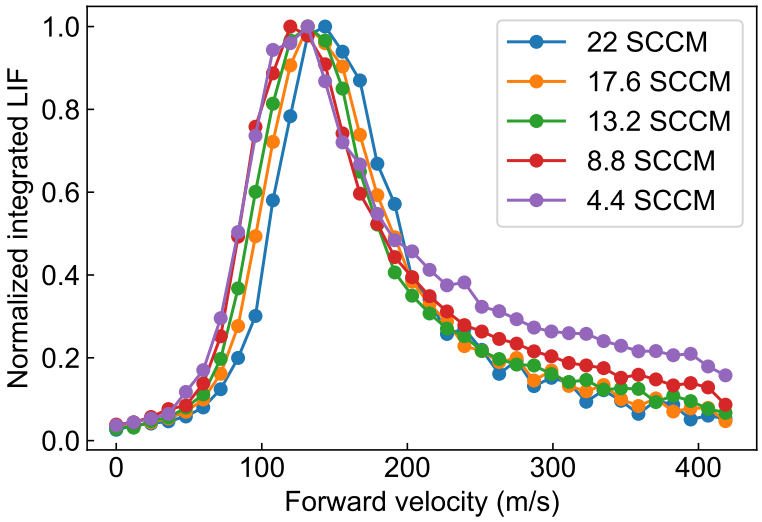

Figure 3.4: Velocity performance with two-stage cell. With increasing He flow rate, very minimal peak velocity change is observed, signaling the output molecular beam in the effusive regime.

consensus, we decided to try the chemical reaction method [119].

Reactions occurring within CBGB sources are generally barrierless or possess small energy barriers that can be overcome with thermal or optical excitation. For instance, Ca reacts exothermically with SF_6 to form CaF [120], while its reaction with H_2O to yield CaOH requires promoting the Ca atom to the metastable $^3P_1$ state in order to overcome an energy barrier of approximately 1.3 eV [77]. By contrast, if we use H_2 as a reactant, the reaction would have a considerably higher barrier of ~2.7 eV. To thermally overcome this barrier, temperatures on the order of 3×10^4 K would be needed, which is approaching the limits achievable through laser ablation. Consequently, one would anticipate the reaction to yield only a small amount of product. We investigate the reactions between Ca atoms and the isotopologues H_2, D_2, and HD, under conditions both including and excluding He as the buffer gas. Counterintuitively, our results show that the reaction proceeds much more efficiently than a simple thermodynamic estimate would suggest, emphasizing that reaction dynamics play a critical role compared to purely energetic considerations. Furthermore, we observe that H_2, but not D_2 and HD, acts effectively as a buffer gas, enabling the produced CaH molecules to thermalize into their rovibrational ground state. To interpret these observations, we developed a model of the reactant dynamics employing rate constants obtained from quasi-

classical trajectory (QCT) simulations in collaboration with Prof. Jesús Pérez Ríos at Stony Brook University. Our calculations elucidate the general trends observed in the experiment and provide an order-of-magnitude estimate of reaction rate constants.

3.2.1 Cell Design

For chemical production, we would need to flow in reactants at temperatures above their freezing point so that they do not clog the fill line. To achieve this, we modified our buffer gas cell by adding a thermally isolated gas fill line on the back, as shown in Fig. 3.5. An Nd:YAG laser is used to ablate on a solid Ca target instead of CaH_2 target to create a hot plume of Ca atoms. In this study, we also upgraded our Nd:YAG laser to a higher power version (refurbished by Anderson Lasers, Inc.) up to 200 mJ at 532 nm. We use laser absorption to probe the Ca atoms and product molecules. Specifically, Ca atoms are probed on the $4s4p\ ^3P_1 \leftarrow 4s^2\ ^1S_0$ transition at 657 nm, and CaH molecules are detected via the $A^2\Pi_{1/2}(v' = 0,\ J' = 3/2,\ +) \leftarrow X^2\Sigma^+(v = 0,\ N = 1,\ J =$

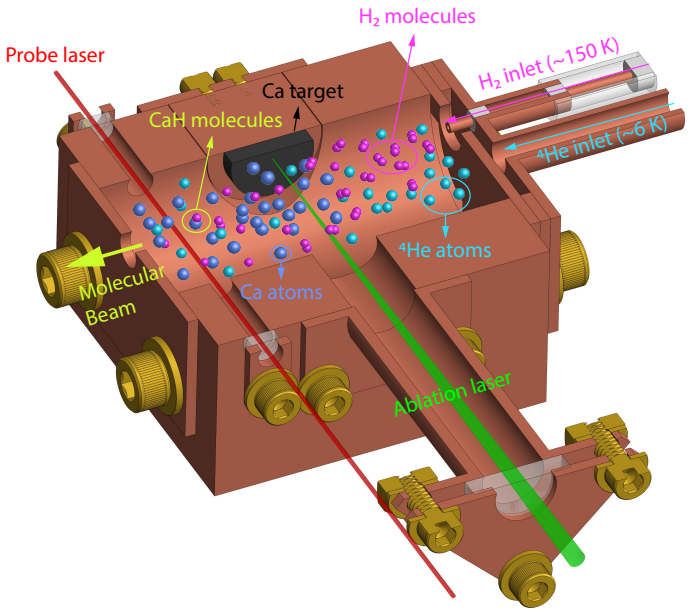

Figure 3.5: Horizontal cross section of the buffer gas cell modified for chemical production. An thermally isolated gas fill line is added to the back of the cell, where we can flow in various reactants such as H_2, D_2, and HD. Hot Ca atoms are generated via laser ablation of a solid Ca target and subsequently react to form CaH or CaD. Additionally, He flows in at ~6 K for efficient buffer gas cooling. The Ca atoms and the product molecules are probed through laser absorption.

$1/2,\ -$) transition at 695 nm.

3.2.2 Ca + H_2 Reaction

The Ca + H_2 chemical reaction is expected to be barely within reach in a CBGB source due to its endothermic nature. Surprisingly, we detect a substantial yield of CaH molecules in the $X^2\Sigma^+(v = 0,\ N = 1,\ -)$ state (~3–10×10^{10} molecules/steradian/pulse), which we attribute to the unique properties of cryogenic H_2: it can be both a reactant and a buffer gas. This will be discussed in detail later. The reaction occurs once the H_2 flow reaches a few SCCM (1 SCCM ≈ 4.5×10^{17} molecules per second) and plateaus at flow rates of several tens of SCCM. Figure 3.6 shows the measured total CaH density plotted against the initial Ca density. The Ca density is controlled by tuning the ablation energy, which simultaneously influences the temperature of the ablation plume. We carefully calibrate the internal state distribution at different ablation energies up to

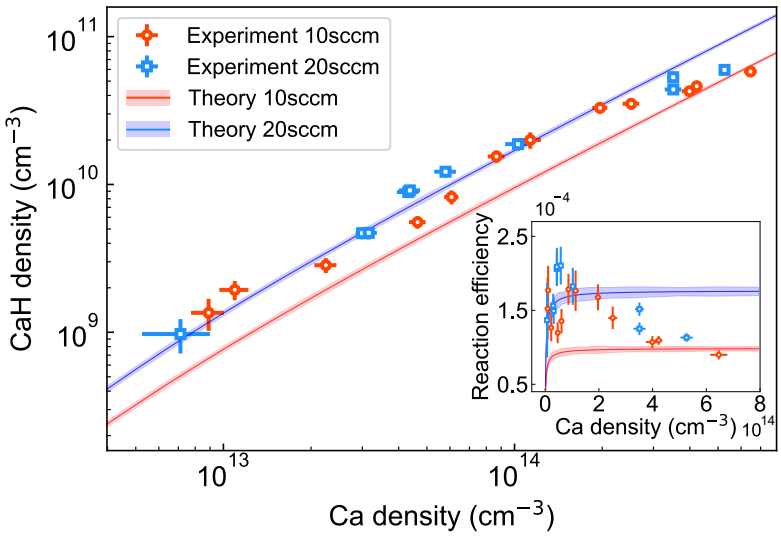

Figure 3.6: Chemical reaction in the buffer gas cell. Time-averaged CaH densities measured within 0–1 ms after ablation, plotted against Ca density for 10 SCCM of H_2 (red circles) and 20 SCCM of H_2 (blue squares), both under 2.2 SCCM of He. The lines denote theoretical results at the same conditions at a collision temperature of 2400 K, showing qualitative agreement. The inset shows the reaction efficiency, defined as the ratio of CaH to Ca densities. A notable decrease in reaction efficiency is observed experimentally at higher Ca densities, whereas the theoretical model does not capture this trend, showing the need for further refinement. Error bars on the experimental data correspond to 1-σ statistical uncertainties.

the highest populated level ($v = 0,\ N = 2$) (see Sec. 3.2.3) for the experimental conditions in Fig. 3.6, thereby concluding that the total CaH population across these states accounts for the total molecular yield. We develop a chemical reaction network model (lines in Fig. 3.6) based on rate constants obtained from QCT calculations (see Sec. 3.2.4). We find a constant plume temperature of ~2400 K, independent of Ca density, yields the best fit to the data. We verify this assumption by measuring the plume temperature without gas flow (see Sec. 3.2.4). Our measurements show a maximum 45(10)% increase in temperature with ablation energy, supporting the constant plume temperature assumption. We also note that plume temperature is the only fit parameter we use in the reaction network model.

We observe that the experimental data at different H_2 flow rates in Fig. 3.6 appear less well-separated than the theoretical predictions. In our model, we assume that the H_2 density increases linearly with flow rate, which is a simplification of the actual processes occurring in the cell. In reality, a significant portion of H_2 may condense onto the cold cell walls, forming solid H_2 ice, while sublimation from this ice layer can reintroduce H_2 into the gas phase. These dynamics may lead to transient and spatially inhomogeneous gas densities, but they are difficult to model and lie beyond the scope of this work. Experimentally, we also observe that CaH production remains substantial even after the H_2 flow is turned off, further supporting the presence of residual H_2 vapor from sublimation. These effects may contribute to the reduced sensitivity of CaH yield to the H_2 flow rate observed in the experiment.

Although the experimental data generally agree with the reaction model predictions, noticeable deviations arise at higher Ca densities. As shown in the inset of Fig. 3.6, the reaction efficiency, or the fraction of Ca atoms converted into CaH molecules, decreases as the Ca density increases. In contrast, the model predicts that the reaction efficiency should plateau at higher densities. These losses may be attributed to nonequilibrium processes that are not included in the simplified model, for instance, the formation of denser ionic species such as Ca^+ within the plasma can enhance the likelihood of subsequent ionization of CaH, thereby reducing the overall yield.

3.2.3 Rotational Temperature

The total density of cold CaH molecules is converted from that in the $X^2\Sigma^+(v = 0,\ N = 1,\ J = 1/2,\ -)$ state with rotational temperature measurements. Figure 3.7(a) shows the measured relative absorption of $X^2\Sigma^+(N = 0)$ and $X^2\Sigma^+(N = 2)$ states with respect to $X^2\Sigma^+(N = 1)$ for varying ablation pulse energies. The transitions involved in these measurements are $A^2\Pi_{1/2}(v' = 0,\ J' =$

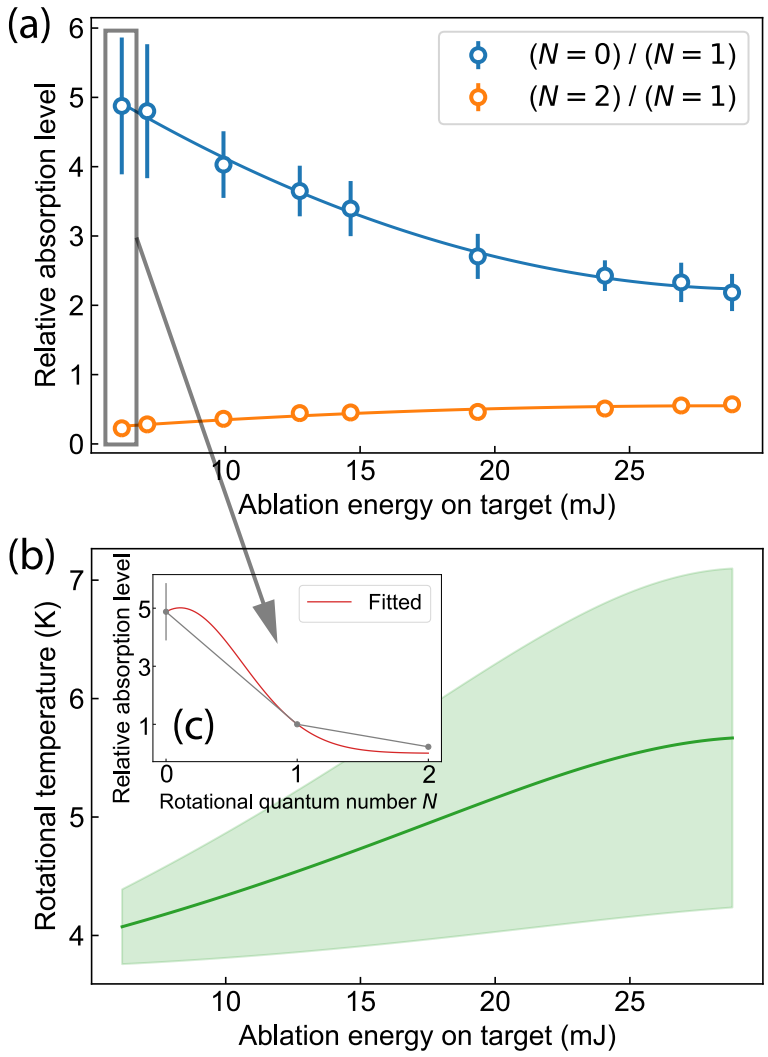

Figure 3.7: (a) Relative in-cell absorption for $X^2\Sigma^+(N = 0)$ and $X^2\Sigma^+(N = 2)$ states with respect to $X^2\Sigma^+(N = 1)$, versus ablation pulse energy. Absorption for $X^2\Sigma^+(N = 3)$ and higher rovibrational states is below the detection limit and therefore neglected. Solid lines are fitted quadratic functions to guide the eye. (b) Fitted rotational temperature versus ablation pulse energy. Temperatures are extracted from a least-squares fit according to Eq. (3.1), as shown in inset (c). The wide green band represents the 2-σ uncertainties from the fit.

$1/2,\ -) \leftarrow X^2\Sigma^+(v = 0,\ N = 0,\ J = 1/2,\ +)$, $A^2\Pi_{1/2}(v' = 0,\ J' = 3/2,\ +) \leftarrow X^2\Sigma^+(v = 0,\ N = 1,\ J = 3/2,\ -)$, and $A^2\Pi_{1/2}(v' = 0,\ J' = 5/2,\ -) \leftarrow X^2\Sigma^+(v = 0,\ N = 2,\ J = 5/2,\ +)$, for the states with $N = 0$, 1, and 2, respectively. Note that numbers in Fig. 3.7(a) should not be directly interpreted as population ratios. We fit the relative absorption values to extract the corresponding rotational temperature via the expression

$$P \propto S \times d \times e^{-BN(N+1)/k_BT}, \tag{3.1}$$

where P, S, d, and B denote the absorption, the Hönl-London factor, the degeneracy of the respective hyperfine magnetic sublevels, and the ground-state rotational constant, respectively, and k_B is the Boltzmann constant. The fitted rotational temperature as a function of ablation energy is shown in Fig. 3.7(b), with the inset (c) showing a sample fit. With the knowledge of the rotational temperature, we can use the population in the $X^2\Sigma^+(N = 1)$ state to predict the population in all occupied rotational states. Figure 3.6 is showing the converted total density.

3.2.4 Theoretical Interpretation

Reaction Network Model

In the reaction model, hot neutral Ca atoms collide with H_2 molecules, leading to vibrational excitation of H_2 and formation of CaH. Although H_2 flows into the cell at 150 K, it rapidly thermalizes via collisions with He to 6 K where nearly all the molecules are in the ground rovibrational state. The cold H_2 gas in the CBGB source is assumed to be in the ground vibrational state initially. Assuming a homogeneous mixture of gases, the vibrational quenching via inelastic collisions can be represented by

$$H_2(v) + \mathrm{Ca} \underset{k^q_{v'\to v}(T_{\mathrm{Ca}})}{\overset{k^q_{v\to v'}(T_{\mathrm{Ca}})}{\rightleftharpoons}} H_2(v') + \mathrm{Ca}, \tag{3.2}$$

where up to ($\nu' = 2$) are included. The reactive process representing the formation of CaH in all rovibrational states is described as

$$H_2(\nu) + Ca \xrightarrow{k_\nu^r(T_{Ca})} CaH + H, \tag{3.3}$$

where ν represents the vibrational level of H_2, with up to ($\nu = 2$) included. The state-to-state quenching rate constants (k^q) and reaction rate constants (k^r) are calculated via the QCT method. Rotational excitation is neglected, as our simulation shows that vibrational excitation has a more significant effect on the reaction rate than rotational excitation. This can be attributed to the far more efficient vibration-translation coupling compared to rotation-translation coupling [121]. The inelastic rate constants, summed over all final rotational states, and the reactive rate constants, summed over all final rovibrational states, are shown in Fig. 3.8(a).

We use a deterministic approach to study the evolution of these reactions in a closed system at thermal equilibrium by solving the set of differential equations associated with Eqs. (3.2)–(3.3). The evolution of CaH and H_2 vibrational state densities is given by

$$\frac{dn_{CaH}}{dt} = \sum_{\nu=0}^{2} k_\nu^r n_{H_2(\nu)} n_{Ca} \tag{3.4}$$

and

$$\frac{dn_{H_2(\nu)}}{dt} = -k_\nu^r n_{H_2(\nu)} n_{Ca} + \sum_{\nu' \neq \nu} (k^q_{\nu' \to \nu} n_{H_2(\nu')} n_{Ca} - k^q_{\nu \to \nu'} n_{H_2(\nu)} n_{Ca}), \tag{3.5}$$

where $n_{H_2(\nu)}$, n_{CaH}, and n_{Ca} represent the density of H_2 molecules in vibrational state ν, CaH molecules, and Ca atoms in the cell, respectively. A sample dynamics of the densities is shown in Fig. 3.8(b).

Buffer gas thermalization properties due to elastic collisions are included. The hot Ca atoms thermalize according to

$$\frac{dT_{Ca}}{dt} = -\frac{R_{H_2}(T_{Ca} - T_{H_2})}{\kappa_{H_2}} - \frac{R_{He}(T_{Ca} - T_{He})}{\kappa_{He}}, \tag{3.6}$$

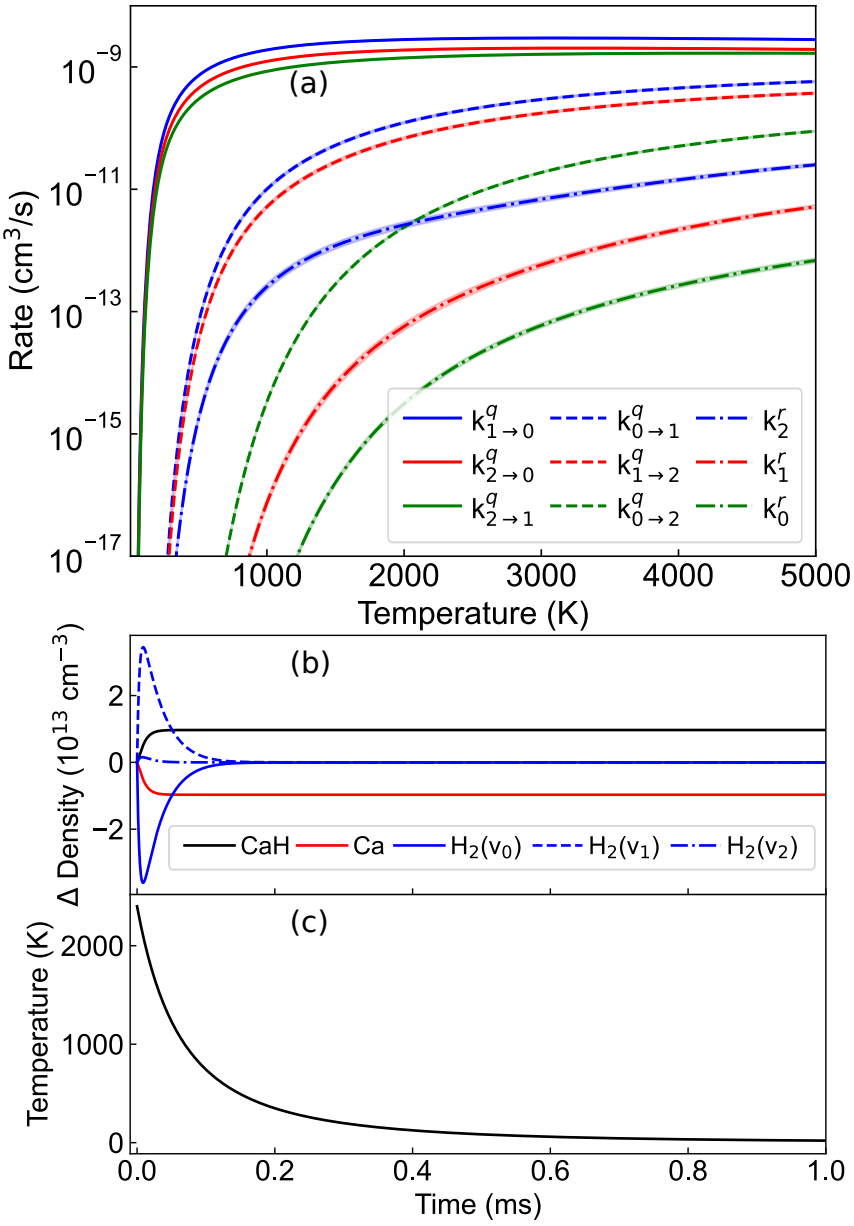

Figure 3.8: (a) QCT calculated temperature-dependent state-to-state vibrational rate constants for H_2 ($k^q_{v\to v'}$), where the subscripts denote the initial and final vibrational states, and formation of CaH (k^r_v), where the subscript denotes the initial vibrational state of H_2. (b) Sample solution to the reaction model at 2400 K showing the change in number density over time relative to the initial densities. The Ca and CaH densities are scaled up by a factor of 500 for visualization. (c) Kinetic temperature of Ca over time, decaying due to elastic collisions with buffer gases H_2 and He.

which dictates the kinetic temperature of collisions. Here, $R_{\mathrm{BG}} = n_{\mathrm{BG}}\sigma^{el}_{\mathrm{BG}}\bar{v}_{\mathrm{BG}}$ is the elastic collision rate between Ca and buffer gas BG, where n_{BG} is the density of the buffer gas, $\sigma^{el}_{\mathrm{BG}}$ is the elastic cross section, and $\bar{v}_{\mathrm{BG}}$ is the average relative velocity between Ca and the buffer

gas. T_{Ca} is the temperature of the ablated Ca, T_{BG} is the buffer gas temperature, and $\kappa_{\mathrm{BG}} = (m_{\mathrm{Ca}} + m_{\mathrm{BG}})^2/(2m_{\mathrm{Ca}}m_{\mathrm{BG}})$. Temperature of Ca decaying due to collisions with H_2 and He is presented in Fig. 3.8(c)

QCT Simulations

We use the QCT method [122, 123] via the PyQCAMS [124] software to calculate the energy-dependent cross sections of processes involved in collisions between ground-state Ca and H_2, which are required to solve Eqs. 3.4–3.5. The particle motion is treated classically, such that the trajectories are found using Hamilton's equations of motion. The internal states are treated according to the Bohr-Sommerfeld quantization rule, which quantizes the classical action into discrete energy levels. Thus, we gain insight into state-to-state cross sections of relevant processes, such as vibrational excitation or quenching of H_2, or a reaction leading to CaH formation, at variable collision energies. The energy-dependent cross section for a process p is calculated via

$$\sigma_p(E_c) = 2\pi \int_0^{b_{max}} \mathcal{P}_p(E_c, b) b db \tag{3.7}$$

where $\mathcal{P}_p(E_c, b) = \frac{N_p}{N_t} \pm \frac{N_p}{N_t}\sqrt{\frac{N_t - N_p}{N_t}}$ represents the probability of process p occurring from N_t collisions for a given collision energy E_c and impact parameter b. The uncertainty represents one standard deviation associated with the Boolean Monte Carlo process for calculating $\mathcal{P}_p(E_c, b)$. Here, process p can represent rovibrational quenching, formation of a new molecule, or dissociation of the initial molecule. The integral is calculated after randomizing initial conditions for a sufficient number of trajectories. The reaction rate of the collision is then calculated as the product of the cross section and the collision velocity,

$$k_p(E_c) = \sigma_p(E_c)\sqrt{\frac{2E_c}{\mu}}, \tag{3.8}$$

where $\mu = m_{\mathrm{Ca}}m_{\mathrm{H_2}}/(m_{\mathrm{Ca}} + m_{\mathrm{H_2}})$ is the reduced mass of the colliding particles. For an appropriate Maxwell-Boltzmann distribution of energies, we calculate the temperature-dependent rate

constants of these processes,

$$k_p(T) = \frac{2}{(k_B T)^{3/2}} \int k_p(E_c) \sqrt{\frac{E_c}{\pi}} e^{-E_c/k_B T} dE_c. \tag{3.9}$$

The calculated temperature-dependent rates are presented in Fig. 3.8(a).

All the above discussions regarding the reaction model and QCT simulations are just to provide an picture of how they work. For a more detailed description and the code, the reader is referred to our collaborator Rian Koots' thesis [125].

Ablation Plume Temperature

We have measured the dependence of the ablation plume temperature on the ablation energy when there is no gas flow in the system, as shown in Fig. 3.9. The temperature of the ablation plume is determined by analyzing the measured absorption linewidth of the Ca $4s4p\ ^1P_1 \leftarrow 4s^2\ ^1S_0$ transition at 423 nm. While the Ca yield remains stable during the measurement, we sweep the

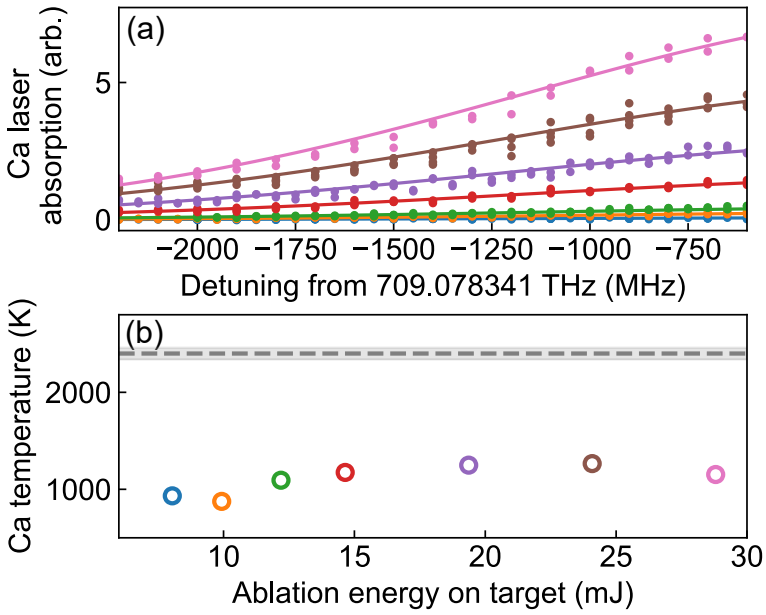

Figure 3.9: (a) Ca absorption spectra at different ablation energies. The data is fitted with the Gaussian function. (b) The Ca plume temperature versus ablation energy (error bars not visible at this scale). The gray shaded area represents the theoretical temperature 2400(60) K that optimally matches the experimental results in Fig. 3.6.

frequency of the 423 nm laser through the cell and observe a Gaussian-shaped absorption spectrum. Its linewidth is influenced by various line-broadening mechanisms which we carefully consider to identify the dominant contributor.

The natural linewidth of the transition is ~30 MHz. Collisional broadening is negligible here due to the low density of the buffer gas in the cell, and power broadening is minimal due to the low intensity of the probe laser light. Consequently, the dominant broadening mechanism is attributed to the Doppler effect. The measured linewidth of ~1 GHz is significantly larger than any of the other broadening contributions, allowing us to directly translate the linewidth to temperature.

It is important to note that the measured temperature represents a lower bound on the actual translational temperature of the ablation plume. In nonequilibrium systems such as the CBGB source, the translational temperature is anisotropic: the temperature along the direction of ablation is typically higher than the temperature perpendicular to it [126]. Based on our QCT simulations, a temperature of 2400(60) K provides the best fits to the experimental data. We therefore estimate this value to be near the average plume temperature in our system.

3.2.5 H_2 as a Buffer Gas Coolant

With H_2, substantial yields of thermalized Ca atoms and CaH molecules are detected, even in the absence of He as a buffer gas (Fig. 3.10, green). As a comparison, when HD or D_2 is supplied, the thermalized Ca yield drops significantly, and CaH (or CaD) production falls below our detection limits (Fig. 3.10, yellow and red). These findings highlight the advantages of H_2 as a reactant and cooling medium in CBGB systems.

These observations may be attributed to the exceptionally high saturated vapor pressure of H_2 at cryogenic temperatures. For example, at 6 K the vapor pressure of H_2 reaches ~1.5 mTorr, which is a few orders of magnitude above that of HD (4.0×10^{-2} mTorr) and D_2 ($1.5{\times}10^{-3}$ mTorr) [127, 128]. This high vapor pressure allows a sufficient density of H_2 in the gas phase, allowing more productive collisions with Ca atoms before adhering to the cell walls or exiting the cell, thereby facilitating efficient thermalization and chemical reactions. In comparison, HD and D_2 condense

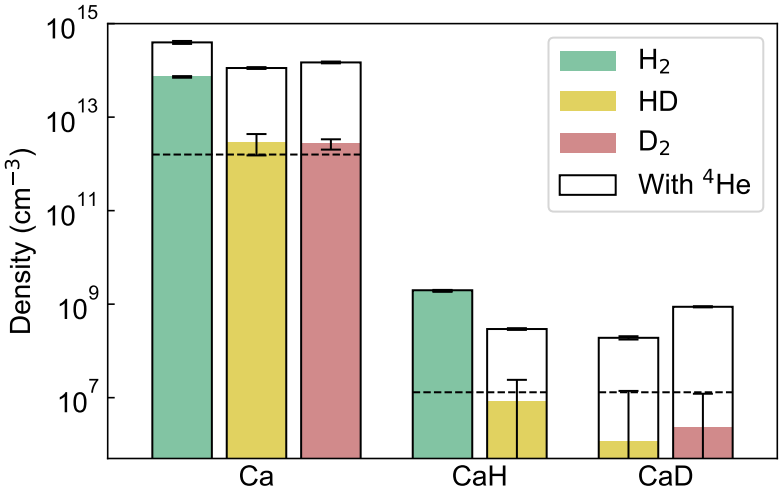

Figure 3.10: Time-averaged densities (0–1 ms after ablation) of Ca and CaH (or CaD) under different gas flow configurations. Reactant gases H_2, HD, or D_2 are supplied at 20 SCCM, with He (if used) added at 8.8 SCCM. Ablation energy is 19 mJ per pulse. Green, yellow, and red bars represent results for H_2, HD, and D_2, respectively, while black-framed bars show the yields with He added. Dashed lines indicate the detection limits, defined as the lowest density detectable with SNR > 2, below which measurements are statistically consistent with zero. Relative errors are larger when signals are close to the detection limit. Here the measured densities of CaH and CaD are those in the $X^2\Sigma^+(v = 0,\ N = 1,\ J = 1/2,\ -)$ states.

rapidly due to lower vapor pressures, resulting in insufficient collisions with Ca. Moreover, QCT simulations show that CaD formation in a D_2 environment is reduced by 30% relative to CaH production under H_2, which can be attributed to the larger mass of D_2. Further descriptions of the observed change in reactivity across isotopes may require a more rigorous quantum mechanical study.

Adding cryogenic He to the system increases the yields of thermalized Ca atoms and CaH molecules for all three reactants (black-framed bars in Fig. 3.10). This enhancement likely comes from the high efficiency of He to thermalize the gas mixture and provide hydrodynamic entrainment [52], thereby creating a more homogeneous environment in the cryogenic cell that improves detection of Ca and CaH. Therefore, introducing He into the system helps mitigate the constraints from the lower vapor pressures of HD and D_2. Note that the increase in CaH molecular yield is less than 22(1)%, substantially lower than the corresponding increase in thermalized Ca yield in the presence of He, which is typically greater than 440(40)%. This may result from a more rapid

cooling of Ca atoms when cryogenic He is present, which subsequently lowers the efficiency of the chemical reaction.

3.2.6 Collisional Cross Sections

Elastic collisions play a pivotal role in the thermalization process of CBGB systems. Larger elastic cross sections correspond to higher collision rates, facilitating rapid thermal equilibration of translational degrees of freedom. Inert gases like He and Ne are commonly selected as buffer gases because of their relatively large elastic collisional cross sections with various molecular species, on the order of 10^{-14} cm^2. Motivated by the pronounced cooling effect observed with H_2, we investigate the elastic cross sections of H_2, HD, and D_2 in collisions with Ca and CaH.

We use an approach adapted from Ref. [52]. We assume that particles either stick to the cell walls or exit through the cell aperture via a diffusion process when the density of buffer gas is low. By monitoring the decay of the signal over time, we estimate the diffusion time constant and consequently derive the elastic collisional cross section. The diffusion time constant is extracted by fitting an exponentially decaying function to the later part of the absorption time trace as illustrated in Fig. 3.11(a). The elastic collisional cross section is then

$$\sigma = \frac{9\pi v_{\mathrm{BG}} \tau}{16 A_{\mathrm{cell}} n_{\mathrm{BG}}}, \tag{3.10}$$

where $v_{\mathrm{BG}} = \sqrt{8 k_B T_0 / \pi m_{\mathrm{BG}}}$ is the expected speed of the buffer gas which follows the standard Maxwell-Boltzmann distribution, τ is the fitted diffusion time constant, A_{cell} is the cross-sectional cell area of ~5 cm^2, and n_{BG} is the density of the buffer gas. The density is set by controlling the flow as $n_{\mathrm{BG}} = 4 f_{\mathrm{BG}} / (v_{\mathrm{BG}} A_{\mathrm{aperture}})$, where f_{BG} is the flow rate of the buffer gas into the system and A_{aperture} is the aperture size of the buffer gas cell of ~0.25 cm^2.

The data is presented in Fig. 3.11. In order to reduce measurement errors, we select multiple ablation spot and flow rate combinations and statistically average the results. Given the low densities of Ca and CaH (or CaD) when using the HD and D_2 gases, we average these measurements

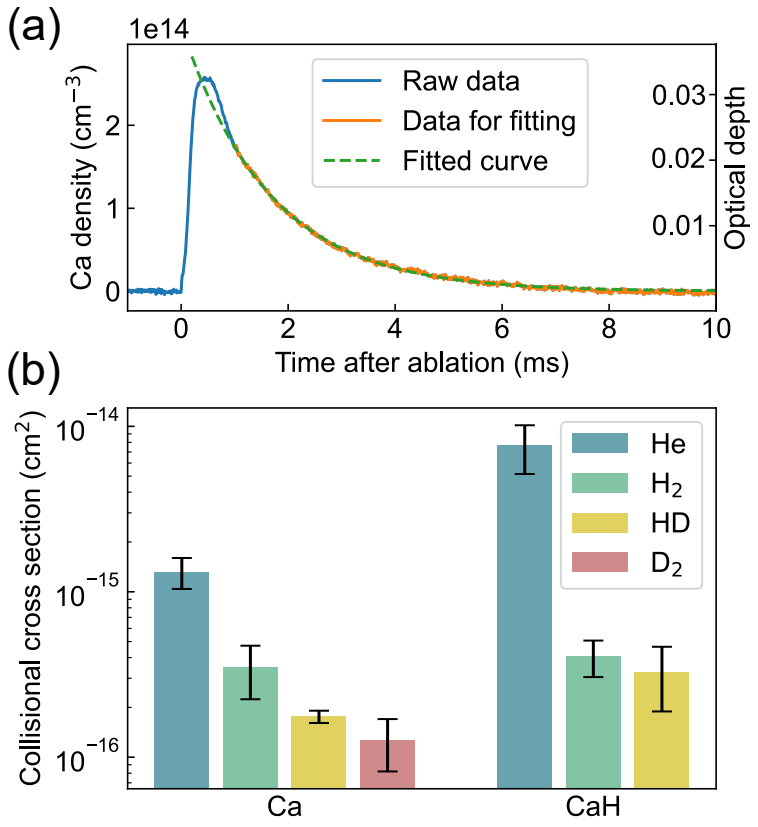

Figure 3.11: (a) A Ca density trace as a function of time after the ablation pulse (average of 30 shots). The blue curve is the original data, the orange line highlights the data used for fitting, and the green dashed line indicates the fitted single exponential decay result. This data is obtained with 8.8 SCCM He flow. (b) Measured collisional cross sections of He, H_2, HD, and D_2 with Ca and CaH.

more extensively. Noticeable shifts in the background signal were observed during measurements involving H_2, HD, and D_2, likely due to sublimation of ice deposits on the cell windows. This was accounted for by including a constant offset in the exponential fit. Ultimately, we have measured the elastic cross section of H_2 with CaH to be $4.1(1.0) \times 10^{-16}$ cm^2. This is high enough for efficient translational cooling in a regular buffer gas cell. The measured rovibrational temperature of CaH with H_2 shown in Sec. 3.2.3 also provides evidence for efficient cooling with H_2.

3.3 Beam Source Comparison

Up to this point, the feasibility of the chemical production method for CaH is demonstrated, despite the endothermic nature. The question now is, whether it is working better than the CaH_2-

based source. The first important part we have already seen is the higher molecular flux, up to 10^{11} molecules/steradian/pulse. The other important characteristic is the forward velocity, since one would want as bright and as slow of a beam as possible for slowing and trapping experiments. However, we find that the chemically produced CaH beam appears to be faster, as can be inferred from the arrival time in Fig. 3.12(b). The LIF is measured on a PMT ~1 m downstream from the cell and the cell is in the single-stage configuration.

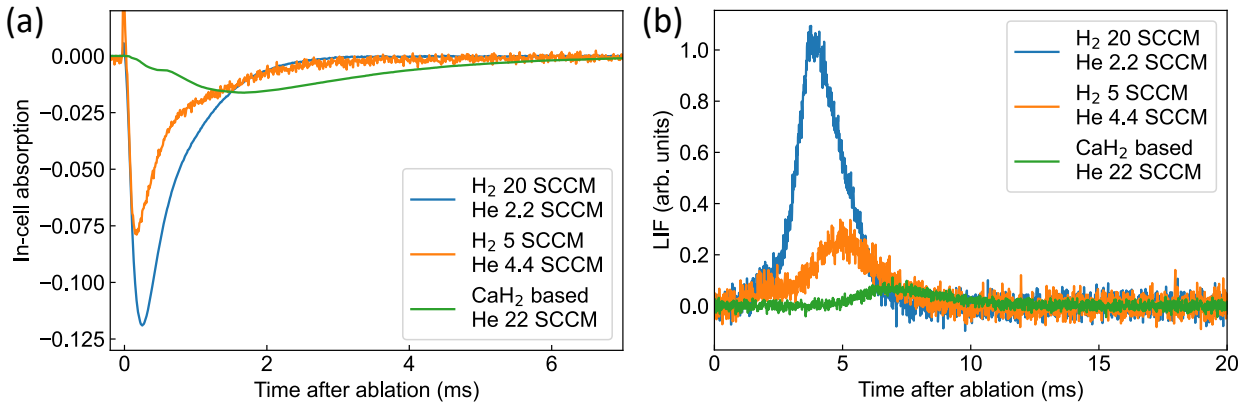

Figure 3.12: CaH_2-based and chemically produced source detected in cell and in beam. (a) CaH density measured with laser absorption in cell. Chemically produced CaH shows a faster extraction. (b) In-beam LIF measured ~1 m downstream from the cell.

The earlier arrival time may not immediately mean a faster velocity. It turns out that the chemically produced CaH molecules have a very fast extraction from the cell. This is measured through laser absorption in cell in Fig. 3.12(a). Chemically produced CaH extracts from the cell within a millisecond while it takes the CaH_2-based source ~5 ms for the molecules to completely extracted from the cell. Through the Ca velocity in the chemical production configuration, we confirmed that the velocity peaks at ~250–300 m/s, which is not significantly faster than the CaH_2-based source. However, the peak forward velocity cannot be reduced much by reducing the H_2 flow rate as what we saw with the CaH_2-based source when we reduce the He flow. This is understandable since H_2 serves also as a buffer gas, and the forward velocity may be affected by H_2, and its mean velocity at ~6 K is faster at the ~300 m/s level given its light mass. Two-stage cell is also not able to reduce the forward velocity. These observations indicate that H_2 is probably dominating the cell

dynamics. But surprisingly, two-stage cell would not reduce the overall molecular beam flux for the chemical production, but just showing a better buffer gas cooling behavior measured with Ca atoms (more concentrated in velocity and broader in arrival time). Although subtle, we keep the two-stage cell for chemically produced CaH beams.

Another important improvement for chemically produced beams is their stability. Compared to CaH_2-based source, the exponential decay time constant of molecule number for chemically produced source is measured to be ~20 times longer. However, it still has variation depending on how much H_2 ice is in the system. A newly loaded sample without any H_2 ice would require a higher flow of H_2 to start seeing a healthy number of molecules. However, if one can be more patient and flow a smaller amount, say ~1 SCCM, they would observe the yield going up and saturating after a day or two of operation. After a long period of operation (a week or so), the molecule number will start going down again, probably because of the ice accumulation. A warm up and cool down cycle would bring the molecule number back up again.

Taking into account all of this, despite the quirkiness of H_2, chemically produced CaH beam source still is the most promising way forward. Moreover, it also turns out that it is the unique property of H_2 that make the CaH production more efficient. We have tried other candidate reactants that may have smaller enthalpies for producing CaH, including CH_4, H_2O, and H_2O_2, none of these produces a number even comparable to the CaH_2-based source. So in the end, for all slowing and MOT experiments shown later, we are using the H_2-based chemical production source.

Chapter 4: Laser Cooling of CaH

When choosing a new molecule, the first experiment to test its feasibility for laser cooling is to do 1D cooling on a molecular beam. At this stage, we would like to confirm the quasi-closed photon cycling scheme is actually working, without significant losses that could limit the photon budget. Additionally, a high photon scattering rate is also needed to achieve a strong radiative force for laser slowing and trapping. In this chapter, I describe the early proof-of-principle measurements that confirmed these aspects for CaH.

4.1 Relevant Experimental Hardware

4.1.1 Laser Systems

Up to the point when this thesis is written, there have been different generations of laser systems on this project. From home-built external-cavity diode lasers (ECDLs) and injection-locked lasers (ILAs) to commercial fiber amplifiers, sum-frequency generation (SFG) systems, second-harmonic generation (SHG) systems, Ti-Sapphire lasers, and this list keeps growing. However, back in the time when we first chose this molecule CaH, there were some conservations about whether it will work in the end, and whether it would be another BaH molecule. We thus started from cheaper home-built options.

Luckily, we were able to find a single-mode laser diode, USHIO HL69001DG, that could deliver ~200 mW for our wavelengths. With temperature tuning, this diode can work for both the $A \leftarrow X$ cycling transitions and $B^2\Sigma^+(v' = 0,\ N' = 0,\ +) \leftarrow X^2\Sigma^+(v = 1,\ N = 1,\ -)$ repump transition, which is enough for proof-of-principle beam experiments.

We adopted the homemade laser designs from David DeMille's group now at Johns Hopkins University [104] and modified it according to our needs. Their ECDL design employs the Littrow-

Hänsch (or Littrow in short) configuration due to its higher power output compared to the Littman-Metcalf configuration. The laser frequencies are measured on a HighFinesse WS7-60 wavemeter with a precision down to 1 MHz. Because of the broad MHz-level transitions in molecules, locking these lasers to this wavemeter is good enough for any applications mentioned in this thesis.

However, since we are relying solely on the wavemeter, any potential uncontrolled drifts should be taken care of. The most dramatic source of instability comes from the instability of the room temperature and pressure. The solution to this problem is to seal the wavemeter in a vacuum chamber to isolate it from the environment. All of the electronics are connected with vacuum feedthroughs, and for the optical connection, we drill a hole on a vacuum blank, send in a bare fiber, and glue it with a vacuum-compatible glue. No vacuum pumping is needed. Once we do this, the wavemeter's stability improves from ~50 MHz drift per day to ~10 MHz drift per month. This small drift can be easily captured with a stable reference laser. In our case, we use the other projects Sr red MOT laser addressing the $5s5p\ ^3P_1 \leftarrow 5s^2\ ^1S_0$ transition as a reference.

4.1.2 Beamline

We inherited the beamline from the BaH laser cooling experiment, where there is a long interaction region (~12 cm), details can be found in Ref. [65, 129]. Figure 4.1 shows a schematic of the experiment. We start with a CBGB source as described in the previous chapter. Back then we have not upgraded the cell so the schematic shows an older cell design. We use the fundamental output of a pulsed Nd:YAG laser operating at 1064 nm to ablate on the CaH_2 target, and we run the ablation at a maximum pulse energy of 30 mJ (Big Sky Ultra CFR UL620111). He buffer gas is flowed into the cell at a rate of ~6 SCCM via a capillary on the back of the cell. After leaving the cryostat, the molecules enter the beamline. The high vacuum chamber is equipped with a beam aperture of 5 mm diameter to filter out the $1/e^2$ transverse velocity range to $\sim \pm 3$ m/s [Fig. 4.1(a)]. We keep the aperture in place for all data shown in this work. Subsequently, the molecules enter an interaction region with rectangular, antireflection coated windows enabling a 12 cm long interaction length. Next, the molecules enter a "cleanup" region, where population accumulated in the

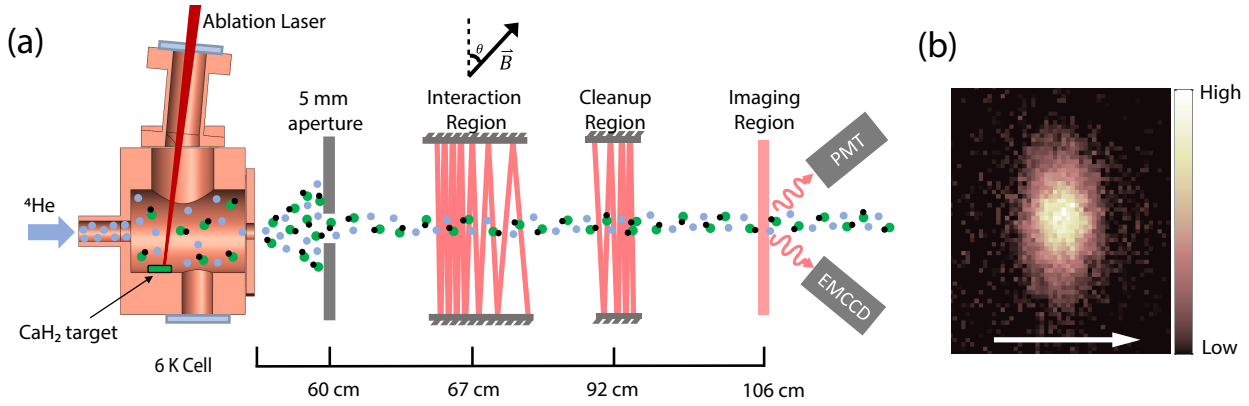

Figure 4.1: (a) Schematic for the 1D cooling experiment. CaH molecules are produced via ablation of a solid target of CaH_2. The ejected molecules thermalize to the $\sim$ 6 K He buffer gas and are extracted through a 3 mm diameter aperture. An additional 5 mm aperture is placed just before the molecular beam enters the interaction region to limit the transverse velocity distribution. The cooling chamber consists of 12 cm of optical access followed by a cleanup region and a detection region. (b) A sample image of molecules in the beam taken with the EMCCD camera. Photons are collected for 7 ms during imaging. Arrow indicates the direction of the molecular beam.

$X(v'' = 1)$ state is pumped back to the $X(v'' = 0)$ state via the $B(v' = 0)$ state, and are then detected in the imaging region by scattering photons on the $B(v' = 0) \leftarrow X(v'' = 0)$ transition. The scattered photons are simultaneously collected on a PMT and an EMCCD camera. An example of the average camera images collected is shown in Fig. 4.1(b).

4.2 FCF and VBR Measurements

We perform the VBR measurement with our molecular beam using a process similar to the one described in Ref. [130]. A pump laser beam intersects the CaH beam orthogonally in the imaging region, and resonantly excites the molecules from $X^2\Sigma^+(v'' = 0)$ ground states to the $A^2\Pi_{1/2}(v' = 0)$ or $B^2\Sigma^+(v' = 0)$ excited states. Once excited, two PMTs in photon-counting mode with different dichroic filters are used to collect the photons simultaneously emitted from the various decay pathways of the excited state. The narrow bandpass dichroic filters are strategically chosen to isolate photons with a frequency resonant with vibrational decay to a single excited vibrational state ($\lambda_{0v''}$) while simultaneously detecting the molecules that return to the ground state (λ_{00}).

We first compare the time traces of two PMTs when their filters allow transmission at the same λ_{00} frequency. The ratio of integrated signals, R_0, can be expressed with systematic parameters and VBRs as

$$R_0 = \frac{N\mathrm{VBR}_{00}\Omega_{P_2}T_{F_2,\lambda_{00}}Q_{P_2,\lambda_{00}}}{N\mathrm{VBR}_{00}\Omega_{P_1}T_{F_1,\lambda_{00}}Q_{P_1,\lambda_{00}}}, \tag{4.1}$$

where the subscripts P_1/P_2 stand for two PMTs used in this experiment (Hamamatsu R13456 and SensTech P30PC-01), subscripts F_1/F_2 stand for the two bandpass filters used, N is the number of scattering events, Ω_P is the geometrical collection efficiency for a given PMT, $T_{F,\lambda}$ is the transmission efficiency for a given bandpass filter at a wavelength λ, and $Q_{P,\lambda}$ is the quantum efficiency for a given PMT at a wavelength λ.

Next, we replace filter F_2 with another filter F_3 which blocks transmission at λ_{00} and allows transmission at $\lambda_{0\nu''}$, where ν'' is 1 or 2. The ratio of integrated signals, $R_{\nu''}$, can then be written as

$$R_{\nu''} = \frac{N'\mathrm{VBR}_{0\nu''}\Omega_{P_2}T_{F_3,\lambda_{0\nu''}}Q_{P_2,\lambda_{0\nu''}}}{N'\mathrm{VBR}_{00}\Omega_{P_1}T_{F_1,\lambda_{00}}Q_{P_1,\lambda_{00}}}. \tag{4.2}$$

An example of the measured signals is shown in Fig. 4.2(a). For each measurement we simultaneously collect the time traces from the two PMTs. In order to obtain the ratio $R_{\nu''}$, we perform a one-parameter least square fit of all points in one time trace to the other [Fig. 4.2(a) inset]. Since the PMTs are stationary throughout the experiment, any variation in Ω is negligible. By measuring the transmission efficiency of the filters F_2/F_3 at $\lambda_{00}/\lambda_{0\nu''}$, as well as the quantum efficiency of P_2 at $\lambda_{00}/\lambda_{0\nu''}$, and combining Eq. (4.1) and Eq. (4.2), we estimate the ratio of VBRs as

$$\frac{\mathrm{VBR}_{0\nu''}}{\mathrm{VBR}_{00}} = \frac{R_{\nu''}Q_{P_2,\lambda_{00}}T_{F_2,\lambda_{00}}}{R_0Q_{P_2,\lambda_{0\nu''}}T_{F_3,\lambda_{0\nu''}}}. \tag{4.3}$$

We calculate the individual VBRs by assuming that the sum is $\sum_{\nu''=0}^{2}\mathrm{VBR}_{0\nu''} = 1$. This is a reasonable approximation since the calculated value of q_{03} is smaller than the statistical uncertainty in the measured FCFs for both A and B states (Table 2.2). The resulting VBRs are plotted in Fig. 4.2(b) and Fig. 4.2(c). The measured FCFs were calculated using the inverted form of

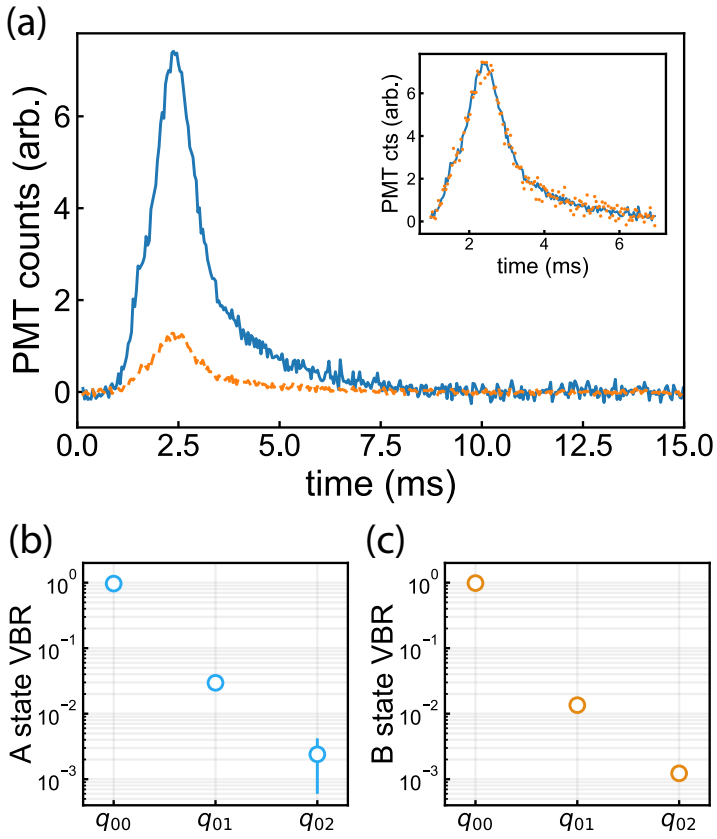

Figure 4.2: Measurement of the VBRs for CaH molecules. (a) An example of PMT traces used to calculate the VBRs. These two time traces correspond to background-subtracted fluorescence from the decay to $X(v'' = 0)$ for PMTs P_1 (orange, dashed) and P_2 (blue, solid) while the $B^2\Sigma^+(v' = 0) \leftarrow X^2\Sigma^+(v'' = 0)$ transition is excited. The cell was performing suboptimally during this data taking, the molecular beam velocity is faster at ~400 m/s, leading to an earlier arrival time. The inset denotes how the ratio of integrated signals, R_0, is computed. We perform a one-parameter fit of the dashed trace to the solid trace. The result of the fit produces the orange points that can be seen to overlap temporally with the blue trace. (b)–(c) The resulting VBRs from the measured ratio $R_{v''}$, obtained by evaluating Eq. (4.3), for the A and B states. Each point represents an average of at least 200 shots with background subtraction, while the higher vibrational decays require ~700 shots for an appreciable SNR due to the low probability of decaying to these excited states. Error bars are statistical standard errors.

Eq. (2.8).

4.3 Scattering Rate Measurement

Efficient cooling and slowing of molecules require rapid scattering of photons while simultaneously minimizing the loss to unaddressed vibrationally excited states. From the measured VBRs

for the primary decay pathways for CaH, we obtain the average number of photons per molecule, $\langle N_{\rm ph}\rangle$, that we expect to scatter while addressing N_v vibrational channels before only $1/e$ of the ground state population remains available for optical cycling as

$$\langle N_{\rm ph}\rangle \simeq \frac{1}{1-\sum_{v''=0}^{N_v} \mathrm{VBR}_{0v''}}. \tag{4.4}$$

Thus we expect to scatter 31(3) photons for $A \leftarrow X(v''=0)$ and 68(5) photons for $B \leftarrow X(v''=0)$ before losing 63% of molecules to the $X(v''=1)$ state. Next, if the $X(v''=1)$ state is repumped, this photon number increases to around 400 for the A state and 800 for the B state cycling schemes. In order to slow a CaH molecule traveling at 250 m/s to within the capture velocity of a MOT ($\lesssim$10 m/s), we would need to scatter $\sim 2\times10^4$ photons. Although the loss to excited vibrational modes can be minimized by using repumping lasers for higher vibrational states, it is essential to scatter photons at a high rate so that the slowing distance can be minimized. The maximum scattering rate for a multilevel system with n_g ground states and n_e excited states is given by Ref. [131]:

$$R_{\rm sc,max} = \Gamma_{\rm eff} = \frac{1}{\tau}\frac{n_e}{n_e+n_g} \tag{4.5}$$

where τ is the excited state lifetime given in Table 2.2. The rotationally closed transition employed here is $N'=0 \leftarrow N''=1$, i.e., $n_e=4$ and $n_g=12$. Here we assume that the repumping lasers couple to different excited states. We obtain the maximum scattering rate $\sim 7.6\times10^6$ s^{-1} for the A state and $\sim 4.3\times10^6$ s^{-1} for the B state. In practice, however, it is difficult to achieve these maximum values and most experiments with diatomic, triatomic, and polyatomic molecules to date achieve scattering rates up to $\sim 2\times10^6$ s^{-1}.

In order to determine the maximum scattering rate achievable in our setup, we measure the fraction of molecules that are pumped to dark vibrationally excited states as a function of interaction time. First, we apply only the $A \leftarrow X(v''=0)$ linearly polarized, resonant light (~80 mW per spin-rotation component) in the interaction region in a multi-pass configuration [Fig. 4.1(a)]. Each pass of the laser beam is spatially resolved so that the effective interaction length can be varied and

quantified by counting the number of passes. We detect the population remaining in $X(v'' = 0)$, and we convert the interaction length to time by measuring the laser beam waist ($1/e^2$ radius of 0.55 mm in the direction parallel to the molecular beam and 0.84 mm in the orthogonal direction) and estimating the average velocity weighted by the relative population within the velocity distribution (251 m/s). We also apply a 3 G magnetic field in the interaction region to destabilize the dark magnetic sublevels that become populated during optical cycling. Magnetic field strength and laser polarization angle with respect to the magnetic field are scanned to maximize the scattering rate.

As the molecules propagate through the interaction region and scatter photons, some of the excited state molecules decay to unaddressed higher vibrational states at a rate given by the sum of addressed state VBRs as

$$f_{\mathrm{rem}}(t) = \frac{N_{\mathrm{mol}}(t)}{N_{\mathrm{mol}}(t=0)} = \left(\sum_{v''=0}^{v_a} \mathrm{VBR}_{0v''} \right)^{N_p(t)} \tag{4.6}$$

where f_{rem} is the fraction of molecules that remain in all the addressed states combined. The number of scattered photons is $N_p(t) = R_{\mathrm{sc}} t$, and v_a is the highest addressed vibrational level. The experimental data is shown in Fig. 4.3 (orange circles). We fit the decay in f_{rem} to an exponential decay with a finite offset. We note that in the limit of infinite interaction time, $f_{\mathrm{rem}} \to 0$. However, in our setup we have a small fraction of the molecules that only weakly interact with the laser beam but are still detected in the imaging region. These molecules are accounted for by adding a constant offset to f_{rem}. From the exponential decay constant τ_d, we can obtain the scattering rate

$$R_{\mathrm{sc}} \simeq \frac{1}{\tau_d \left(1 - \sum_{v''=0}^{v_a} \mathrm{VBR}_{0v''}\right)}. \tag{4.7}$$

Using our measured values of the VBRs and τ_d from the orange curve of Fig. 4.3, we estimate an average scattering rate of $1.67(15) \times 10^6$ s^{-1}. Here we make a simplifying assumption that the local variation in light intensity does not affect our estimate. We justify this assumption by noting

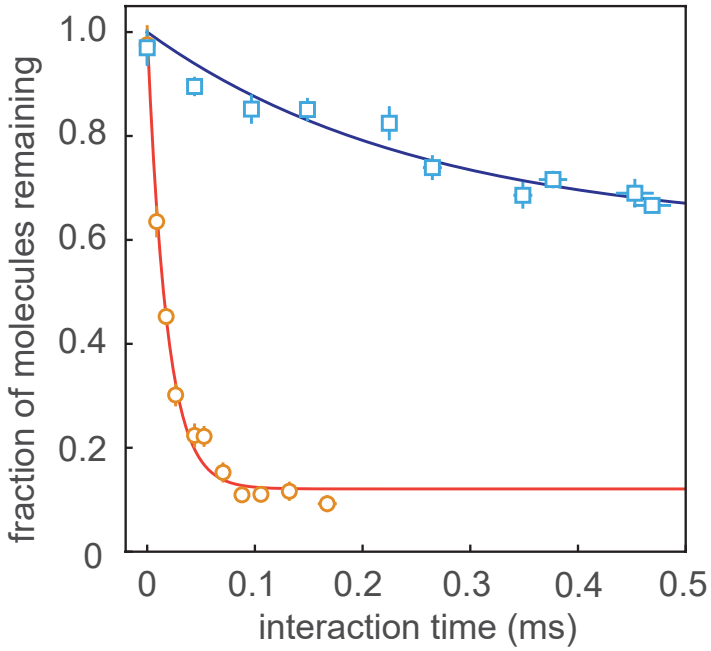

Figure 4.3: Scattering rate measurement. The fraction of molecules remaining in the $X(v'' = 0)$ state when cycling on the $A(v' = 0) \leftarrow X(v'' = 0)$ transition (orange circles) and the fraction remaining in $X(v'' = 0) + X(v'' = 1)$ states when cycling simultaneously on the $A(v' = 0) \leftarrow X(v'' = 0)$ and the $B(v' = 0) \leftarrow X(v'' = 1)$ transitions (blue squares) are measured as a function of the interaction time. Lines are fits to exponential decay curves with finite offsets. The offset is due to detected molecules that are only weakly addressed in the interaction region. The exponential decay time constant τ from the fit is $5.5(3) \times 10^4\ s^{-1}$ for the orange curve and $3.92(13) \times 10^3\ s^{-1}$ for the blue curve.

that the laser intensity far exceeds the predicted saturation intensity ($I_{\text{sat}} \approx 1.9\ \text{mW/cm}^2$) after accounting for the Gaussian laser beam profile, beam propagation, and power loss per pass.

Next, we measure R_{sc} after adding ~110 mW of repumping light addressing the $B(v' = 0) \leftarrow X(v'' = 1)$ transition, co-propagating with the main cooling light. In this case, we also add ~40 mW of the same repumping light to the cleanup region. Within this multi-pass cleanup region, we are able to transfer the $X(v'' = 1)$ population to $X(v'' = 0)$ with >90% efficiency. The resulting data is plotted in Fig. 4.3 (blue squares). In this case the decay time is much longer, since it takes 33 photons for a $1/e$ decay in ground state population when only the $A(v' = 0) \leftarrow X(v'' = 0)$ is addressed, while it takes ~400 photons when the repump is added. However, the precision of this experiment is limited by the measured VBR values. From the decay constant of the exponential fit, we obtain an average scattering rate $1.6(1.2) \times 10^6\ \text{s}^{-1}$. The uncertainty mostly comes from

VBR_{02}. Nevertheless, the two independent measurements provide an order-of-magnitude estimate of the scattering rate. The relatively high values of R_{sc} indicate that we can achieve sufficiently high scattering rates for CaH molecules. Finally, at the longest interaction time, we estimate that 170^{+500}_{-70} photons per molecule are scattered.

4.4 Magnetically Assisted Sisyphus Cooling

The technique of Sisyphus cooling was first demonstrated with atoms [132, 133]. It was subsequently demonstrated with diatomic [61, 64], triatomic [70], and symmetric top [73] molecules. Alternative methods such as optoelectric Sisyphus cooling [134] and Zeeman-Sisyphus deceleration [56, 57] of polyatomic molecules have also been demonstrated. Briefly, in a Type-II cycling scheme with more ground than excited sublevels, dark states exist. Molecules traveling at a velocity v through a standing wave formed by counter-propagating, near-resonant laser beams lose kinetic energy as they travel up potential hills that arise from spatially varying AC Stark shifts. At the top of the hill where the intensity is highest, molecules absorb the near-resonant photons and rapidly decay to a dark state, finding themselves at the bottom of the hill. If the magnetic field induced remixing rate is matched to the propagation time along the standing wave, $\lambda/(4v)$, the molecules return to the bright state and can climb up the potential hill again. This process repeats multiple times, leading to cooling. The opposite effect of Sisyphus heating can be generated by using a red-detuned laser.

We perform Sisyphus cooling and heating by allowing the laser beam in a multi-pass configuration to overlap between adjacent passes. In order to achieve higher intensities, we keep the laser beam waist relatively small. This leads to substantial beam expansion as the beam propagates. We rely on this expansion after ~16 passes to create sufficient overlap for a standing wave. We estimate a peak intensity of ~200 mW/cm^2 for one beam within a 5 cm long interaction region. We apply a magnetic field $\vec{B}$ perpendicular to both the molecular beam and the laser wave vector $\vec{k}$, and tune the linear laser polarization to maximize R_{sc}. When optimized, we observe Sisyphus cooling at a detuning of +20 MHz as a visible compression of the width of the molecular distribution and also

a slight enhancement in the on-axis molecule number [Fig. 4.4(a)]. When the detuning is switched to −20 MHz, we instead see an increase in the molecular width and the emergence of bimodality near the center, a tell-tale sign of Sisyphus heating. We fit each trace to a 1D Gaussian function to obtain the $1/e$ cloud radius σ.

We perform optical Bloch equation (OBE) simulations of the internal states of the molecule in order to estimate the Sisyphus force. Details of the simulation can be found in Refs. [135, 136] and also in Qi Sun's thesis [137]. Briefly, we account for 12 ground states and 4 excited states. We let these molecular states evolve under the OBEs. The force is calculated once the excited state population has reached steady state. Next, we perform Monte Carlo (MC) simulations of individual trajectories as the molecules travel through the interaction region and arrive in the detection region. The spatial distribution from the MC simulation can be compared to the measured camera images. In addition, the associated velocity distribution gives us access to the beam transverse temperature. Furthermore, we consider the full possible range of the standing wave intensity which determines the magnitude of the Sisyphus effect, and use this range to estimate the simulation uncertainty.

We characterize the Sisyphus effect in our experiment as a function of three parameters: detuning δ, intensity I, and magnetic field strength B [Figs. 4.4(b)–4.4(d)]. To quantify the cooling effect, we plot the change in cloud radius, $\Delta\sigma$, measured in mm. To minimize systematic effects, we take one molecule image with the Sisyphus laser beams on in one ablation pulse, followed by one molecule image with them off in the subsequent ablation pulse. This allows us to account for drifts in the ablation yield and beam velocity. We repeat this process for 200 shots to obtain the SNR depicted in Fig. 4.4. We observe the expected Sisyphus behavior with detuning that is opposite of the Doppler effect: red-detuned heating and blue-detuned cooling. We additionally observe that the Sisyphus effect persists for detunings up to ±50 MHz [Fig. 4.4(b)]. We next measure the dependence on the laser intensity by varying the laser power while keeping the detuning fixed at $\delta = +20$ MHz. We note that we do not reach saturation of Sisyphus cooling at our maximum available laser intensity, although we expect to be in the saturated regime for photon scattering. This is due to the fact that the depth of the potential hill that quantifies the energy loss per cycle during

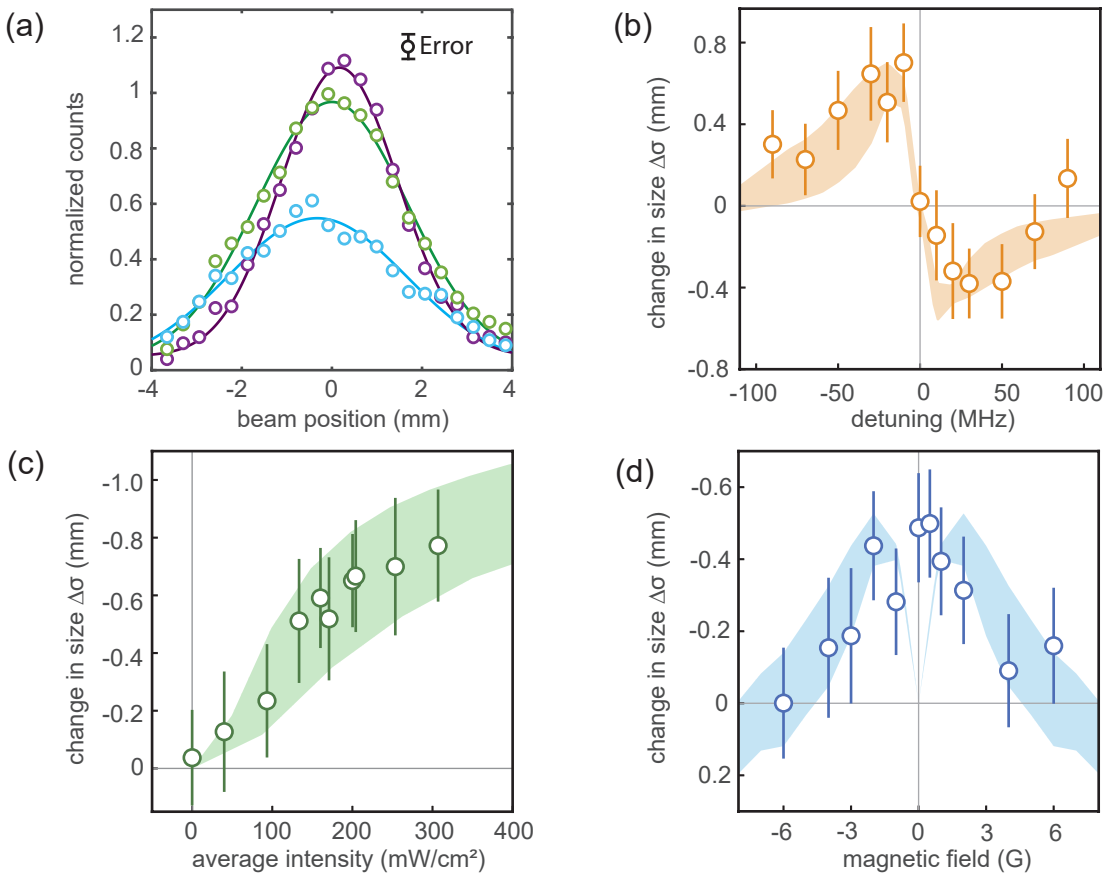

Figure 4.4: Magnetically assisted Sisyphus effect in CaH. (a) Molecular beam profiles obtained for an unperturbed beam (green), Sisyphus cooled beam (purple) at $\delta = +20$ MHz, and Sisyphus heated beam (blue) at $\delta = -20$ MHz. The y-axis is normalized to the unperturbed beam maximum and no other scale factors are used. Lines are fits to a 1D Gaussian function to obtain the $1/e$ cloud radius σ. The increase in on-axis molecule number seen in the cooling configuration is a clear signature of Sisyphus cooling. Statistical error for each point is represented by the bar on top right and is depicted separately for clarity. (b) Change in σ as a function of detuning, where $\Delta\sigma > 0$ implies heating and vice versa. The detuning is applied globally to each spin-rotation and hyperfine addressing lasers. The data was taken at an intensity of 200 mW/cm^2. The band represents the result of OBE and MC simulations for our experimental system. (c) Change in beam size $\Delta\sigma$ as a function of laser intensity. Detuning has been fixed at $\delta = +20$ MHz. We do not saturate the Sisyphus cooling effect even at the largest available laser intensity (~300 mW/cm^2). The simulations shown as a band suggest that an intensity of >600 mW/cm^2 is required for saturation. (d) Change in beam size $\Delta\sigma$ as a function of magnetic field strength. Detuning is $\delta = +20$ MHz and intensity is 200 mW/cm^2. Maximum cooling is seen for $B \approx 1$ G. Note that the scattering rate is maximized at $B \approx 3$ G. The Sisyphus effect is expected to be nulled at $B = 0$, but due to the presence of the Earth's magnetic field and the low laser intensity we do not resolve the dip. The simulation shows the same behavior. The bands shown in simulations encompass the spatial variation in laser intensity we expect in the experiment. Each point is a result of 200 repetitions of the experiment, and the experimental error bars are standard errors of Gaussian fitting.

Sisyphus cooling has a stronger dependence on the degree of overlap between adjacent beams than on the peak laser intensity. From the simulations, we predict that saturation can be expected for intensities above 600 mW/cm^2 [Fig. 4.4(c)]. At the intensity where we see the largest cooling effect, we estimate that the transverse temperature of the molecular beam is reduced from 12.2(1.2) mK to 5.7(1.1) mK while scattering 140^{+400}_{-60} photons. Lastly, we measure the dependence on magnetic field strength at a fixed detuning ($\delta = +20$ MHz) and intensity (200 mW/cm^2). The magnetically assisted Sisyphus effect should operate at non-zero magnetic fields, and at our low laser intensities the peak is expected at ∼1 G as corroborated by simulations [Fig. 4.4(d)]. Since the Earth's field is not canceled in the experiment, we do not detect a clear dip around $B = 0$. Nevertheless, we can be certain that Sisyphus cooling is observed here, since maximum photon scattering occurs at $B \sim 3$ G.

Chapter 5: Predissociative Loss of CaH

With highly diagonal FCFs, high photon scattering rate at the 10^6 s^{-1} level, and a decent 1D laser cooling performance, CaH should be a viable candidate for further cooling and trapping. However, during the above measurements, we realize that if cycling photons on the $B^2\Sigma^+(v' = 0,\ N' = 0,\ +) \leftarrow X^2\Sigma^+(v = 0,\ N = 1,\ -)$ transition, there is additional loss that could not be explained by vibrational branching. Later on we figure this is coming from a process called predissociation.

In CaH, the lowest-energy excited state $A^2\Pi_{1/2}$ ($v' = 0$) lies 556 cm^{-1} above the Ca(^1S)+H(^2S) dissociation threshold of the ground $X^2\Sigma^+$ manifold [Fig. 5.1(a)], so a molecule in the excited state could decay into the continuum via a radiationless transition. This phenomenon, known as predissociation [138, 139], is traditionally studied by observing spectral line shapes and widths inconsistent with radiative decay. A predissociated molecule cannot be repumped into optical cycling because of the significant physical separation and relative velocity of the fragments. Hence the predissociation probability (P_{pd}) sets a limit on the number of photons one can scatter with laser cooling.

Despite the fact that the $A^2\Pi$ state in CaH lies above the ground state threshold energy, predissociation from $A^2\Pi$ to the $X^2\Sigma^+$ continuum is nominally forbidden due to the von Neumann-Wigner noncrossing rule [140]. For diatomic molecules, states with different symmetries cross while those with the same symmetries form avoided crossings [141, 142] (i.e., the molecular Hamiltonian does not couple states with different symmetries). The second-lowest excited $B^2\Sigma^+$ state is allowed to predissociate. However, effects such as spin-orbit coupling can lead to mixing of $A^2\Pi$ and $B^2\Sigma^+$ states resulting in a small but finite P_{pd} for $A^2\Pi$. Both A and B states are important for efficient optical cycling.

Here we present theoretical analysis, collaborating with Prof. Anastassia N. Alexandrova at

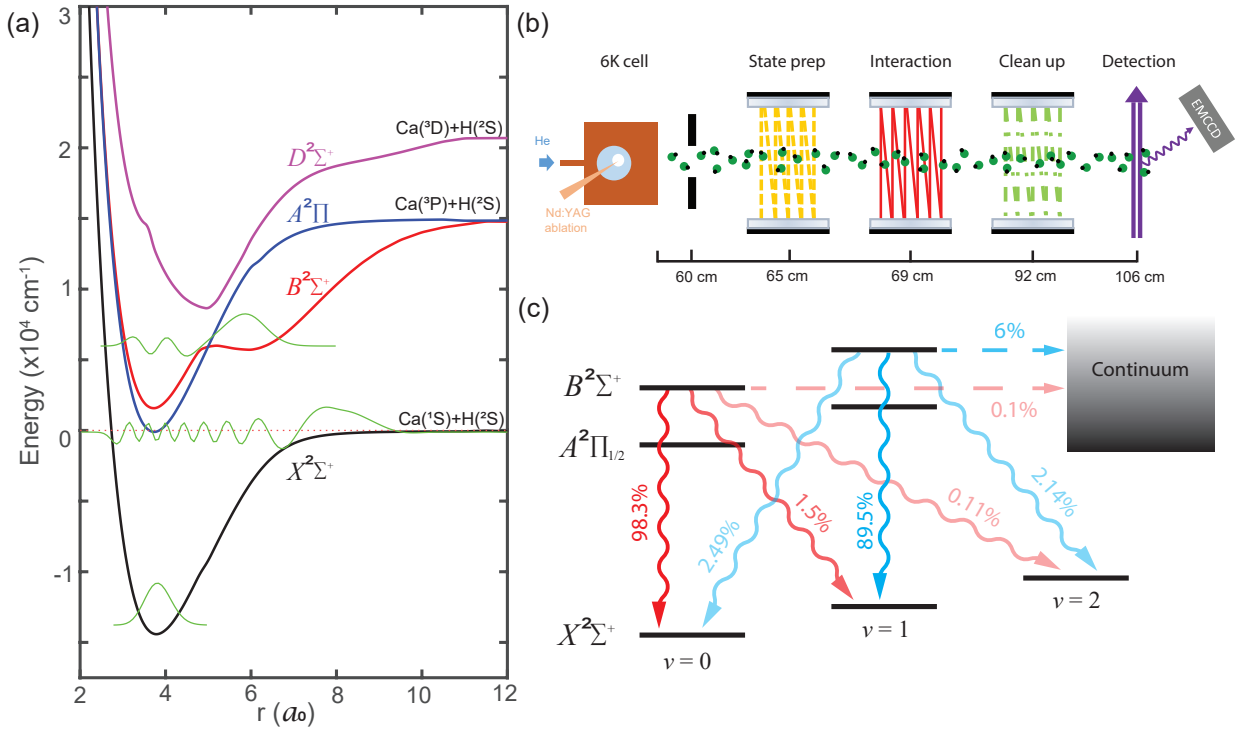

Figure 5.1: (a) PES for the 4 lowest electronic states of CaH: $X^2\Sigma^+$, $A^2\Pi$, $B^2\Sigma^+$, and $D^2\Sigma^+$. Spin-orbit interaction is omitted. The x-axis is the internuclear separation r in Bohr radii (a_0) and the y-axis is energy in cm^{-1} (1 cm^{-1} $\approx$ 30 GHz). The energy origin is chosen as the Ca(^1S)+H(^2S) continuum threshold (v_{th}). Superimposed are the wavefunctions (bottom to top) for the $X(v'' = 0)$ absolute ground state, $X(v'' = 15)$ least-bound state, and $B(v' = 4)$ excited state. (b) Experimental layout for predissociation measurement. The CaH molecular beam encounters 4 spatially separated regions: state preparation (S), interaction (I), cleanup (C), and detection (D). Each region includes multipassed lasers described in the text. The diagram is not aligned to scale. (c) Relevant VBRs (squiggly arrows) calculated for the $B^2\Sigma^+$ state. The hyperfine structure of the excited states is unresolved. Measured predissociation probabilities for $B(v' = 0)$ and $B(v' = 1)$ are denoted by dashed lines.

UCLA, and measurements of predissociation probability for the $B^2\Sigma^+$ state of CaH. We perform *ab initio* calculations of the potential energy surfaces for CaH, and confirm their accuracy by extracting the FCFs for the primary $A^2\Pi_{1/2} \rightarrow X^2\Sigma^+$ and $B^2\Sigma^+ \rightarrow X^2\Sigma^+$ decays and comparing them to our previous measurements. We calculate a nonradiative decay rate, and obtain an estimate of P_{pd} by comparing it to the radiative decay rate. Next, we present a novel experimental protocol to measure an upper bound of P_{pd}. We find that $P_{\text{pd}} \approx 1 \times 10^{-3}$ for the vibrational ground state ($v' = 0$) and $\approx 6 \times 10^{-2}$ for the first vibrationally excited state ($v' = 1$) of the $B^2\Sigma^+$ manifold. We deduce that the vibrational ground state of the $A^2\Pi_{1/2}$ manifold predissociates with a $\sim 5 \times$

10^{-7} probability due to spin-orbit mixing with the B state. The measured values of P_{pd} imply a ~50% predissociative molecule loss after scattering 10^4 photons, suggesting that a MOT of CaH is feasible.

5.1 Theoretical Model

The theoretical approach described in the following is performed by our collaborator at UCLA and JHU, and is shown here for a complete picture. A more detailed discussion can be found in Claire E. Dickerson's thesis [143].

5.1.1 Calculation of Molecular Potential Energies

The starting point for our calculations is the construction of PES for CaH. All calculations were performed using the Molpro program [144, 145, 146]. We adopt a basis set and active space as in Ref. [147], where we use cc-pwCVQZ [148] for the Ca atom and aug-cc-pVQZ [149] for the H atom. Calculations were performed in C_{2v} symmetry, which is the nearest Abelian point group to $C_{\infty v}$. Orbitals were generated with a restricted Hartree-Fock formalism (RHF), then further optimized in a state-averaged complete active space self-consistent field (SA-CASSCF) [150] calculation involving 3 active electrons and 9 active orbitals. For the Σ^+ states, 4 states were averaged at equal weights in the SA-CASSCF calculation, with (5,2,2,0) closed and (9,4,4,1) occupied orbitals.

For the $A^2\Pi$ state, since only abelian point group symmetries are available, a two-state SA-CASSCF calculation with the same active space was performed in C_{2v} symmetry involving symmetries 2 and 3 of equal weight to represent the $C_{\infty v}$ A state. These wavefunctions were then used in a multireference configuration interaction calculation with Davidson corrections for higher excitations (MRCI+Q) [151, 152, 153]. Here, (3,1,1,0) orbitals made up the core, (5,2,2,0) were closed and (9,4,4,1) were occupied. Electron correlation involving double and single excitations were allowed. Spin-orbit interaction was incorporated at the MRCI level using the Breit-Pauli Hamiltonian [154].

5.1.2 Calculation of FCFs

Next, we employ the vibrational wavefunctions obtained in Sec. 5.1.1 to calculate the FCFs for the CaH transitions of interest. FCFs are calculated using a grid representation of the vibrational wavefunctions. A spline interpolation was fit to the potential energy surfaces calculated in Molpro to create the potential energy functions, $V(r)$. The real space kinetic energy operator was approximated with the Colbert-Miller derivative [155]. Nonadiabatic coupling vectors were computed analytically with the CP-MCSCF program [156] in Molpro and fit to a spline interpolation. They were incorporated into the Hamiltonian by directly adding the nonadiabatic coupling to the momentum operator [157]. The Hamiltonian was diagonalized to obtain eigenvalues and eigenvectors. Our calculations converged with a grid-spacing (dr) of 0.007 a_0 and a box size of 16.5 a_0.

We compare our calculated FCFs to previous experimental measurements [66] in Table 5.1. We chose the active space which matched $B^2\Sigma^+$ and $X^2\Sigma^+$ state FCFs and vibrational energies in all calculations, since MRCI spin-orbit coupling (SOC) requires the same active space for all involved states. Therefore, the FCFs for $A^2\Pi$ could be improved with varied active space, but a compromise was made to estimate SOC splittings. Despite this compromise, we find the $A^2\Pi_{1/2}$ potential has the correct shape but a slightly incorrect equilibrium bond length.

Table 5.1: The calculated FCFs for CaH, compared to experimental FCFs [66]. The experimental FCFs are derived from measured VBRs. Note that the active space was optimized for the B state.

Transition	Vibrational quanta (v'')	FCF calculated ($q_{0v''}$)	FCF measured ($q_{0v''}$)
$A \rightarrow X$	0	0.9788	0.9572(43)
	1	0.0205	0.0386(32)
	2	6.8×10^{-4}	$4.2(3.2) \times 10^{-3}$
	3	4.1×10^{-5}	-
$B \rightarrow X$	0	0.9789	0.9807(13)
	1	0.0192	0.0173(13)
	2	1.8×10^{-3}	$2.0(3) \times 10^{-3}$
	3	1.4×10^{-4}	-

5.1.3 $B^2\Sigma^+$ Predissociation Estimate

Predissociation probability estimates were computed using an optical absorbing potential with previously predicted scattering cross sections close to experiment [158, 159, 160]. An absorbing potential resembling a decaying half-parabola of the form $-iV(r-r_0)^2/w^2$ was added to the $X^2\Sigma^+$ potential energy starting and centered at $r_0 = 8\,a_0$ with a width $w = 8\,a_0$ and a depth of $V = 0.2$ a.u. (4.4×10^4 cm^{-1}). Results are insensitive to absorber placement as long as it is placed along the potential energy surface's asymptote [160] and has a width larger than the typical de Broglie wavelength [161]. This creates a channeled flux equation which imposes a boundary condition on the wavefunction and eigenvalues attain an imaginary component.

This component, such as the imaginary eigenvalue of $B(v' = 0)$, is directly related to the nonadiabatic coupling between that vibrational wavefunction and the X continuum (where we placed the absorber) as the nonradiative transition rate A_{NR}. We estimate the predissociation probability as the ratio of the calculated nonradiative (A_{NR}) and radiative (A_R) decay rates, $A_{\mathrm{NR}}/(A_{\mathrm{NR}} + A_R)$.

5.2 $B^2\Sigma^+$ Predissociation Measurement

The experimental setup is similar to that of the 1D cooling experiment. The CaH beam enters a high-vacuum chamber which is divided into four regions: state preparation, interaction, cleanup, and detection, as shown in Fig. 5.1(b). In the first three regions, the molecular beam intersects with transverse lasers that address $X \rightarrow A$ or $X \rightarrow B$ transitions. These lasers can be switched on and off by independent optical shutters. The laser beams are multipassed to increase the interaction time with the molecular beam. In the detection region, we apply a single-pass $X \rightarrow A$ or $X \rightarrow B$ light and use an EMCCD camera and a PMT to collect the LIF signals for spatially and temporally resolved detection. Every molecule scatters ~20 photons in the detection region, which implies that we are not sensitive to the initial spin-rotation and hyperfine distribution. All addressed transitions are from the $X^2\Sigma^+$ ($N'' = 1$) state to $A^2\Pi_{1/2}$ ($J' = 1/2$) or $B^2\Sigma^+$ ($N' = 0$) states in order to obtain rotational closure. We use electro-optic modulators (EOMs) to generate sidebands on all lasers to

cover all hyperfine states (HFS) as well as to address spin-rotation manifolds. The transitions used here were first measured experimentally with HFS resolution.

To concisely describe the lasers used in this study we adopt the notation $M^R_{v'-v''}$, which denotes the transitions addressed and the spatial positions of the lasers. M is A or B, representing the electronic state of the excited manifold. R is S, I, C, or D (state preparation, interaction, cleanup, or detection region). In addition, the $F_{Mv'v''}$ notation describes the VBRs from either $A^2\Pi_{1/2}$ or $B^2\Sigma^+$ states (represented by M) to $X^2\Sigma^+$ states. For example, F_{B01} is VBR from $B^2\Sigma^+$ ($v' = 0$) to $X^2\Sigma^+$ ($v'' = 1$). We use similar notation, F_{B0a} and F_{B1a}, to represent predissociation probabilities from $B^2\Sigma^+$ ($v' = 0$) and ($v' = 1$) states.

Below is a summary of the laser configuration used for this measurement. All laser beams pass through an EOM to generate the sidebands needed to address HFS.

- In the state preparation region, the A^S_{1-0} light (637 nm) is generated from two sets of ILAs to address the spin-rotation states, with 95 mW of power.

- In the interaction region, multiple lasers are applied. A^I_{0-0} (695 nm) or A^I_{1-1} (693 nm) light is derived from two ILAs that provide 60 mW in total. B^I_{0-0} (635 nm) or B^I_{1-1} (636 nm) is from two ECDLs with 52 mW in total.

- In the cleanup region, B^C_{0-1} (690 nm) is from two sets of ILAs with 90 mW of power, A^C_{1-0} (637 nm) is from two sets of ILAs with 88 mW, A^C_{1-2} (758 nm) or A^C_{0-1} (762 nm) is from SolsTiS continuous-wave (CW) Ti:Sapphire laser, with 93 mW and a 1 GHz EOM to address the spin-rotation states.

- In the detection region, B^D_{0-0} (635 nm) is from two ECDLs with 60 mW of power, A^D_{0-0} (695 nm) or A^D_{1-1} (693 nm) is from two ILAs with 96 mW of power.

The frequencies of all the transitions that we used are in Table 2.3 and Table 2.4. All frequencies are measured with lasers applied transversely to the molecular beam. HFS in the ground states is clearly resolved in all spectra, while HFS in the excited states is not resolved. Our measurements are consistent with previous work [108].

5.2.1 $B^2\Sigma^+$ ($v' = 0$) Predissociation Measurement Method

To measure the predissociation probability of the $B^2\Sigma^+$ ($v' = 0$) state, we need to scatter many photons via $B^2\Sigma^+$ ($v' = 0$) and detect population loss that cannot be explained by known effects, predominantly rovibrational losses. To characterize the loss we design several experimental stages, each stage corresponding to a unique configuration of lasers interacting with the molecular beam. We monitor the population of the $v'' = 0$ ground state in the detection region by detecting LIF signals from the B^D_{0-0} laser. For this measurement we employ 6 stages. By defining temporally stable parameters that describe the properties of our system, we can express the molecular population distribution at each stage.

For example, in the *Unperturbed* stage we detect $X(v'' = 0)$ population denoted by N. This is the calibration signal used as a reference. In the *Cleanup* stage we apply the B^C_{0-1} laser, and the resulting $X(v'' = 0)$ population is $N + n_1 N\kappa F_{B00}/\mathcal{F}_{B0}$ where n_1 is the normalized natural population of $X(v'' = 1)$, κ is the cleanup laser efficiency, and $\mathcal{F}_{B_0} \equiv F_{B0a} + \sum_{i\neq 1} F_{B0i}$ is the VBR normalization factor. This factor accounts for the discrete probability distribution of decay processes based on the VBRs and P_{pd}. By taking the ratio of the integrated signal of the $X(v'' = 0)$ population from *Cleanup* stage with signal from *Unperturbed* stage, we get the parameterized ratio $R_1 = 1 + n_1\kappa F_{B00}/\mathcal{F}_{B0}$. In addition to the *Unperturbed* and *Cleanup* stages, we have four more stages in this measurement, resulting in a total of 5 ratios and 5 parameters (including P_{pd}). The details of all the stages, such as the laser configurations and expressions for the normalized signal, are in Table 5.2 and Sec. 5.2.4. Thus we acquire 5 equations (measured ratios equal to the parameterized expressions) and 5 variables. We can solve the equations and express F_{B0a} via R_is. By precisely measuring R_i we can estimate the $B^2\Sigma^+$ ($v' = 0$) predissociation probability.

5.2.2 $B^2\Sigma^+$ ($v' = 1$) Predissociation Measurement Method

For the $B(v' = 1)$ state, predissociation is also measured within the framework of stages. We implement two different methods, each consisting of multiple laser configurations, to measure the same quantity. In method I we use 6 stages, always monitoring the $X(v'' = 0)$ population

downstream using laser A^D_{0-0}. The aim is to populate $X(v'' = 1)$ via an off-diagonal pumping laser A^S_{1-0} and perform optical cycling between $X(v'' = 1)$ and $B(v' = 1)$. We expect to see an increase of the $X(v'' = 0)$ population as a result of the cycling. We repump the molecules remaining in $X(v'' = 1)$ to $v'' = 0$. The recovered population might be less than expected due to vibrational loss. By ruling out other effects, we attribute the loss to $B(v' = 1)$ predissociation. The details of the 6 stages are in Table 5.3.

Method II differs in several ways. We monitor the $X(v'' = 1)$ population instead of $v'' = 0$, accounting for loss to both $v'' = 0$ and $v'' = 2$ with a sufficient SNR using laser B^D_{1-1}. The 10 stages in this method lead to 9 measured ratios. And the 7 required parameters imply that there are more equations than variables. To find the optimal solution of this over-constrained system, we define a least-squares objective function and use the Levenberg-Marquardt algorithm to search for the local minimum in the parameter space with reasonable initial guesses.

5.2.3 Predissociation Measurement Analysis

The yield of our CBGB source exhibits some slow drift. In order to reduce errors due to molecule number fluctuations, we inserted a reference stage before and after every other stage within a group when taking data. For example, in the $B(v' = 0)$ predissociation measurement, data was taken in the following order: *Unperturbed* → *Cleanup* → *Unperturbed* → *X–A Cycling* → *Unperturbed* ... *X–B Cycling* + *Cleanup* → *Unperturbed*. The reference stage for $B(v' = 1)$ method I is *Unperturbed*, while for method II it is *State Prep* + *Cleanup* $v0$. To calculate the ratios, we divide the signal by the average signal from the calibration shots before and after. The entire group of measurements is repeated multiple times. The averaged ratios can be found in Table 5.2, Table 5.3, and Table 5.4. The values in parentheses denote the 2σ statistical errors. A graphical representation of the analysis process and histograms of all five ratios can be found in Fig. 5.2.

With the ratios measured, we use a bootstrap method [162, 163, 164] to derive the mean values and build the confidence intervals of the predissociation probabilities depicted in Fig. 5.3. This method is particularly useful as it does not require any assumptions about the data such as inde-

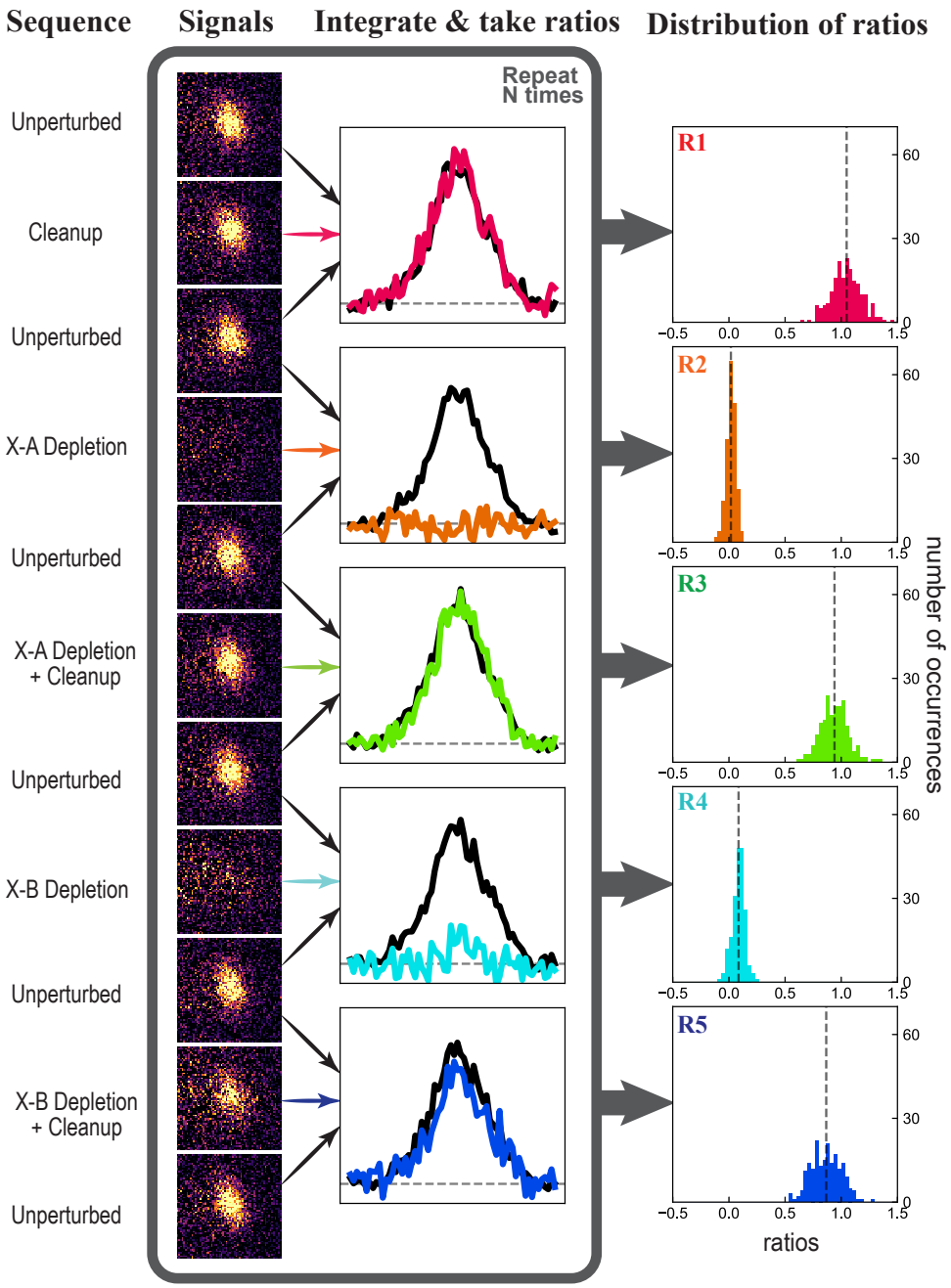

Figure 5.2: Illustration of the ratio extraction process for the $B^2\Sigma^+$ ($v' = 0$) predissociation measurement. We run the stages sequentially with an interlaced reference stage, and collect LIF with an EMCCD. We integrate the images along both axes to obtain the signals, which we then used to calculate ratios. By repeating the entire sequence N times, we collect N sets of five ratios. Here we first show examples of one-shot camera images. We then present the integrated signal along one axis, using colored traces for science stages and black for reference stages (horizontal lines are the baselines). Finally we show the histograms of the five ratios. Vertical dashed lines represent the means of the ratios.

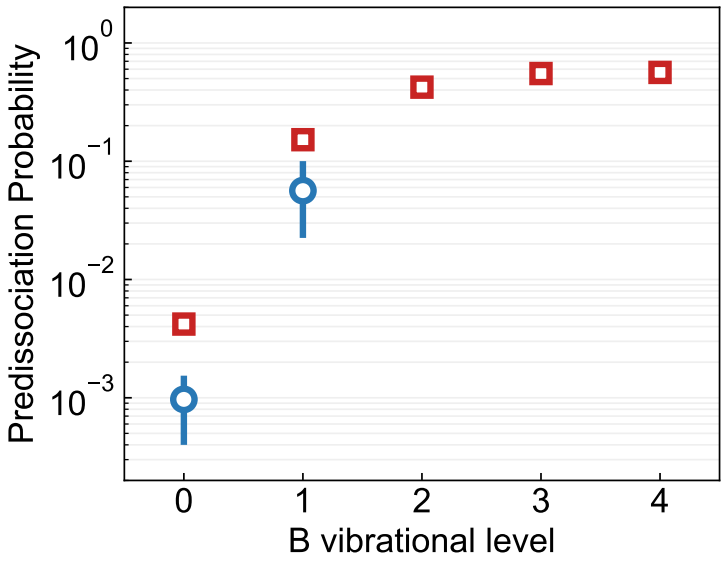

Figure 5.3: CaH predissociation. Red squares are theoretical results for nonradiative decay rates of different vibrational states of $B^2\Sigma^+$. Blue circles are experimental results, where error bars represent the 95% confidence interval.

pendence assumptions typically made for standard error calculations. We considered several other analysis methods, such as pairwise bootstrapping and regular error propagation, and the outcomes were all in agreement with each other.

After considering all systematic effects and analyzing statistical errors, we find the predissociation probability for the $B^2\Sigma^+$ ($v' = 0$) state to be $0.00097^{+0.00059}_{-0.00057}$ and for the $B^2\Sigma^+$ ($v' = 1$) state to be $0.056^{+0.044}_{-0.034}$. The reported value for $B(v' = 1)$ is the average of the two methods (method I yields $0.079^{+0.021}_{-0.017}$ and method II yields $0.033^{+0.013}_{-0.011}$), and the 95% confidence interval is the largest of the two methods combined. These values are consistent with the probabilities calculated in Sec. 5.1.3 within the order of magnitude. In addition, to demonstrate the robustness of our measurements to small variations in FCFs, we perform a comparative analysis by utilizing the FCFs obtained in previous theoretical work on CaH [109, 110]. The results consistently produce nonzero predissociation probabilities and are within error bars of each other. The sharp monotonic increase in P_{pd} seen in Fig. 5.3 can be understood as a bound molecule quantum tunneling through the $B^2\Sigma^+$ potential into the $X^2\Sigma^+$ continuum at the same energy. As the energy of the incident quantum state increases, so does the transmission probability, which is aided by stronger wavefunction overlaps.

5.2.4 Details of the Measurement Stages

The general principle for designing measurement stages is to have at least as many independent equations as parameters, which includes the B state predissociation probability. If the number of equations and parameters are equal, as in the cases of $B(v' = 0)$ and $B(v' = 1)$ using method I, we can directly express P_{pd} using the measured ratios. Other parameters will also be determined and analyzed, to serve as consistency checks. Here we present a detailed explanation of how the stages are used for predissociation probability measurements. We first discuss the simplest $B^2\Sigma^+$ ($v' = 0$) measurement, where the stages include:

- *Unperturbed*. Only the $X(v'' = 0) \rightarrow B(v' = 0)$ detection lasers are turned on. This stage serves as molecule number calibration. By taking ratios of other stages to this stage, we can eliminate molecule number N from the expressions.

- *Cleanup*. B^C_{0-1} vibrational repumpers are turned on. This stage helps to estimate the $X(v'' = 1)$ natural population.

- *X–A Cycling*. A^I_{0-0} cycling lasers are turned on. This stage can be used to estimate the vibrational population distribution after X–A cycling, and measure the depletion efficiency.

- *X–A Cycling + Cleanup*. A^I_{0-0} cycling lasers and B^C_{0-1} repumps are turned on. This stage helps to measure the repump efficiency, given the $X(v'' = 1)$ natural population.

- *X–B Cycling*. B^I_{0-0} cycling lasers are turned on. This stage helps to measure the vibrational population distribution after X–B cycling.

- *X–B Cycling + Cleanup*. B^I_{0-0} cycling lasers and B^C_{0-1} repumpers are turned on. Combined with previous stages, this helps to measure the $B^2\Sigma^+$ state predissociation probability.

To understand the stages better, let's take an example when N ground-state molecules interact with the $X(v'' = 0) \rightarrow A(v' = 0)$ laser. After optical cycling, the downstream ground-state population decreases to $d_A N$ (where $d_A < 1$ and is measurable simply by taking the ratios of

signals). In this process, we describe the depletion efficiency as $1 - d_A$. We can also describe how d_A is distributed among the different vibrational levels of $X^2\Sigma^+$ using the known VBRs. For example, the population in $X(v'' = 1)$ is $N(1 - d_A)F_{A01}/\mathcal{F}_{A0} + n_1 N$, where F_{A01}, $\mathcal{F}_{A0}$ and n_1 represent the VBR for $A(v' = 0) \rightarrow X(v'' = 1)$, the sum of VBRs for $A(v' = 0) \rightarrow X(v'' = 1, 2, 3, ...)$, and normalized $X(v'' = 1)$ natural population, because when a molecule is excited to $B(v' = 0)$ it eventually decays to a vibrational level or breaks apart. This process follows a discrete probability distribution based on the VBRs and P_{pd}. In the case discussed above, $(1 - d_A)N$ molecules leave $B(v' = 0)$, and, based on the law of large numbers, we expect the $X(v'' = 1)$ population to become $N(1 - d_A)F_{A01}/\mathcal{F}_{A0}$.

Note that our description relies on population transfer $(1 - d_A)$ rather than the number of scattered photons. In addition, the measurement protocol does not rely on the lasers having good overlap with the molecular beam or with each other, because as long as molecules share the same spatial and velocity distributions shot to shot, the parameters (e.g., cleanup efficiency) remain constant.

Here we briefly introduce the stages in method I of the $B^2\Sigma^+$ $(v' = 1)$ P_{pd} measurement:

- *Unperturbed*. We always monitor the $X(v'' = 0)$ population, which serves as calibration.
- *Cleanup*. With A^C_{0-1} laser, we pump the natural population in $X(v'' = 1)$ to $X(v'' = 0)$ to check cleanup efficiency.
- *State Prep*. With A^S_{1-0} laser, we pump the natural population in $X(v'' = 0)$ to $X(v'' = 1)$ to check state preparation efficiency. Only after efficiently pumping molecules to $X(v'' = 1)$ can we perform high-SNR optical cycling on $X(v'' = 1) \rightarrow B(v' = 1)$. Otherwise, the predissociation loss is too low to measure.
- *State Prep + Cleanup*. We first populate $X(v'' = 1)$ with A^S_{1-0} laser, then move the $X(v'' = 1)$ population back to $X(v'' = 0)$. The signal size should be comparable to the unperturbed case. This step helps to measure κ, a and n_1, which are cleanup efficiency, state preparation efficiency and $X(v'' = 1)$ natural population.

- *State Prep + X–B* 1–1 *Cycling*. With most molecules in the $X(v'' = 1)$ state, we can perform optical cycling via $B(v' = 1)$. We expect a signal increment compared to *State Prep* due to optical cycling and a redistribution of population based on VBR and P_{pd}.

- *State Prep + X–B* 1–1 *Cycling + Cleanup*. By cleaning up the population in $X(v'' = 1)$, we measure the molecules left in $X(v'' = 1)$ after optical cycling. Combined with previous stages, this provides 5 equations and 5 variables including P_{pd}.

Method II is designed as follows. We first perform state preparation to populate the $X(v'' = 1)$ state, similar to method I. By individually repumping the population that leaks to $X(v'' = 0)$ and $X(v'' = 2)$ we get a measure of unwanted loss. This also serves as a comparison of $A^2\Pi_{1/2}$ and $B^2\Sigma^+$ states in terms of the loss distribution. The 10 stages are detailed in Table 5.4. The fact that method II accounts for losses to both $X(v'' = 0)$ and $X(v'' = 2)$ has advantages and disadvantages On the one hand, method II provides an additional confidence check, with more equations than variables. On the other hand, the method relies on detection using the $X(v'' = 1)$ state, which leads to lower signals and higher drift sensitivity than detecting on $X(v'' = 0)$. Hence the SNR for method II is not significantly higher than for method I.

Measuring the predissociation probability for $B^2\Sigma^+$ ($v' = 2$) and higher vibrational levels would require pumping the population to $X^2\Sigma^+$ ($v'' = 2$) and higher and performing optical cycling there, with repumping to recover the population, and monitoring unexplained loss. However, due to practical limitations in available space and number of lasers, as well as the increased complexity of the required stages, we did not pursue these measurements.

5.3 $A^2\Pi_{1/2}$ Predissociation Estimate

The $A^2\Pi$ state in CaH does not undergo predissociation via the process described for the $B^2\Sigma^+$ state. However, SOC can induce mixing between the A and B states, leading to non-vanishing predissociation of the $A^2\Pi_{1/2}$ spin-orbit state. For a linear molecule, the z-component of total angular momentum, J_z, is a good quantum number. Therefore the spin-orbit component $A^2\Pi_{1/2}$

can interact with $B^2\Sigma^+(J_z = 1/2)$ due to the same J_z value. A similar interaction exists between $A^2\Pi_{1/2}$ and $X^2\Sigma^+(J_z = 1/2)$ but the energy separation is much larger (~14,000 cm^{-1}) compared to that between the A and B states (~1,400 cm^{-1}). Higher vibrational states of the X manifold are closer in energy to A but the effective coupling to the states relevant for laser cooling is weaker due to a poor vibrational wavefunction overlap.

We estimate the mixing between the $A(v' = 0)$ and the $B(v' = 0)$ states separated by 1400 cm^{-1}. The spin-orbit parameters were obtained with the Breit-Pauli Hamiltonian at the MRCI level [154] and are given in Table 5.5. Diagonalization of this Hamiltonian matrix leads to a 0.05% $B(v' = 0)$ admixture into the $A(v' = 0)$ state. Similarly, we can compute the mixing between $A(v' = 1)$, $B(v' = 0)$, and $B(v' = 1)$. The coupling between $A(v' = 1)$ and $B(v' = 1)$ is expected to be similar to the case of $v' = 0$ since the energy difference of 1310 cm^{-1} is similar to that in the case of $v' = 0$. However, the $A(v' = 1)$ and $B(v' = 0)$ states are only 64 cm^{-1} apart, hence even a small FCF can lead to significant mixing. Note that the measured FCF for the $A(v' = 0) \rightarrow X(v'' = 1)$ transition is 4% (Table 5.1) and that our calculated $A - B$ bond length difference is smaller than the $X - A$ bond length. We use $f = 5\%$ as an upper limit for the $A(v' = 1) \rightarrow B(v' = 0)$ FCF. Diagonalization of the corresponding Hamiltonian matrix in Table 5.5 yields a 8.4% $B(v' = 0)$ character for $A(v' = 1)$. Combining these admixtures with the measured P_{pd} for $B(v' = 0,\ 1)$, we estimate that the $A(v' = 0)$ state very weakly predissociates with a probability of $\sim 5 \times 10^{-7}$ and the $A(v' = 1)$ state with a higher probability of $\sim 3 \times 10^{-5}$. The FCF used here is an upper-bound value and therefore the estimated probabilities serve as upper bounds.

5.4 Does Predissociation Limit Us?

Now that we have measured and characterized the predissociation rate of the states of relevance to laser cooling, the question is , does predissociation limit us? The answer is no, not to the level that will completely disable a MOT. Let us walk through each state one by one here.

First, for the $B^2\Sigma^+(v = 0,\ N = 0,\ +)$ state, predissociation probability is measured to be $\sim 9.7 \times 10^{-4}$. If we use this state as the main cooling transition, the photon budget will be limited

to $\sim 10^3$, which is not enough for slowing a molecular beam of $\sim$200 m/s velocity close to zero. So instead, the main cooling transition needs to be on the $A^2\Pi_{1/2}(v = 0,\ J = 1/2,\ +)$ state, where, as estimated in Sec. 5.3, the predissociation probability is $\sim 5 \times 10^{-7}$ with a photon budget of $\sim 2 \times 10^6$. In this regime, other effect might start dominating, we do not expect to see any effect experimentally.

However, as can be seen in Eq. 4.5, to achieve a high photon scattering rate, we cannot use the same state for ($v = 1$) repump, as it will double the number of ground states with unchanged number of excited states, lowering the effective scattering rate. Luckily, repumping on the $B^2\Sigma^+(v = 0,\ N = 0,\ +)$ state is still viable. With a lower chance of being excited, the leak probability is $P_{\mathrm{pd}} \times \mathrm{VBR}_{01} \sim 2.9 \times 10^{-5}$, corresponding to a photon budget of $\sim 3.5 \times 10^4$.

All higher repumps could be done on the A state since it will no longer affect the highest achievable photon scattering rate. Now we recall the ultimate laser cooling scheme shown in Fig. 2.2, with the measurements in this chapter, the reader should have gained more insights to this choice of photon cycling scheme.

Table 5.2: Experimental stages for $B(v' = 0)$ state predissociation measurement. In the second column, $M^R_{v'-v''}$ denotes the laser information. M is A or B, representing the electronic excited state. R is the region S, I, or C (see text). The third column contains the normalized ground-state populations using unknown variables and calculated VBRs. The five variables n_1, κ, F_{B0a}, d_A and d_B represent $X(v'' = 1)$ state natural population, cleanup efficiency of laser B^C_{1-0}, $B(v' = 0)$ state predissociation probability, depletion efficiency of laser A^I_{0-0} and depletion efficiency of laser B^I_{0-0}. We denote the VBR normalization factors as $\mathcal{F}_{A_0} \equiv \sum_{i\neq 0} F_{A0i}$, $\mathcal{F}_{B_0} \equiv F_{B0a} + \sum_{i\neq 1} F_{B0i}$, and $\mathcal{F}_{B_1} \equiv F_{B0a} + \sum_{i\neq 0} F_{B0i}$. Additional information is in Sec. 5.2.4.

Purpose	Upstream Laser Config	Downstream Normalized $X^2\Sigma^+$ $(v'' = 0)$ State Pop	Averaged Signal Ratio
Unperturbed	–	1	–
Cleanup	B^C_{0-1}	$1 + n_1\kappa F_{B00}/\mathcal{F}_{B_0}$	1.05(2)
X–A Cycling	A^I_{0-0}	d_A	0.018(6)
X–A Cycling + Cleanup	$A^I_{0-0} + B^C_{0-1}$	$d_A + [(1-d_A)F_{A01}/\mathcal{F}_{A_0} + n_1]\kappa F_{B00}/\mathcal{F}_{B_0}$	0.94(2)
X–B Cycling	B^I_{0-0}	d_B	0.086(8)
X–B Cycling + Cleanup	$B^I_{0-0} + B^C_{0-1}$	$d_B + [(1-d_B)F_{B01}/\mathcal{F}_{B_1} + n_1]\kappa F_{B00}/\mathcal{F}_{B_0}$	0.87(2)

Table 5.3: Method I of $B^2\Sigma^+$ ($v' = 1$) predissociation measurement. Notation is similar to Table 5.2. In the third column, the variables include a, n_1, κ, F_{B1a} and d_B, representing state preparation (from $X(v'' = 0)$ to $X(v'' = 1)$) efficiency, $X(v'' = 1)$ natural population, cleanup efficiency of laser A^C_{0-1}, $B(v' = 1)$ predissociation probability and depletion efficiency of laser B^I_{1-1}. The VBR normalization factors are $\mathcal{F}_{A_1} \equiv \sum_{i\neq 1} F_{A0i}$, $\mathcal{F}_{A_2} \equiv \sum_{i\neq 0} F_{A1i}$, and $\mathcal{F}_{B_2} \equiv F_{B1a} + \sum_{i\neq 1} F_{B1i}$.

Purpose	Upstream Laser Config	Downstream Normalized $X^2\Sigma^+$ ($v'' = 0$) State Pop	Averaged Signal Ratio
Unperturbed	–	1	–
State Prep	A^S_{1-0}	$1 - a$	0.22(2)
Cleanup	A^C_{0-1}	$1 + n_1\kappa F_{A00}/\mathcal{F}_{A_1}$	1.10(3)
State Prep + Cleanup	$A^S_{1-0} + A^C_{0-1}$	$1 - a + (n_1 + aF_{A11}/\mathcal{F}_{A_2})\kappa F_{A00}/\mathcal{F}_{A_1}$	1.01(3)
State Prep + X–B 1–1 Cycling	$A^S_{1-0} + B^I_{1-1}$	$1 - a + (n_1 + aF_{A11}/\mathcal{F}_{A_2})d_B F_{B10}/\mathcal{F}_{B_2}$	0.39(2)
State Prep + X–B 1–1 Cycling + Cleanup	$A^S_{1-0} + B^I_{1-1} + A^C_{0-1}$	$1 - a + (n_1 + aF_{A11}/\mathcal{F}_{A_2})(d_B F_{B10}/\mathcal{F}_{B_2} + (1 - d_B)\kappa F_{A00}/\mathcal{F}_{A_1})$	0.40(2)

Table 5.4: Method II of $B^2\Sigma^+$ ($v' = 1$) predissociation measurement. In the third column, the 7 variables include a, n_1, κ_1, κ_2, F_{B1a}, d_A and d_B, representing state preparation [from $X(v'' = 0)$ to $X(v'' = 1)$] efficiency, $X(v'' = 1)$ natural population, cleanup efficiency of laser A^C_{1-0}, cleanup efficiency of laser A^C_{1-2}, $B(v' = 1)$ predissociation probability, depletion efficiency of laser A^I_{1-1} and depletion efficiency of laser B^I_{1-1}. The VBR normalization factors are $\mathcal{F}_{A_2} \equiv \sum_{i\neq 0} F_{A1i}$, $\mathcal{F}_{A_3} \equiv \sum_{i\neq 1} F_{A1i}$, $\mathcal{F}_{A_4} \equiv \sum_{i\neq 2} F_{A1i}$, and $\mathcal{F}_{B_2} \equiv F_{B1a} + \sum_{i\neq 1} F_{B1i}$.

Purpose	Upstream Laser Config	Downstream Normalized $X^2\Sigma^+$ ($v'' = 1$) State Pop	Avg Ratio
State Prep + Cleanup $v0$	$A^S_{1-0} + A^C_{1-0}$	$n_1 + (a + \kappa_1 - a\kappa_1)F_{A11}/\mathcal{F}_{A_2}$	–
Unperturbed	–	n_1	0.13(3)
State Prep	A^S_{1-0}	$n_1 + aF_{A11}/\mathcal{F}_{A_2} \equiv \mathcal{Z}$	0.89(4)
Cleanup $v0$	A^C_{1-0}	$n_1 + \kappa_1 F_{A11}/\mathcal{F}_{A_2}$	0.93(4)
State Prep + X–A 1–1 Cycling	$A^S_{1-0} + A^I_{1-1}$	$\mathcal{Z}(1 - d_A)$	0.03(3)
State Prep + X–A 1–1 Cycling + Cleanup $v0$	$A^S_{1-0} + A^I_{1-1} + A^C_{1-0}$	$\mathcal{Z}(1 - d_A) + (1 - a + \mathcal{Z}d_A F_{A10}/\mathcal{F}_{A_3})\kappa_1 F_{A11}/\mathcal{F}_{A_2}$	0.33(3)
State Prep + X–A 1–1 Cycling + Cleanup $v2$	$A^S_{1-0} + A^I_{1-1} + A^C_{1-2}$	$\mathcal{Z}(1 - d_A) + (aF_{A12}/\mathcal{F}_{A_2} + \mathcal{Z}d_A F_{A12}/\mathcal{F}_{A_3})\kappa_2 F_{A11}/\mathcal{F}_{A_4}$	0.57(4)
State Prep + X–B 1–1 Cycling	$A^S_{1-0} + B^I_{1-1}$	$\mathcal{Z}(1 - d_B)$	0.12(3)
State Prep + X–B 1–1 Cycling + Cleanup $v0$	$A^S_{1-0} + B^I_{1-1} + A^C_{1-0}$	$\mathcal{Z}(1 - d_B) + (1 - a + \mathcal{Z}d_B F_{B10}/\mathcal{F}_{B_2})\kappa_1 F_{A11}/\mathcal{F}_{A_2}$	0.35(3)
State Prep + X–B 1–1 Cycling + Cleanup $v2$	$A^S_{1-0} + B^I_{1-1} + A^C_{1-2}$	$\mathcal{Z}(1 - d_B) + (aF_{A12}/\mathcal{F}_{A_2} + \mathcal{Z}d_B F_{B12}/\mathcal{F}_{B_2})\kappa_2 F_{A11}/\mathcal{F}_{A_4}$	0.42(3)

Table 5.5: Spin-orbit matrices accounting for vibrational mixing of the A and B states. The Π_x and Π_y basis states split under SOC to produce $\Pi_{1/2}$ and $\Pi_{3/2}$ states. The top matrix is for $A^2\Pi$ ($v' = 0$) and $B^2\Sigma^+$ ($v' = 0$), while the bottom one is for $A^2\Pi$ ($v' = 1$), $B^2\Sigma^+$ ($v' = 1$) and $B^2\Sigma^+$ ($v' = 0$). The Franck-Condon factor f is introduced to account for the off-diagonal vibrational wavefunction overlap. The diagonal terms represent the energies of unperturbed states. All values are in cm^{-1}.

	$A^2\Pi_x$ ($v = 0,\ m_s = 1/2$)	$A^2\Pi_y$ ($v = 0,\ m_s = 1/2$)	$B^2\Sigma^+$ ($v = 0,\ m_s = -1/2$)
$A^2\Pi_x$ ($v = 0,\ m_s = 1/2$)	0	$-35.5i$	21.5
$A^2\Pi_y$ ($v = 0,\ m_s = 1/2$)	$35.5i$	0	$-21.5i$
$B^2\Sigma^+$ ($v = 0,\ m_s = -1/2$)	21.5	$21.5i$	1400

	$A^2\Pi_x$ ($v = 1,\ m_s = 1/2$)	$A^2\Pi_y$ ($v = 1,\ m_s = 1/2$)	$B^2\Sigma^+$ ($v = 0,\ m_s = -1/2$)	$B^2\Sigma^+$ ($v = 1,\ m_s = -1/2$)
$A^2\Pi_x$ ($v = 1,\ m_s = 1/2$)	0	$-35.5i$	$21.5f$	21.5
$A^2\Pi_y$ ($v = 1,\ m_s = 1/2$)	$35.5i$	0	$-(21.5f)i$	$-21.5i$
$B^2\Sigma^+$ ($v = 0,\ m_s = -1/2$)	$21.5f$	$(21.5f)i$	64	0
$B^2\Sigma^+$ ($v = 1,\ m_s = -1/2$)	21.5	$21.5i$	0	1310

Chapter 6: Laser Slowing of CaH

At this point, we believe laser slowing and MOT should be feasible for CaH, so we proceeded to make all the upgrades in pursuit of this goal, our experiment turned to a building phase. In the coming two chapters, I will describe in detail the necessary system upgrades that allow for a MOT and how we managed to create it in the end.

6.1 Relevant Experimental Hardware

6.1.1 Laser Systems

The first major upgrades are on the lasers. With confirmation of the laser cooling scheme, we turned to commercial high-power solutions. For the main cooling laser addressing the $A^2\Pi_{1/2}(v' = 0,\ J' = 1/2,\ +) \leftarrow X^2\Sigma^+(v = 0,\ N = 1,\ -)$ transition at 695 nm, we use Precilasers' SFG system, where they use two fiber amplified lasers at 1080 nm and 1950 nm and use a nonlinear crystal to sum the two frequencies. This SFG process is typically not efficient at the percent level. But given the high power at these infrared wavelengths, we do not need optical cavities for a higher efficiency. At the time when we purchased the laser, Precilasers was able to generate ~3.5 W of power at 695 nm.

For the ($v = 1$) repump laser addressing the $B^2\Sigma^+(v' = 0,\ N' = 0,\ +) \leftarrow X^2\Sigma^+(v = 1,\ N = 1,\ -)$ transition, we home-built an SFG system for it. One of the frequencies we use is the dumped ~5 W 1950 nm light from Precilasers, and the other frequency is generated with a fiber amplifier from IPG Photonics, operating at 1068 nm, and we use a Precilasers fiber distributed feedback (DFB) laser to seed the IPG system. The nonlinear crystal we use is Covesion MSHG1420-0.5-40. This system could generate up to 1.8 W of power at 690 nm with ~5 W of 1950 nm light and ~15 W if 1068 nm light. For the ($v = 2$) repump laser addressing the $A^2\Pi_{1/2}(v' = 1,\ J' =$

$1/2,\ +) \leftarrow X^2\Sigma^+(v = 2,\ N = 1,\ -)$ transition, we use a Toptica TA pro system that could deliver up to 1.2 W of power at 758 nm.

In the slowing setup, to generate frequency sidebands for the spin-rotation and hyperfine splittings in CaH, we chose to use free-space EOMs. When we were about to make this decision, a technique was first demonstrated for laser cooling molecules, using serrodyne to generate the sidebands [165]. This was intriguing for us because all the power can be used without loss on ineffective sidebands. But for free-space EOMs, since they are resonant, they can only generate sidebands with even spacings. However, we were planning to use the same laser for both slowing and MOT. Since MOT can be quite sensitive to the cleanness of the laser spectrum, and serrodyne may induce small but finite unwanted sidebands, free-space EOMs turned out to be the best solution at the time.

As previously shown in Fig. 2.3, CaH has a ~2 GHz spin-rotation splitting and a ~50–100 MHz hyperfine splitting. For the spin-rotation splitting, we adapted an EOM design from the neighboring Prof. Sebastian Will's group. The design uses acrylic mounts to press a copper sheet on top of an EOM crystal's two gold surfaces, making the inductor (copper sheet) and the capacitor (crystal) parallel. Then a wired antenna is coupled to the copper sheet to deliver rf power. The copper sheet is used because of the low inductance required for high resonant frequency ($f \sim 1/\sqrt{LC}$). Because of the copper sheet, the resonant frequency is very thermally sensitive. With a higher temperature when rf power delivered, the resonant frequency will shift down. As a result, these EOMs have to be constantly on. If they are ever turned off by accident, turning them back on will not bring them back to the same resonance. Because at a colder temperature the resonance shifts and turning on the rf will not deliver power into the system, thus the temperature cannot go back to the same point. Note that this is particularly important when using high laser powers. The spatial profile of the laser could change under different conditions which could lead to a change in the downstream alignments. Mg-doped crystals can mitigate the problem but still cannot solve it completely. This is something that needs to be constantly monitored. EOMs operating at ~50–100 MHz are quite standard, and I will not go into details here. Figure 6.1(a) shows the 695 nm laser modulated by

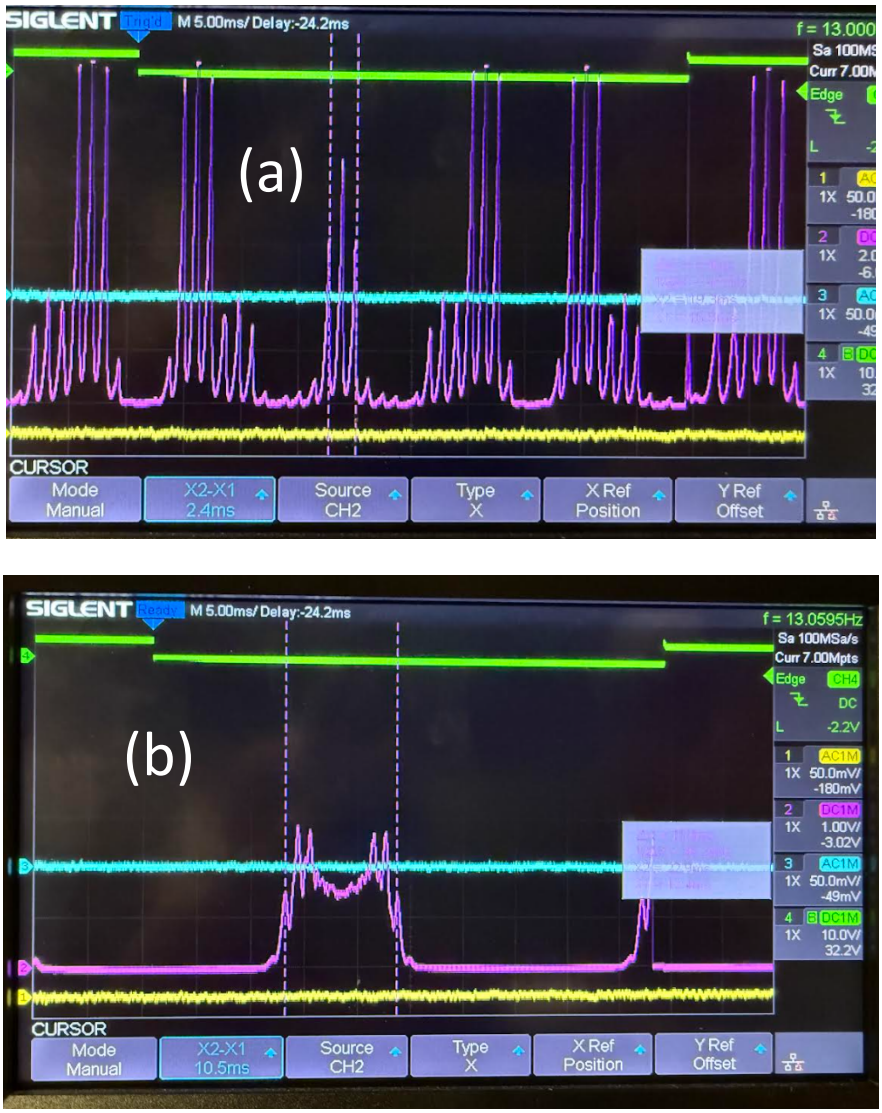

Figure 6.1: Slowing lasers modulated by different EOMs detected on a FPC. (a) The ($\nu = 0$) cycling laser modulated by a 947.1 MHz spin-rotation EOM and a 50.83 MHz hyperfine EOM. Periodic structure arises from the 1.5 GHz FSR of the FPC. (b) The ($\nu = 0$) cycling laser modulated by a white-light (WL) EOM operating at 4.335 MHz and a 50.83 MHz hyperfine EOM.

a 947.1 MHz EOM and a 50.83 MHz EOM detected on a Fabry-Pérot cavity (FPC). Choices of frequencies for the EOMs are determined not by the absolute splitting but by optimizing the depletion (main cycling) or cleanup (repumps) at velocity groups of interest. The modulation depth for both EOMs are around 1 so the ±1 orders are the strongest. The periodic structure is from the 1.5 GHz free spectral range (FSR) of the FPC used (Thorlabs SA30-73). The taller peaks are the ±1 orders of the 947.1 MHz EOM, while the narrower structures are from the 50.83 MHz EOM.

We employ a technique called white-light (WL) laser slowing, which was first introduced in Ref. [166]. We use a strongly driven high-Q EOM operating at ~4 MHz (lower than the natural linewidth of the transitions) to broaden the slowing laser to several hundred MHz, so that the molecules with different velocities (ideally 0–200 m/s) can remain resonant during the whole slowing process. Figure 6.1(b) shows an example of the resulting spectrum of the strongly driven WL EOM operating at 4.335 MHz together with a 50.83 MHz hyperfine EOM. From the known spacing of the 50.83 MHz EOM, we can figure out how much the WL EOM has broadened the slowing laser. We also use a Pockels cell operating at 2 MHz to switch the polarization of the slowing lasers in between two orthogonal linear polarizations to remix the dark state. It is worth noting that we use a Thorlabs EO-AM-NR-C1 EOM and a driver HVSQ-0.3-5000-SMA from EEA Elektronik Adamietz GmbH to serve as a Pockels cell. This combination turns out to be not very stable thermally and is subject to a long-term drift. As a result, we are using this for the slowing lasers where high-contrast polarization switching is not required. For the MOT system in the next chapter, we instead use a Conoptics Pockels cell for better stability. Figure 6.2 shows a detailed schematic of how the slowing lasers are generated.

Because of the growing number of lasers required in the experiment, we also upgraded our wavemeter locking system. Previously, the wavemeter is seeded by a commercial fiber switch with 8 input channels, corresponding to the 8 readout channels of the wavemeter. Commercial fiber switches are typically not that broad in wavelength, sending lasers outside the range could damage the switch over time. In order to monitor more than 8 channels with a wider wavelength range, we use a home-built galvo-based fiber switch. The basic idea is, we fiber couple 16 potential laser channels into a single fiber, with each corresponding to a different tilt angle of the galvo mirror (Thorlabs GVS002) controlled by analog input voltages. By synchronizing the wavemeter readout time and galvo analog input voltages, we can make the wavemeter read the 16 laser frequencies on the 8 wavemeter channels (for example at a certain wavemeter channel, one laser is sent in half of the time, and another laser is sent in the second half of the time). For this system, we adapted a full system including an electronic control board and a control software from the Doyle group.

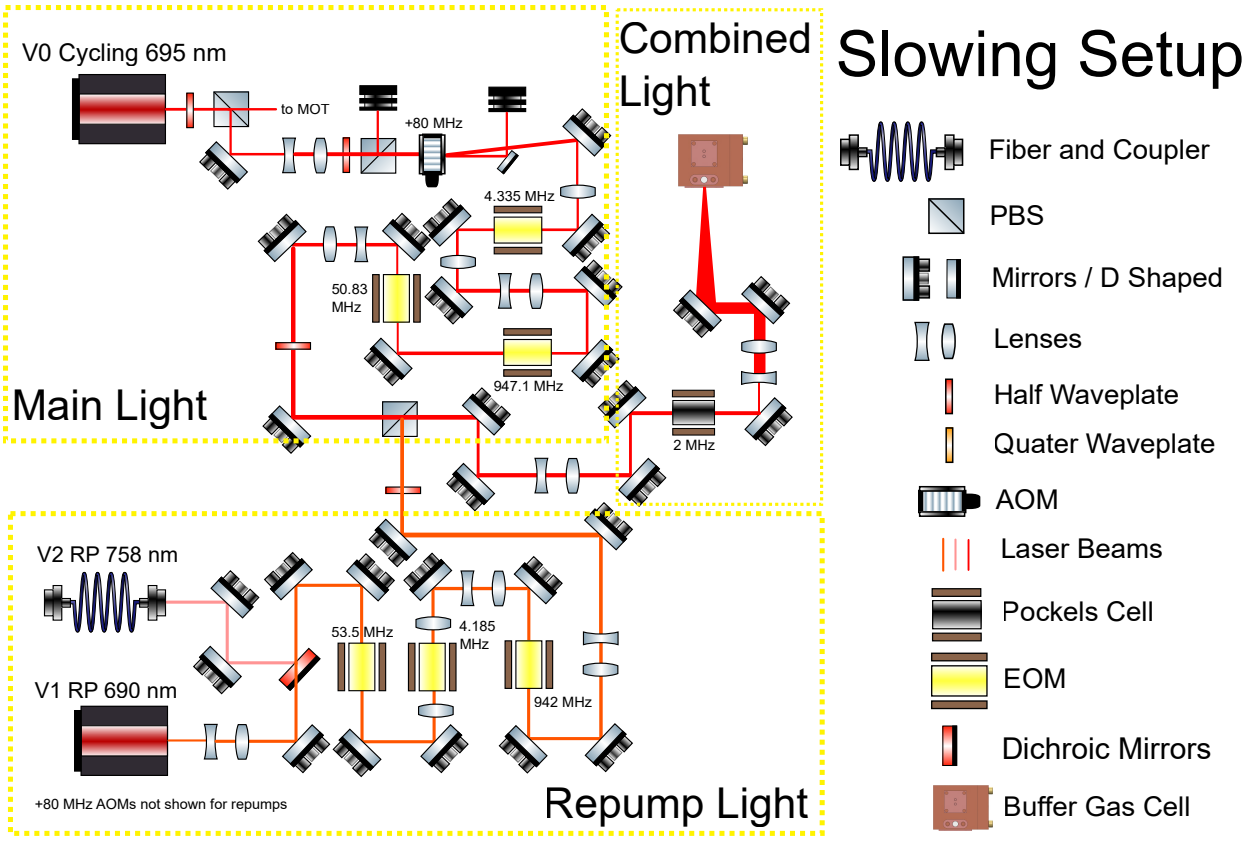

Figure 6.2: Optical path layout for slowing lasers. Different EOMs are used to generate the frequency sidebands for spin-rotation splitting, hyperfine splitting, and WL. This figure is reproduced from Ref. [137], with corrected frequencies and order of the acousto-optic modulator (AOM).

6.1.2 Ultrahigh Vacuum System

The beamline for the 1D cooling experiment and predissociation measurement was retired, and we upgraded to an ultrahigh vacuum (UHV) chamber to incorporate slowing and MOT experiments. The main MOT chamber we chose Kimball Physics MCF800-SphSq-G2E4C4A16 for its maximum optical access from different angles. MOT also requires a high magnetic field gradient, and we decided to go for an rf MOT solution. The reason is that, since we do not know how much trapping force is required for CaH and rf MOTs are known to provide the highest trapping force, they are safer for the first attempt. However, high rf currents are more challenging than high dc currents, so in order to generate a high enough magnetic field gradient, the MOT magnetic field coils have to be put in vacuum. This is not the end of the world as long as we do a good thermal

contact to outside of the UHV chamber so the heat can be dissipated, and also do a small duty cycle on the MOT operation (this in some sense is automatic since typical molecular MOT loading time is at the 10 ms level and experiment cycle time is at the 1 s level). Figure 6.3 shows the in-vacuum MOT coils and the MOT chamber. The coil design is adapted from the Doyle group. In order to minimize the scattered light in the vacuum chamber, the whole interior is painted with vacuum-compatible black paint. Figure 6.3(a) is the MOT coils after painted. The molecules travel through the middle of the top and bottom plates, which are spaced by 1 inch. The spiral in the middle are the coils, and the elliptical holes are for optical access of the small windows on the Kimball

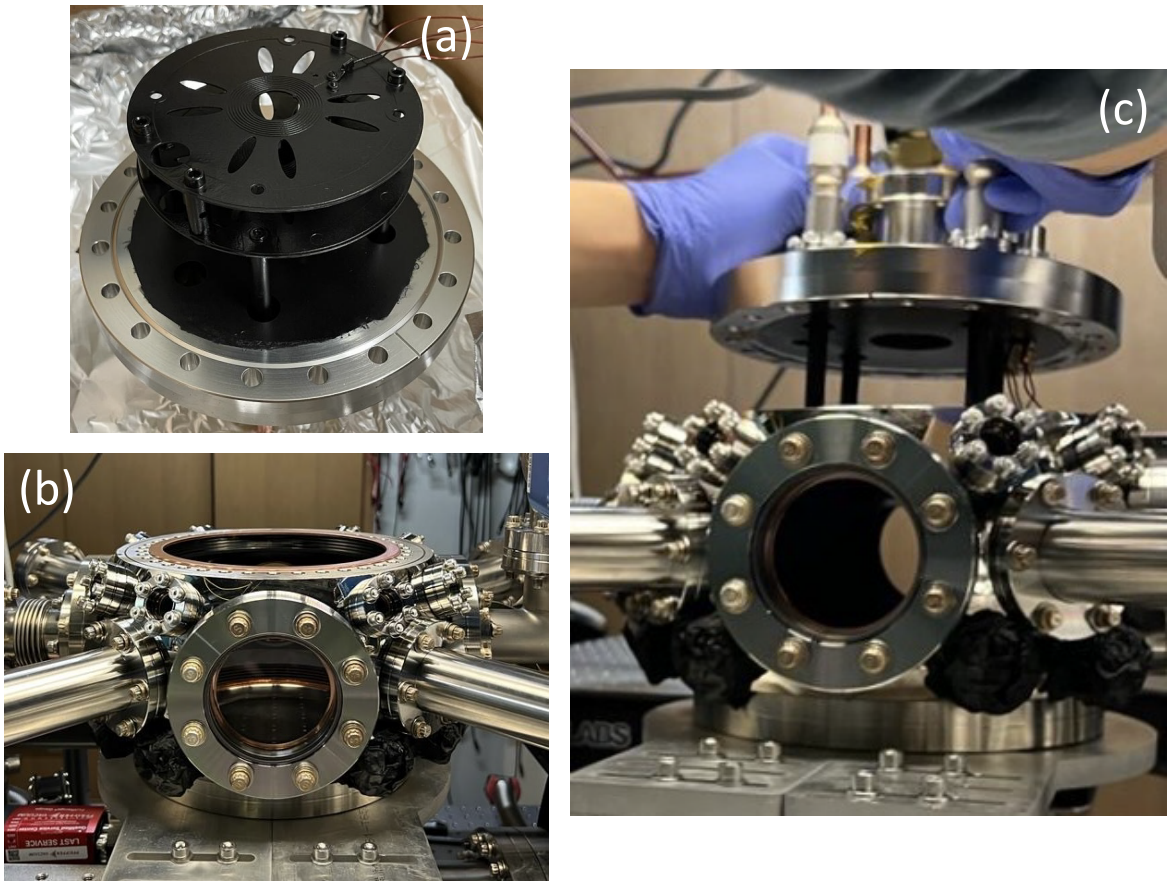

Figure 6.3: Pictures of the MOT chamber. (a) In-vacuum MOT coils after painted. Molecules travel through the middle of the two plates, which are spaced by 1 inch. The spiral in the middle of the plate is the coil, and the elliptical holes are for optical access of the small windows on the chamber. The MOT coils are thermally connected to outside the vacuum through the holding structure. (b) Kimball Physics chamber. (c) During assembly, a picture from a different angle of the MOT coil for a better vision of the structure.

Physics chamber. The MOT coils are thermally connected to the outside of the vacuum through the holding structure. Figures 6.3(b)–6.3(c) are the actual MOT chamber and a picture during assembly. With appropriate vacuum pumping and baking, the pressure of the MOT chamber went down to 10^{-10} Torr at the lowest. We note that this pressure is already low enough given the buffer gas required for the experiment. With H_2 and He flowed into the system, the pressure can go up to the 10^{-8} Torr level.

To achieve a higher photon collection efficiency for LIF signals, we also added an in-vacuum lens, as shown in Fig. 6.4. The lens we use is an uncoated UV fused silica aspheric lens with an effective focal length of 30 mm and a diameter of 25 mm (Edmund Optics Stock #48-537). The

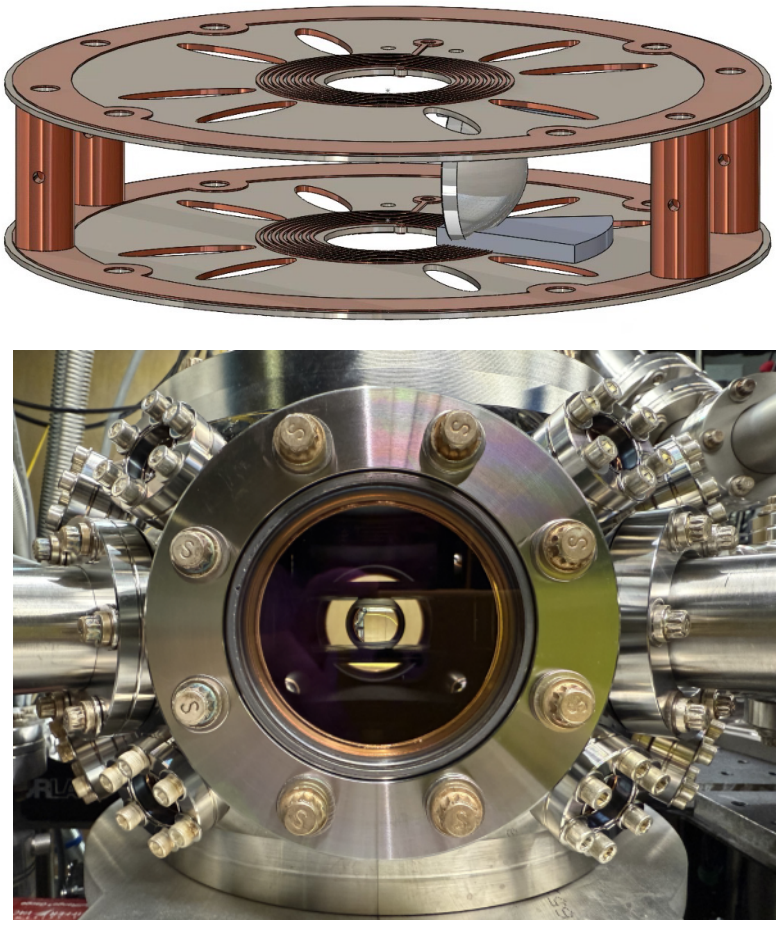

Figure 6.4: In-vacuum lens for higher photon collection efficiency. Top is a rough drawing of how the lens is mounted. The coil and lens holder designs are modified slightly for the final version used in the experiment. Bottom is a picture after the lens was installed.

collection efficiency can in principle increase from ∼1% to ∼5%. However, COMSOL simulation shows a collection efficiency of ∼3% in this system due to the spatial constraints on the top and bottom edges and the finite distance between the lens and the window of the chamber. Nevertheless, we expect an improvement for the photon collection efficiency.

6.2 Two-Photon Background-Free Velocity Detection

Even with the best blackening we can do, the small LIF of the molecules is still going to be buried in the background scattered light in the chamber if using a non-background-free detection scheme. It is always best practice to have background-free (BGF) detection schemes for any measurements we take. For velocity detection, there have been a two-photon BGF detection scheme first introduced in Ref. [167]. The basic idea is, instead of using just a cycling transition like $A \leftarrow X$, we apply a second laser exciting the molecules from A to a higher excited state, the decay from the higher excited state back to the ground state will be a different and higher photon energy, detecting such photons is thus BGF. Also ideally, we would want to use a different A state from the main cycling laser, $A^2\Pi_{1/2}(v = 0,\ J = 3/2,\ +)$ for example, to avoid interfering with laser slowing.

Among the different excited electronic states, we chose the E state in the end because it is the only one with measured lines besides the A and B states [168]. The corresponding measurement scheme for CaH is shown in Fig. 6.5(a). A challenge immediately pops up, there was no straightforward laser options in the wavelength range ∼1668 nm. Luckily again, we were able to find a laser diode that could operate around this wavelength, Seminex TO0-174-161. Though the diode is preferred to operate in a pulsed mode, we can still use it in the CW mode. There was a bit of engineering challenge to put it to the right wavelength, the operating temperature needs to be at around 0 °C. We designed a small chamber to shield our home-built ECDL, and fill the chamber with N_2, the laser can then be cooled down to this low temperature without water condensation. Note also that because of the huge temperature difference on the thermoelectric cooler, the whole chamber needs to be water cooled, otherwise the laser would not be able to reach the desired temperature.

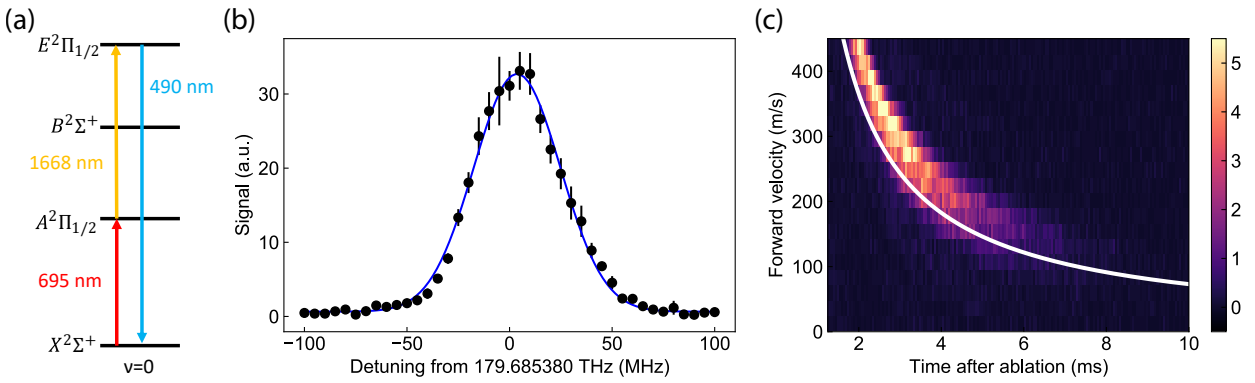

Figure 6.5: Two-photon BGF velocity measurement. (a) Measurement scheme. The molecules are excited with two lasers, with the first addressing an $A \leftarrow X$ transition, and the second addressing an $E \leftarrow A$ transition. The LIF of the decay from the E state back to X state at ~490 nm is detected on a PMT. (b) Spectrum of the $E^2\Pi_{1/2}(v' = 0,\ J' = 3/2,\ -) \leftarrow A^2\Pi_{1/2}(v = 0,\ J = 3/2,\ +)$ transition. Hyperfine structure remains unresolved at this precision. (c) A sample velocity measurement of the chemically produced CaH molecular beam, with the $E \leftarrow A$ laser applied in a velocity sensitive configuration (45°with respect to the molecular beam in this measurement). LIF from the $E \rightarrow X$ decay detected on a PMT. x-axis is the time of arrival on the PMT, while y-axis is the velocity group selected with detuning from the $E \leftarrow A$ transition. Solid white line is a guide to eye of a ballistic propagation from the cell to the detection region.

Another challenge is that our wavemeter cannot directly read this wavelength, so we home-built an SHG system (using Covesion MSHG1650-0.5-40) and measure the frequency of the doubled 834 nm light. Given these challenges, it really took us a long time to find even just a single line in the E state.

Figure 6.5(b) shows one of the measured lines, $E^2\Pi_{1/2}(v' = 0,\ J' = 3/2,\ -) \leftarrow A^2\Pi_{1/2}(v = 0,\ J = 3/2,\ +)$. Since we are using the $A^2\Pi_{1/2}(v = 0,\ J = 3/2,\ +)$ state, we used an additional laser addressing the $A^2\Pi_{1/2}(v' = 0,\ J' = 3/2,\ +) \leftarrow X^2\Sigma^+(v = 0,\ N = 3,\ J = 5/2,\ -)$ besides the $A^2\Pi_{1/2}(v' = 0,\ J' = 3/2,\ +) \leftarrow X^2\Sigma^+(v = 0,\ N = 1,\ -)$ transition to achieve rotational closure. Once the laser frequency is confirmed, following Prof. Stefan Truppe's suggestion, we ordered a VECSELS laser system from Vexlum. They are able to provide ~1 W of power at ~1668 nm. It is important to have as high of a power as possible for velocity detection so that we can saturate the transition for a higher SNR. In practice, ~300 mW is enough for velocity measurements. By applying the $E \leftarrow A$ laser in a velocity sensitive configuration, we can measure the forward velocity of the CaH molecular beam. Figure 6.5(c) shows a sample measurement.

Velocity group is selected by detuning the $E \leftarrow A$ laser. As one can tell, the forward velocity of the chemically produced CaH molecular beam peaks at ~250–300 m/s, which is not ideal. Given a MHz-level scattering rate and ~1 m slowing distance, we can probably only laser slow velocities up to ~150 m/s, so we are really relying on the slower velocity tail of the distribution.

6.3 White-Light Laser Slowing

Typical capture velocity of molecular MOTs is $\lesssim$10 m/s. In order to load molecules into a MOT, we would need to first slow the velocity of the molecular beam from ~200 m/s close to this range. For the first attempt of laser slowing, we decided to pursue white-light slowing because of the smaller parameter space.

Due to the predissociative loss in CaH, the number of photons that could be scattered during the slowing process is limited. As a result, we would ideally want to start with as slow of a molecular beam as possible. However, as mentioned before, the unique property of H_2 helps with the overall molecule production but boosts the velocity of the molecular beam to peak at ~250–300 m/s. With a slowing distance of ~73 cm (from the cell aperture to the center of the MOT chamber), photon scattering rate of $\sim 10^6$ s^{-1}, and a photon recoil velocity of $\hbar k/m \approx 1.4 \times 10^{-2}$ m/s, only molecules with velocities below ~170 m/s could be slowed to this range. Here k is the wavenumber of a 695 nm photon, and m is the mass of a CaH molecule. The good news is, we can still measure a small amount of CaH molecules below this velocity and down to ~100 m/s.

About three years ago, Nathaniel Vilas on the CaOH project in the Doyle group paid a visit to us, and described a bizarre cell performance. They observed that, if they prefire the YAG about tens of milliseconds before, the resulting molecular beam will be a little slower. Their explanation is, the prefire melts a certain amount of ice in the cell (they flow water to produce CaOH molecules), which leads to a better thermalization, thus reducing the forward velocity. Thanks to this small tip, we were able to bring down the beam velocity a little more. Figure 6.6(a) shows a comparison of the CaH beam velocity with (double ablation) and without (single ablation) a prefire. The YAG is prefired 20 ms for double ablation. We observe a big improvement of molecule number in

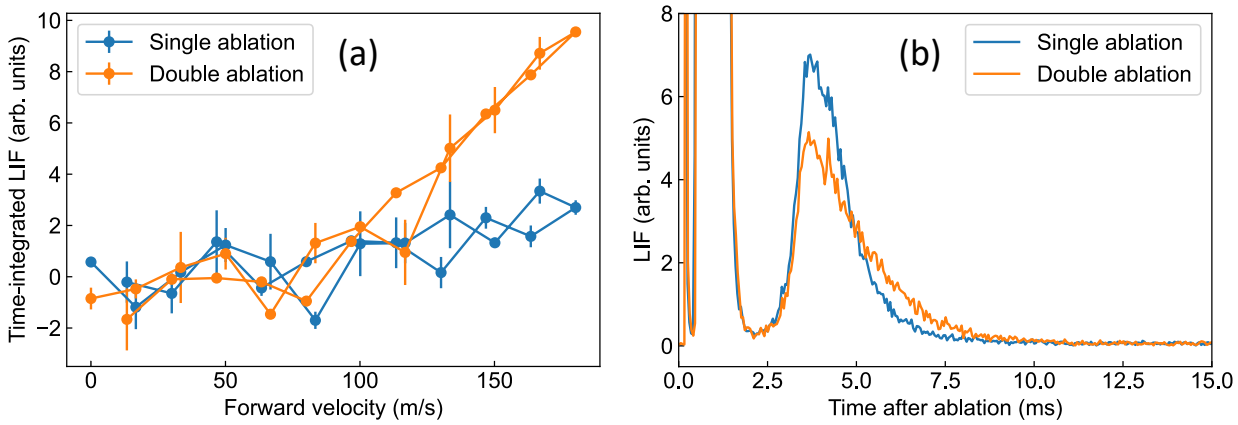

Figure 6.6: Beam velocity with double ablation. (a) Measured forward velocity of the CaH molecular beam with single and double ablation. The prefire time for double ablation is 20 ms. An improvement of molecule number in the 100–200 m/s velocity group is observed with double ablation. (b) Arrival time of the molecules detected through LIF on the slowing lasers. Later arrival time with double ablation also indicates a slower velocity.

the 100–200 m/s velocity range. Figure 6.6(b) shows the arrival time of the molecules with and without the prefire, which is detected through the LIF on the slowing lasers. The slowing lasers [including the ($v = 0$) main cooling laser at 695 nm, ($v = 1$) repump laser at 690 nm, and ($v = 2$) repump laser at 758 nm] are kept on while the molecules are flying by, and the 635 nm LIF from the $B^2\Sigma^+(v' = 0,\ N' = 0,\ +) \rightarrow X^2\Sigma^+(v = 0,\ N = 1,\ -)$ decay is detected on a PMT. The later arrival time with double ablation also indicates a lower forward velocity. We scanned this prefire time in the 20–100 ms range, and found that the shorter this time the better. We set the prefire time to be 20 ms in the end, and all the slowing measurements are done in this configuration.

The first thing to make sure for laser slowing is if we can achieve a high scattering rate with lasers in the longitudinal direction with respect to the molecular beam. Because of the fast molecular beam, we do not want to address the whole velocity profile, optimizing laser frequencies with overall molecule number depletion is not a good idea. We instead look at depletion and or depletion-revival with certain velocity groups. For ($v = 0$) main cooling laser, we measure depletion with the WL and spin-rotation 1 GHz EOMs off. With the depletion spectrum, we can extract the optimal frequency setpoint for the 1 GHz EOM of the main cooling laser. For the frequency setpoints of the repump lasers, we first deplete with the main cooling laser and revive the molecules

back to the ($v = 0$) state with the repump laser with these EOMs off, and the optimal frequency setpoint can be extracted from this depletion-revival spectrum.

Next, we also need to consider how wide a velocity range we should cover for the WL. This is mostly determined by how high of a photon scattering rate we can achieve. Assuming a scattering rate of $\sim 10^6$ s^{-1}, in the most ideal case, we would want to cover the velocity range up to $\sim$150 m/s. A problem for CaH is the large hyperfine splittings in the $\sim$50–100 MHz range. As a result, the same laser frequency may be resonant with velocities different by $\sim$50 m/s in different hyperfine states. If we want to cover the same velocity range for all hyperfine states, a much broader WL spectrum is needed, leading to an inefficient power usage. With these considerations, we in the end determined the following setpoints for the slowing laser. The spin-rotation and hyperfine EOMs of the main cooling laser is set to be 947.1 MHz and 50.83 MHz, respectively. The WL EOM operating at 4.335 MHz (this number is arbitrary as long as it is smaller than the natural linewidth), together with the hyperfine EOM, generates a frequency broadening of 402 MHz. The two repump lasers share the same set of EOM series, with spin-rotation and hyperfine EOMs operating at 942 MHz and 53.5 MHz. The WL EOM of repump lasers, together with their hyperfine EOM, generates a frequency broadening of 424 MHz. The repump lasers are set to be broader to cross zero velocity so it can also serve as repumps for the MOT. A detailed optical path layout can be found in Fig. 6.2. The center frequencies of the slowing lasers before modulated by these EOMs are summarized in Table 6.1.

A few more parameters need to be considered for slowing: when to start and how long, and what size to use for the slowing laser beams. First, we find that, if starting slowing too early when the molecules are not fully extracted from the cell, the molecules will be depleted by the slowing

Table 6.1: Center frequencies of the slowing lasers, measured on a HighFinesse WS7-60 wavemeter.

Ground	v	N	J	F	Excited	v'	N'	J'	F'	Frequency (THz)
X	0	1	1/2, 3/2	$0, 1^+, 1^-, 2$	A	0	–	1/2	0, 1	431.275351
X	1	1	1/2, 3/2	$0, 1^+, 1^-, 2$	B	0	0	1/2	0, 1	434.255716
X	2	1	1/2, 3/2	$0, 1^+, 1^-, 2$	A	1	–	1/2	0, 1	395.717941

lasers. A possible explanation is that, the buffer gas density is high near the cell exit, the molecules excited by the slowing laser may be scrambled to opposite parity states and thus can no longer be detected in the normal photon cycling transitions. The extraction time of our cell is quite fast at ~1 ms, so we can still turn on slowing quite early. The slowing start time is chosen to be 1.2 ms in the end, but we later find that this start time can be tolerant, the MOT will still work with a 2 ms start time. As for the size of the slowing laser beams, we would ideally want them to be as big as possible so that we can cover the big molecular beam. However, if too big, we might starve with laser power. We chose a ~1.5 cm $1/e^2$ Gaussian diameter, measured before sent into the vacuum chamber. The slowing laser is gently focused into the cell, with a 0.8 cm diameter at the cell exit and a 1.3 cm diameter at the center of the MOT chamber.

Because of the long lever arm of all the frequency modulations required, the spatial mode of the slowing laser beams becomes slightly non-Gaussian. As a result, co-aligning the slowing lasers can be tricky. To solve this problem, we use a set of motorized flipper mirrors to switch between free space and fiber coupling. This turned out to be very important, because if the slowing lasers are not aligned well through the crystals, the resulting additional non-Gaussianity will mess up co-alignment (two points aligned do not guarantee co-alignment throughout). Coupling the slowing lasers at different wavelengths into the same fiber would guarantee a good co-alignment. Note that the fiber to be used here needs to be a photonic crystal fiber. Because of the same mode field diameter across a large wavelength range, fiber coupling efficiency can be high for all three wavelengths of the slowing lasers. Ensuring high fiber coupling efficiency for the three wavelengths will lead to both good Gaussian mode and good co-alignment.

With all the above considerations taken care of, we were able to observe decent laser slowing with velocities close to zero. Figure 6.7(a) shows the differential LIF obtained by subtracting the LIF of the unperturbed molecular beam from the LIF of the laser slowed beam. The laser powers used are 1.2 W, 0.9 W, and 0.3 W for the main cooling laser, ($v = 1$) repump laser, and ($v = 2$) repump laser, respectively. Slowing is on for 10 ms in this measurement. We observe a substantial molecule population with lower velocities, as shown in red. Initially, we were worry

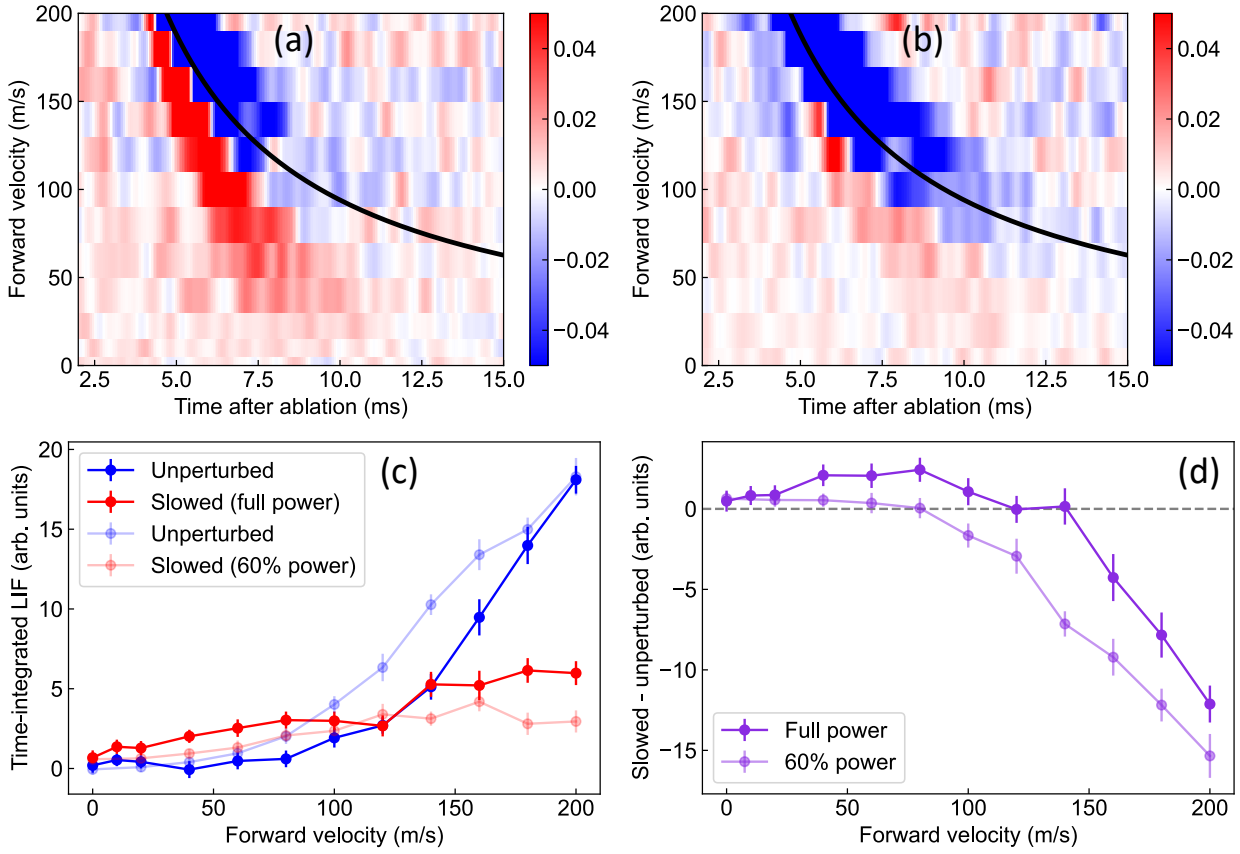

Figure 6.7: Laser slowing with full (free-space) and 60% (fiber coupled) of power. (a) Differential LIF (unperturbed molecular beam subtracted from slowed molecular beam) with free-space slowing lasers. With laser slowing, a substantial molecule population is observed with low velocities (red region). (b) Differential LIF with fiber coupled slowing lasers. (c) Time-integrated LIF at different velocities for the two configurations. (d) Differential (unperturbed subtracted from slowed) time-integrated LIF for the two configurations.

about the co-alignment of the slowing lasers, so we were trying laser slowing with the slowing lasers fiber coupled. The ~40% loss in fiber coupling actually led to a significantly worse laser slowing, as shown in Fig. 6.7(b). This data was taken with a better cell performance, but the red region for slower velocities is smaller, and there is barely any population close to zero velocity. Figure 6.7(c) shows time-integrated LIF at different velocities for the two configurations, the free-space full power slowing clearly has more slower molecules. Figure 6.7(d) shows the differential time-integrated LIF for the two configurations. We are still in the linear regime for slowing power.

With the decent laser slowing observed, we proceeded to finely tune the parameters to ensure the existence of molecules near zero velocity, and we detect the velocity in the MOT region (above

measurements are done in a later region, ~1 m from the cell, MOT region is ~73 cm from the cell). And we find that the existence of "zero" velocity molecules is pretty robust against small change of slowing parameters. Part of the reason could be power broadening of the $E \leftarrow A$ laser, a faulty low velocity could be detected when the molecules are actually at slightly higher velocity. Figure 6.8 shows laser slowing measured in the MOT region, with 15 ms of duration instead of 10 ms in the measurements in Fig. 6.7. The inset of Fig. 6.8(b) shows the LIF with and without laser slowing when the detection laser is tuned to resonance (for "zero velocity"). A small amount of very slow molecules near zero velocity is observed.

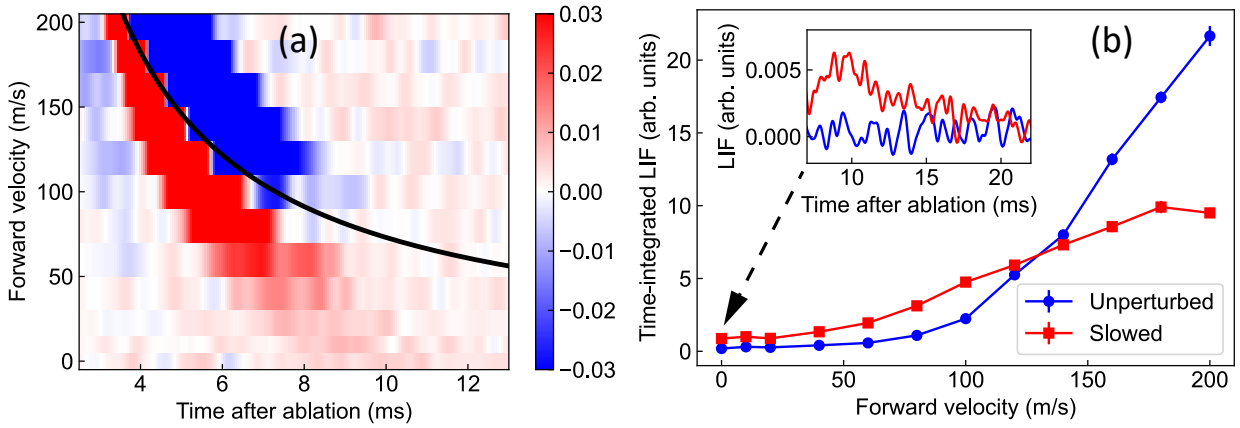

Figure 6.8: Laser slowing measured in the MOT region. (a) Differential LIF obtained by subtracting the unperturbed molecular beam from the slowed molecular beam. Decent slowing effect is observed. (b) Time-integrated LIF at different velocities. With laser slowing, molecules near zero velocity are observed, as in the inset.

Chapter 7: Magneto-Optical Trapping of CaH

With confirmation of an efficient laser slowing, we proceeded to look for a MOT. Our former postdoc Prof. Debayan Mitra would always say, you will see a MOT the second day you see a good slowing. Unfortunately, this was not the case for us. In this chapter, I describe how we figured out the last few pieces of the puzzle.

7.1 Relevant Experimental Hardware

7.1.1 Laser Systems

MOT requires lasers with a clean spectrum, as a result, we cannot use EOMs to generate frequency sidebands for the spin-rotation and hyperfine splittings. Due to the large spin-rotation splitting of CaH at ~2 GHz, we would need a series of acousto-optic modulators (AOMs) as frequency shifters to cover this big gap. Figure 7.1 shows the layout for the optical path of the MOT lasers. We use a 650 MHz AOM, a double-passed 342 MHz AOM, and a double passed 272 MHz AOM to cover the spin-rotation splitting. The double-passed AOMs are powered with voltage controlled oscillators, which can be used to ramp the MOT laser frequencies. The 82 MHz and 53.2 MHz AOMs are for the hyperfine splittings. Because of the many EOMs used in this system, the power efficiency of this system is quite low. We split ~400 mW from the Precilasers 695 nm SFG laser system and only get ~20 mW out of each hyperfine state. In order to achieve a higher power, we seed these four hyperfine fibers to four home-built ILA systems, the output of which can reach ~100 mW for each hyperfine state.

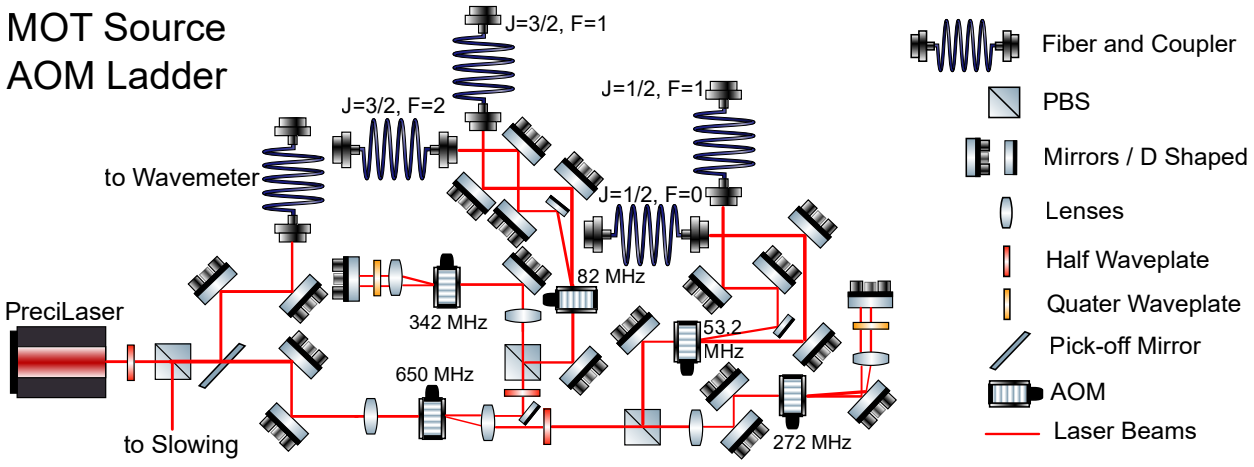

Figure 7.1: Optical path layout for MOT lasers. We use a 650 MHz AOM, a double-passed 342 MHz AOM, and a double-passed 272 MHz AOM to cover the spin-rotation splitting. The 82 MHz and 53.2 MHz AOMs are for the hyperfine splittings. This figure is reproduced from Ref. [137], with corrected frequencies and AOM orders.

7.1.2 Radio-Frequency MOT Configuration

Because of the existence of dark states in the photon cycling scheme in molecules, molecular MOTs do not work easily like Type-I atomic MOTs. There have been a variety of approaches to solve the dark state problems for molecular MOTs, including a dc MOT configuration, dual frequency MOT configuration, and also an rf MOT configuration. The pioneering work with SrF and CaF molecules [75, 131] has shown the larger molecule number of the rf MOT configuration, CaH as an imperfect laser cooling candidate with a low molecular production, it is best practice to start with this configuration. At a certain polarization and magnetic field gradient, molecules would go into a dark state after scattering a few photons. The idea is, at this time, if we switch the polarization and magnetic field gradient, the molecules will become bright again. If we keep switching the polarization and magnetic field gradient at a rate close to the photon scattering rate, the molecules can always be bright and be trapped in the MOT, as indicated from Fig. 7.2(c).

Figure 7.2(a) shows a schematic for the MOT experiment. The experiment starts with the chemically produced CaH CBGB source. An pulsed Nd:YAG laser ablate on a solid Ca target and create a hot plume of Ca atoms. The Ca atoms then react with the H_2 flowed in at ~1 SCCM and get futher buffer gas cooled with He flowed in at ~0.9 SCCM. The molecules extracted from the buffer

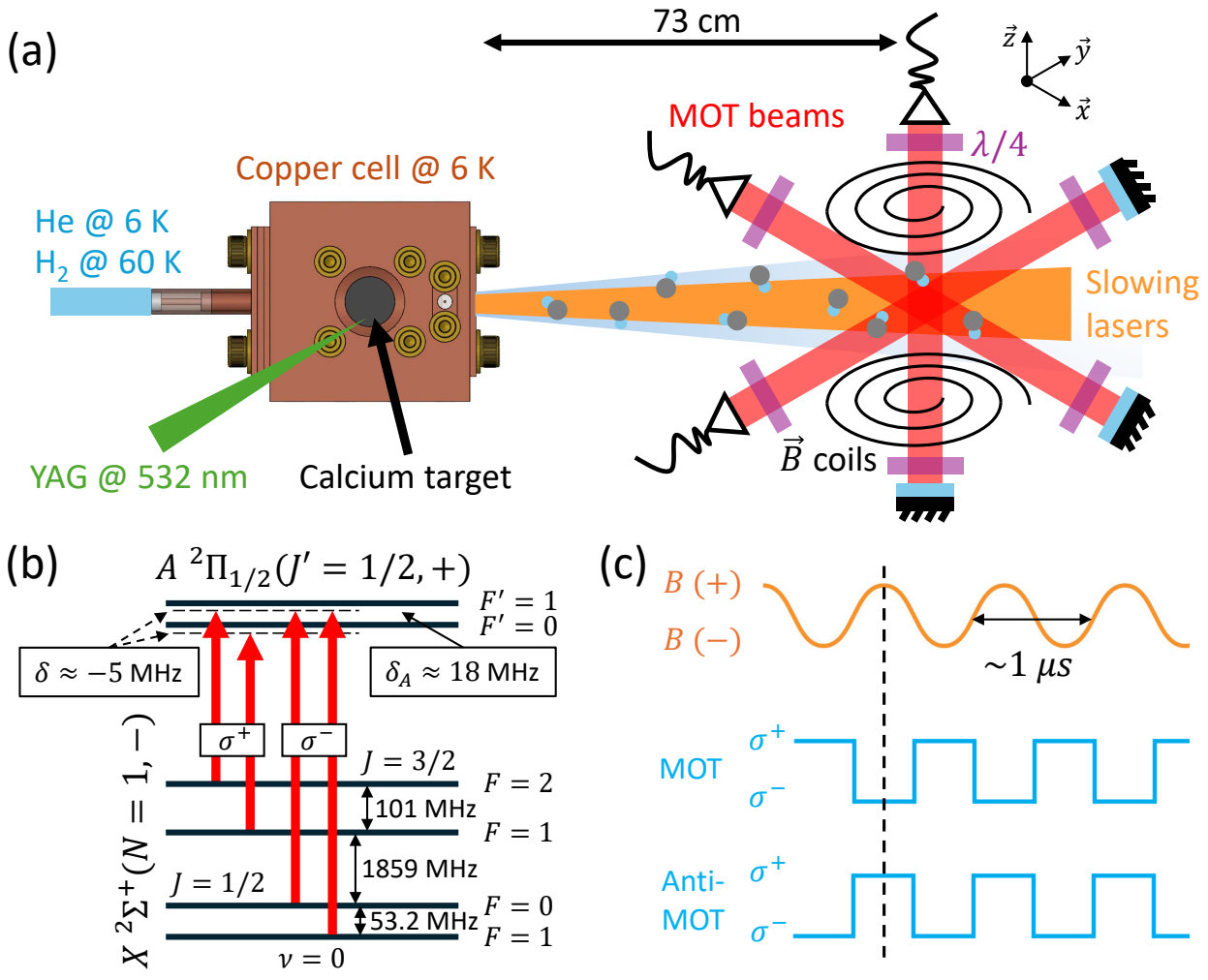

Figure 7.2: (a) Schematic of the MOT experiment. CaH molecules are generated with a CBGB source at ~6 K, and they are subsequently laser slowed and reach the MOT region to be trapped. (b) Laser configuration for the MOT. At a certain magnetic field gradient, the polarization for the ($J = 1/2$) and ($J = 3/2$) states are orthogonal because of the opposite g-factors. The $A^2\Pi_{1/2}(v = 0,\ J = 1/2,\ +)$ state has a hyperfine splitting $\delta_A \approx 18$ MHz. (c) Radio-frequency MOT configuration. Trapping and anti-trapping can be achieved by tuning the relative phase between the magnetic field gradient and the polarization of the MOT lasers.

gas cell are laser slowed in the configuration described in the previous chapter and finally reach the MOT region ~73 cm away from the cell exit. Figure 7.2(b) shows the laser configuration for the MOT. At a given magnetic field gradient, the polarization of the two spin-rotation manifolds $J = 1/2$ and $J = 3/2$ need to be orthogonal because of the opposite g-factors. Moreover, the $A^2\Pi_{1/2}(v = 0,\ J = 1/2,\ +)$ state has a hyperfine splitting $\delta_A \approx 18$ MHz. This has been long overlooked previously, and is the primary reason why we did not see a MOT at the beginning.

More details will be provided later. Figure 7.2(c) shows how the laser polarization and magnetic field gradient are switched in the rf MOT configuration. We use a resonant tank circuit to drive the magnetic field coil. The two coils have their own tank circuits, but the impedance matching is done in the final anti-Helmholtz configuration for the MOT, and each coil is driven with a 50 W amplifier. The tunable capacitor in the tank circuit is Comet CVUN-1500AC/4-BEAA and allows for a frequency range of 800–1200 kHz. Given the geometry of our MOT coil, the magnetic field gradient is 4.83 G/cm/A in the axial direction. With proper tuning of the tank circuits, the peak current that can be delivered is ∼12 A. A peak magnetic field gradient of more than 50 G/cm is more than enough for a MOT. The polarization switching of the MOT lasers can be achieved with a Pockels cell, as also used for dark state remixing for laser slowing. For the MOT, we use a Conoptics M350-50 EO Pockels cell and Conoptics Model 302A driver to drive it. This system has a better thermal stability than the one we used for the slowing lasers. The polarization can be switched with high contrast using the Pockels cell. We combine the four hyperfine ILAs and send them through the Pockels cell for polarization switching at 0.9 MHz (to make sure they can be synchronized, the rf frequency for the magnetic field gradient is also set to be 0.9 MHz). and then split into three fibers to the three MOT arms. An AOM is used for the combined light before the Pockels cell to serve as both an on/off switch and a power ramp control. In the experiment, we can tune the phase between the magnetic field gradient and the polarization, and when they are matched according to the g-factors, it will provide a trapping force (MOT), otherwise it will be an anti-trapping force (antiMOT).

7.2 To Observe a MOT Effect

3D MOT will only work with all aspect mentioned above working together well. Because of the unique property of H_2, it also took us a long time to understand how to perform laser slowing effectively. Apart from the several aspects mentioned in the previous chapter, how to make the buffer gas cell reach the performance that would allow laser slowing is also important. One notable example is we do not want to flow too much H_2 for laser slowing as when we were

characterizing the cell in Chapter 3 (tens of SCCM back then). We need to slowly charge the cell, with ~1 SCCM of H_2 in the first day of data taking. The molecule number will slowly go up and reach a high level. At a certain point, a warm-up and cool-down cycle would also increase the molecular yield. On the MOT side, we would also want to make sure the lasers are well aligned with the zero magnetic field point so that a reasonable MOT force can be applied. Following other molecular laser cooling teams' suggestions, we make our MOT laser beams large with a $1/e^2$ Gaussian diameter of ~1.7 cm. This first simplifies alignment to just geometric center without the need to check the zero magnetic field point with molecules, especially when the signal is low for CaH, and second increases the trapping volume, for heavier molecules this is particularly important.

However, back at this point, with everything we tried to optimize and do our best, we could not see a 3D MOT. And the last thing we tried, is to double check the MOT laser frequencies, which was supposed to be the numbers we have been trusted for years, and they were actually the problem.

7.2.1 $A^2\Pi_{1/2}(v = 0,\ J = 1/2,\ +)$ Hyperfine Splitting

In the seminal paper that brought the the idea of molecular laser cooling by M. D. Di Rosa [169], the author has reported a hyperfine splitting in the $A^2\Pi_{1/2}(v = 0,\ J = 1/2,\ -)$ state. However, for all beam experiments performed till now, we have not seen much evidence of any hyperfine splitting in the $A^2\Pi_{1/2}(v = 0,\ J = 1/2,\ +)$ state. It turned out to be because all these measurements are done with linearly polarized lasers in the beam. When we checked the resonance with the MOT lasers, the hyperfine splitting immediately showed up. Figure 7.3 shows the spectra when we scan the MOT laser with a single frequency component. Instead of 4 lines if there is no excited state splitting, we observe 6 lines. By fitting the frequencies of these 6 lines, we extract a $A^2\Pi_{1/2}(v = 0,\ J = 1/2,\ +)$ splitting $\delta_A \approx 18$ MHz. Since MOT lasers are circularly polarized instead of linearly polarized, some lines, $A^2\Pi_{1/2}(v' = 0,\ J' = 1/2,\ F' = 0,\ +) \leftarrow X^2\Sigma^+(v = 0,\ N = 1,\ J = 1/2,\ F = 1,\ -)$ and $A^2\Pi_{1/2}(v' = 0,\ J' = 1/2,\ F' = 0,\ +) \leftarrow$

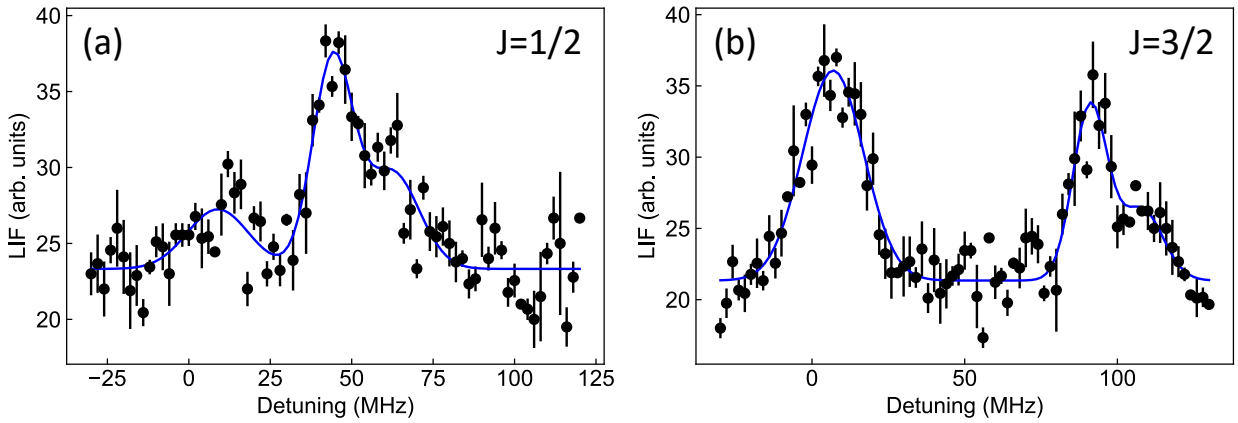

Figure 7.3: Measurement of the $A^2\Pi_{1/2}(v = 0,\ J = 1/2,\ +)$ hyperfine splitting. (a) Spectroscopy with laser at around the $A^2\Pi_{1/2}(v' = 0,\ J' = 1/2,\ +) \leftarrow X^2\Sigma^+(v = 0,\ N = 1,\ J = 1/2,\ -)$ transition. (b) Spectroscopy with laser at around the $A^2\Pi_{1/2}(v' = 0,\ J' = 1/2,\ +) \leftarrow X^2\Sigma^+(v = 0,\ N = 1,\ J = 3/2,\ -)$ transition. According to the fit, the $A^2\Pi_{1/2}(v = 0,\ J = 1/2,\ +)$ hyperfine splitting $\delta_A \approx 18$ MHz.

$X^2\Sigma^+(v = 0,\ N = 1,\ J = 3/2,\ F = 1,\ -)$, are stronger, helping us identify this splitting. In contrast, if doing this spectroscopy with a linearly polarized laser, the $A^2\Pi_{1/2}(v' = 0,\ J' = 1/2,\ F' = 0,\ +) \leftarrow X^2\Sigma^+(v = 0,\ N = 1,\ J = 1/2,\ F = 1,\ -)$ transition does not exist and the $A^2\Pi_{1/2}(v' = 0,\ J' = 1/2,\ F' = 0,\ +) \leftarrow X^2\Sigma^+(v = 0,\ N = 1,\ J = 3/2,\ F = 1,\ -)$ transition is barely visible. Basic atomic physics knowledge like this turned out to be quite important.

7.2.2 MOT Force on the Molecular Beam

With the $A^2\Pi_{1/2}(v = 0,\ J = 1/2,\ +)$ splitting identified, if we look back to the old MOT laser frequency setpoints, they are all addressing the $A^2\Pi_{1/2}(v = 0,\ J = 1/2,\ F = 1,\ +)$ state. This can be problematic since MOT works around the $-\Gamma$ to -2Γ range, this detuning for the $A^2\Pi_{1/2}(v' = 0,\ J' = 1/2,\ F' = 1,\ +) \leftarrow X^2\Sigma^+(v = 0,\ N = 1,\ J = 3/2,\ F = 1,\ -)$ transition is actually $+2\Gamma$ to $+3\Gamma$ for the $A^2\Pi_{1/2}(v' = 0,\ J' = 1/2,\ F' = 0,\ +) \leftarrow X^2\Sigma^+(v = 0,\ N = 1,\ J = 3/2,\ F = 1,\ -)$ transition, causing a competing effect and canceling the MOT. For the ground ($J = 1/2$) states this is more tolerant since they do not provide much MOT force given the small g-factors and small number of states. So the ultimate configuration is, only the $X^2\Sigma^+(v = 0,\ N = 1,\ J = 3/2,\ F = 1,\ -)$ state is coupled to the $A^2\Pi_{1/2}(v = 0,\ J = 1/2,\ F = 0,\ +)$ state,

the other three ground hyperfine states are coupled to the $A^2\Pi_{1/2}(v = 0,\ J = 1/2,\ F = 1,\ +)$ state, as shown in Fig. 7.2(b). Once the lasers are set this way, we immediately observe a MOT compression force on the molecular beam, as shown in Fig. 7.4. In order to observe the MOT effect on the beam, the ($v = 0$) main cooling laser in slowing is turned on only for a millisecond, corresponding to the small and short time blue trace. Note that this does not need to be turned on at all, this happens to be the configuration when we run this experiment. The orange and green traces are from the MOT lasers' fluorescence on the beam in the MOT and antiMOT configurations. In the MOT configuration, the molecular beam is spatially compressed to the center, leading to a better collection efficiency in the imaging system and thus more photons are collected on the PMT. In other words, the effect we see here is a second-order effect. If detected on a camera, one would expect a spatial compression and a minimum change in the number of collected photons.

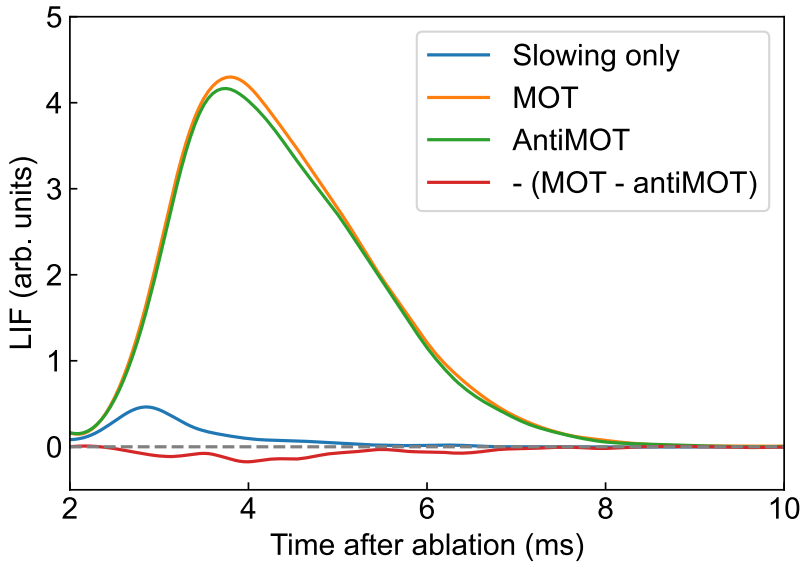

Figure 7.4: MOT compression on the molecular beam. The orange and green trace show the LIF of the MOT lasers in the MOT and antiMOT configurations. A change in LIF is observed, indicating a MOT compression force on the molecular beam.

We further optimized the MOT force using this "2D MOT" effect, including laser frequency scans of individual hyperfine states, relative phase of the Pockels cell and magnetic field gradient, so on and so forth, and found that our initial setpoints are around optimal (we did a good job!). Figure 7.5 shows the frequency response and the phase response of the MOT effect. The MOT

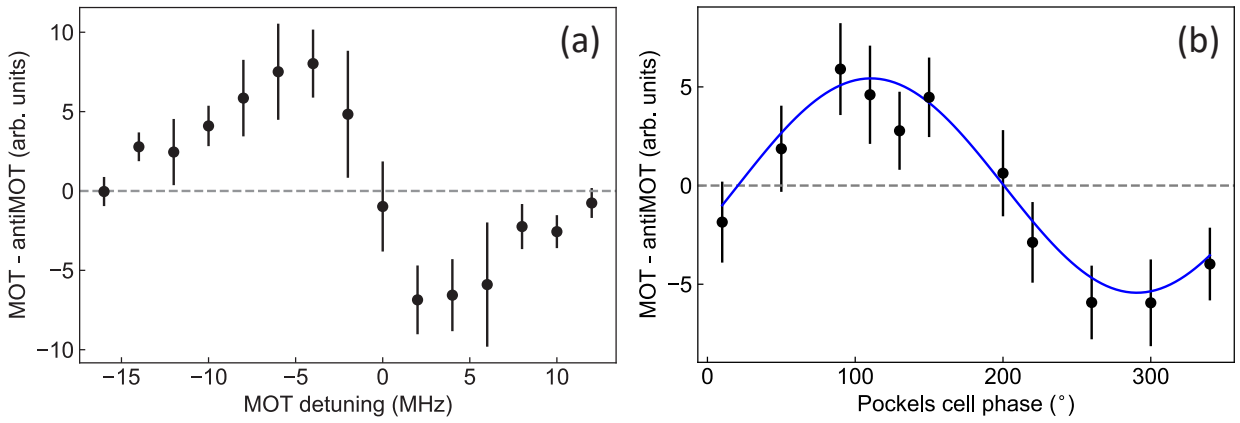

Figure 7.5: "2D MOT" effect as a function of (a) MOT laser detuning and (b) relative phase between the Pockels cell and the magnetic field gradient.

effect is found to be optimal with a global detuning $\delta \approx -5$ MHz, which is later found to be the same as in the 3D MOT. The absolute number of the phase is arbitrary since there is additional phase accumulation in between the cables, but the optimal setpoint of 110° is also exactly the same as what we expected, when we optimized by looking at the laser polarization with respect to the current flowed into the magnetic field coil using Hall probes.

7.3 3D MOT of CaH

With an efficient laser slowing, and a working MOT system, a 3D MOT of CaH immediately showed up. Here I summarize the final configuration of the 3D MOT. The CaH molecules are first chemically produced with a CBGB source. The hot Ca atoms ablated out by a pulsed Nd:YAG laser react with the H_2 molecules flowed in at ~1 SCCM to produce CaH molecules. The molecules are then buffer gas cooled by both H_2 and He buffer gas flowed in at ~0.9 SCCM and extracted from the cell to form the molecular beam. 1.2 ms after the ablation, counter-propagating slowing lasers are applied. The slowing lasers include a ($v = 0$) main cycling laser addressing the $A^2\Pi_{1/2}(v' = 0,\ J' = 1/2,\ +) \leftarrow X^2\Sigma^+(v = 0,\ N = 1,\ -)$ transition, a ($v = 1$) repump laser addressing the $B^2\Sigma^+(v' = 0,\ N' = 0,\ +) \leftarrow X^2\Sigma^+(v = 1,\ N = 1,\ -)$ transition, and a $A^2\Pi_{1/2}(v' = 1,\ J' = 1/2,\ +) \leftarrow X^2\Sigma^+(v = 2,\ N = 1,\ -)$ transition, with powers of 1.2, 0.9, and 0.3 W, respectively. The center frequencies of these slowing lasers are shown in Table 6.1. The ($v = 0$)

main cooling laser is frequency modulated with EOMs operating at 947.1 MHz (spin-rotation), 50.83 MHz (hyperfine), and 4.335 MHz (WL, together with the hyperfine EOM, broadens the laser to 402 MHz). The repump lasers are frequency modulated with EOMs operating at 942 MHz (spin-rotation), 53.5 MHz (hyperfine), and 4.185 MHz (WL, together with the hyperfine EOM, broadens the lasers to 424 MHz). The ($v = 0$) main cooling laser is kept on for 15 ms, while the repump lasers remain on to also serve as repumps for the MOT.

The MOT starts to load at ~15 ms after ablation when the main cooling laser in slowing is turned off. Figure 7.6 shows the 635 nm LIF from the $B^2\Sigma^+(v' = 0,\ N' = 0,\ +) \rightarrow X^2\Sigma^+(v = 0,\ N = 1,\ -)$ decay due to the ($v = 1$) repump laser detected on a PMT in three configurations: slowing only (gray), MOT (red), and antiMOT (blue). The fact that we are able to detect molecules long after the molecular beam flying by demonstrate a successful magneto-optical trapping. We image the MOT using an EMCCD camera, integrating from 25 to 55 ms after ablation for both the MOT and the antiMOT configurations, as shown in the insets of Fig. 7.6. The high contrast

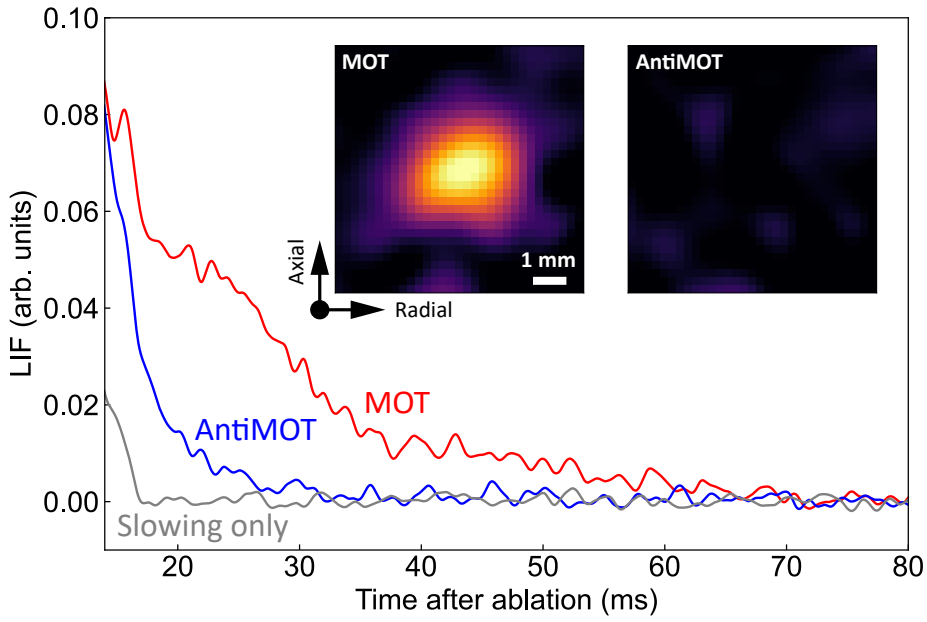

Figure 7.6: MOT LIF measured on PMT and EMCCD camera. The PMT data are taken in three configurations: slowing only (gray), MOT (red), and antiMOT (blue). The existence of molecules after the molecular beam flying by demonstrate a successful magneto-optical trapping. Insets show the camera images of the MOT and antiMOT, integrating from 25 to 55 ms after ablation. The images are smoothed with a Gaussian filter of 0.6 mm standard deviation.

between the two configurations further confirms the successful creation of a MOT. For Fig. 7.6, the MOT is loaded with 11 mW of MOT laser power per beam. After thermalizing for ~10 ms, at 25 ms after ablation, the MOT laser power is ramped down to 7.5 mW per beam over a 10 ms period. This is for extending the lifetime and also to reach a lower temperature of the MOT. The root-mean-square axial magnetic field gradient is kept at 17 G/cm.

7.3.1 MOT Lifetime and Predissociation

To determine the lifetime of the MOT, we subtract the LIF of the antiMOT configuration from that of the MOT configuration on the PMT, and fit the tail of the resulting time trace to an exponential decay, $1/e$ lifetime can be extracted from the exponential decay constant. An example is shown in Fig. 7.7(a). We measure the MOT $1/e$ lifetime at various MOT laser power and achieve

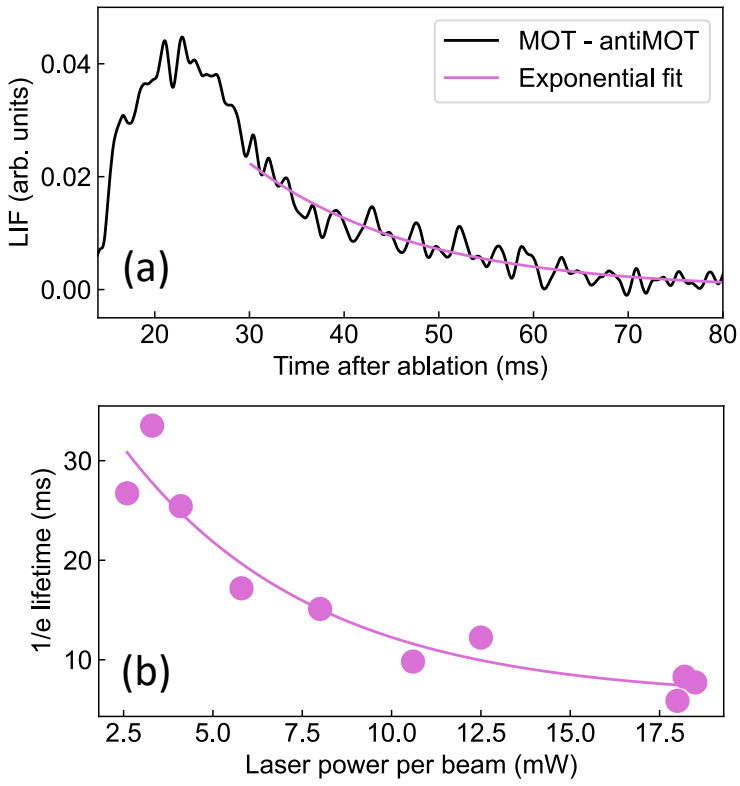

Figure 7.7: MOT lifetime measurement. (a) LIF of the antiMOT configuration subtracted from that of the MOT configuration. The tail of the resulting time trace can be fitted to an exponential day, from which $1/e$ MOT lifetime can be extracted. (b) $1/e$ MOT lifetime as a function of MOT laser power. Lifetime of ~30 ms is achieved with a few milliwatts of MOT laser power per beam.

lifetimes up to ~30 ms at a few milliwatts of power [Fig. 7.7(b)]. Longer lifetimes are possible but would require significantly more averages for comparable SNRs.

Photon scattering rate can be determined by switching off the ($v = 2$) repump laser and measure again the $1/e$ lifetime. With either a measured or theoretical value of VBR_{02}, the photon scattering rate can be extracted. With a photon scattering rate measurement, a calibration of the camera imaging system, and the total photoelectrons collected on the camera, we estimate a peak number of 230(40) molecules trapped in the MOT.

The photon scattering rate measurement also enables estimation of loss to either higher vibrational states or other forms of loss channels, for example predissociation. From the calculated FCFs in Table 5.1, loss to the ($v = 3$) state should be smaller than that from predissociation of the $B^2\Sigma^+(v = 0,\ N = 0,\ +)$ state used for ($v = 1$) repump. With a MOT lifetime of 15.1(2) ms and a photon scattering rate of $6.1(1.1) \times 10^5$ s^{-1} at 8 mW of MOT laser power per beam, the predissociation probability of the $B^2\Sigma^+(v = 0,\ N = 0,\ +)$ is estimated to be $3.7(7) \times 10^{-3}$. This number is higher than our previous measurement in beam but in better agreement with the calculated value. Nevertheless, this further limits our photon budget down to $\sim 7 \times 10^3$. Given the forward velocity of the CaH molecular beam, $\sim 10^4$ photons is required for laser slowing. Less than half of the total slowable population could survive this process, further limiting the number of molecules that could be trapped in the MOT.

7.3.2 MOT Characterization

To further characterize the MOT performance, we measure its properties including the MOT trapping and cooling force, as well as the size and temperature of the MOT. To measure the MOT trapping and cooling force, we apply a push by pulsing on the ($v = 0$) main cooling laser in slowing for 0.5 ms after the MOT has been thermalized (~25 ms after ablation, MOT laser power 11 mW per beam). In the low temperature regime, the MOT trapping and cooling force can be described as a damped harmonic oscillator $F = -\omega^2 r - \beta v$. Here ω and β are the trapping frequency and damping constant, respectively. Through observing the oscillation of the

molecules in the MOT resulting from the push, these constants can be extracted with the expression $r(t) \propto e^{-\beta t/2} \sin[\sqrt{\omega^2 - (\beta/2)^2}t]$. This is measured in Fig. 7.8. Each image in Fig. 7.8 is integrated for 2 ms on the camera, and a 2D Gaussian fit is used to determine the center position. Figures 7.8(ii)–7.8(v) show the MOT position 3.5, 9, 13, and 16 ms after the push, while Fig. 7.8(i) shows the unperturbed MOT position. From the fit, $\omega = 2\pi \times 48(3)$ Hz and $\beta = 510(110)$ s^{-1}. These numbers are comparable to the molecular MOTs with comparable masses, such as CaF [75] and CaOH [77].

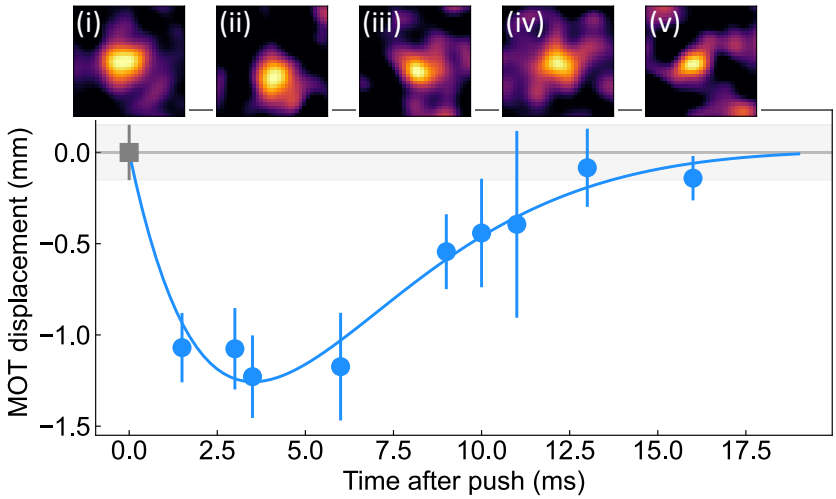

Figure 7.8: MOT trapping and cooling force measurement. The MOT is pushed by the slowing laser for 0.5 ms after thermalized. The resulting oscillation of MOT position is measured. (ii)–(v) are sample camera images of the MOT at 3.5, 9, 13, and 16 ms after the push, while (i) represents the unperturbed MOT position. The images are smoothed with a Gaussian filter of 0.6 mm standard deviation and normalized to the same scale for better visualization. Error bars represent 1-σ uncertainties. From the fit, $\omega = 2\pi \times 48(3)$ Hz and $\beta = 510(110)$ s^{-1}.

Furthermore, we characterize the MOT size and temperature. Figure 7.9 shows the geometric mean MOT size $\sigma_{\mathrm{MOT}} = \sigma_{\parallel}^{1/3}\sigma_{\perp}^{2/3}$ at different MOT laser powers. Here $\sigma_{\parallel}$ and $\sigma_{\perp}$ are the fitted Gaussian width in the axial and radial axis of the magnetic field gradient, respectively. With constant MOT laser powers, the MOT is imaged on the camera from 25 to 55 ms. An increase in the MOT size with laser power is observed, which is expected since with in the high power regime, sub-Doppler heating effect would dominate. We also measure the MOT temperature at two laser powers, 7.5 and 11 mW, as shown in the inset of Fig. 7.9. Temperature is measured

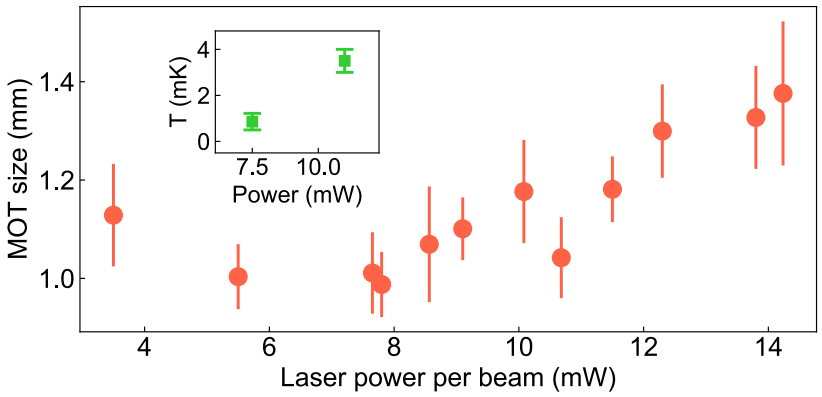

Figure 7.9: MOT size and temperature measurements. Geometric mean MOT size is measured as a function of MOT laser power. An increase in the MOT size at higher laser power due to a stronger sub-Doppler heating is observed. The temperature of the MOT is measured at two characteristic powers using the release-and-recapture method.

through release and recapture of the MOT. 25 ms after ablation when the MOT has thermalized, we release the MOT and wait for a variable amount of time. The spatial expansion during this time follows $\sigma(t) = \sqrt{\sigma^2(0) + (k_B T/m)t^2}$, so the temperature can be inferred. The geometric mean temperatures $T_{\mathrm{MOT}} = T_{\parallel}^{1/3} T_{\perp}^{2/3}$ for the 7.5 and 11 mW of MOT laser power per beam are determined to be 0.86(36) and 3.5(5) mK, respectively.

7.4 Further Cooling and Trapping

Up to this point, we have successfully demonstrated a 3D MOT of CaH molecules. The key to success in future experiments would be to increase the number of trapped molecules. During the search for the CaH MOT, there are a few aspects that we think might help but have not yet been implemented. I discuss these in this section as a guideline for potential future upgrades.

7.4.1 Improvements on Slowing

We can tell from the previous chapter that laser slowing is not optimal yet, with slowed population scaling linearly with the laser power. An immediate improvement is possible if we can have a higher laser power or a higher efficiency of power usage. The most lossy and fragile components in our slowing setup now are the free-space spin-rotation 1 GHz EOMs. As mentioned, they make

the slowing lasers' spatial mode non-Gaussian. Plus, since we are only using the ±1 orders of the sidebands, ~30% of the power is wasted. A neat solution to this will be using fiber EOMs. With the 695 nm SFG system, a fiber EOM with high bandwidth could be added in between the 1080 nm seed and amplifier for this purpose. Unfortunately, we did not have this option included for the first Precilasers SFG system we bought. For the next upgrade, we ordered a new SFG system from Precilasers that can deliver up to ~10 W of power at 695 nm with a built-in fiber EOM. With the new system, we would expect to saturate the effectiveness of WL laser slowing.

Furthermore, chirped laser slowing is known to perform better than WL slowing given the temporal dependence. It helps mitigate the overslowing issue for the lower velocity groups in the natural population. For chirped slowing, we would turn off the WL EOM to only address a specific velocity group, then chirp the frequency to be resonant with ~200 m/s velocities down to ~10 m/s in ~10 ms time scale. Detailed parameters need further exploration. Without the reduced intensity for each velocity group as in WL slowing, the current laser power might be enough. However, we are currently using the same laser for slowing and MOT, while an independent laser is needed for the MOT of we do chirped slowing. The new 695 nm laser system will serve as a stand-alone laser source for MOT in the first trial, and may be swapped with the slowing laser if more power is needed there.

For now, chirped laser slowing remains the most effective method for molecules. However, without the spatial dependence, it still does not work as well as Zeeman slowing as in atoms. Efforts on Zeeman slowing of molecules exist [170], but whether it can be generally practical remains a question mark. Alternatively, a push beam sent from the back of the buffer gas cell can further mitigate the overslowing issue. With the push beam resonant to the near zero velocity group, molecules that are slowed down to zero before reaching the MOT region can be pushed into the MOT, leading to a higher number of trappable molecules. Considering all aspects mentioned here, with higher power (assume a 2× improvement), chirped slowing (other experiments indicate at least a 2× improvement), and push beam, we expect at least a 5× overall improvement on the MOT number if everything is tuned to optimal. Moreover, 2D transverse cooling right after the cell

could also lead to a higher MOT number by producing a more collimated molecular beam. With these upgrades in the pipeline, a MOT with $\sim 10^3$ CaH molecules should be possible.

7.4.2 Blue-Detuned MOT and Optical Dipole Trapping

Although we can already start doing dissociation spectroscopy in the MOT, in order to trap the dissociated hydrogen atoms in an optical dipole trap (ODT), higher phase-space densities are still required. Pathways including sub-Doppler cooling [171, 172, 77] and blue-detuned MOT [173, 174, 175, 176, 177, 178] exist. It has been demonstrated that molecules can reach tens of μK temperature and tens of μm size with these techniques, which can lead to close to unity transfer to a shallow conservative trap such as an ODT. To implement these for CaH, we are going to use an AOM-based polarization switching setup for the rf MOT to replace the Pockels cell setup to be compatible with a dc blue-detuned MOT operation. Figure 7.10 shows a layout of the relevant optical path. The key benefits of this setup include high contrast polarization switching, good long-term stability, and minimal power loss. In this setup, the polarization of a certain hyperfine laser is switched by alternating between two optical paths with $\lambda/2$ phase difference controlled by

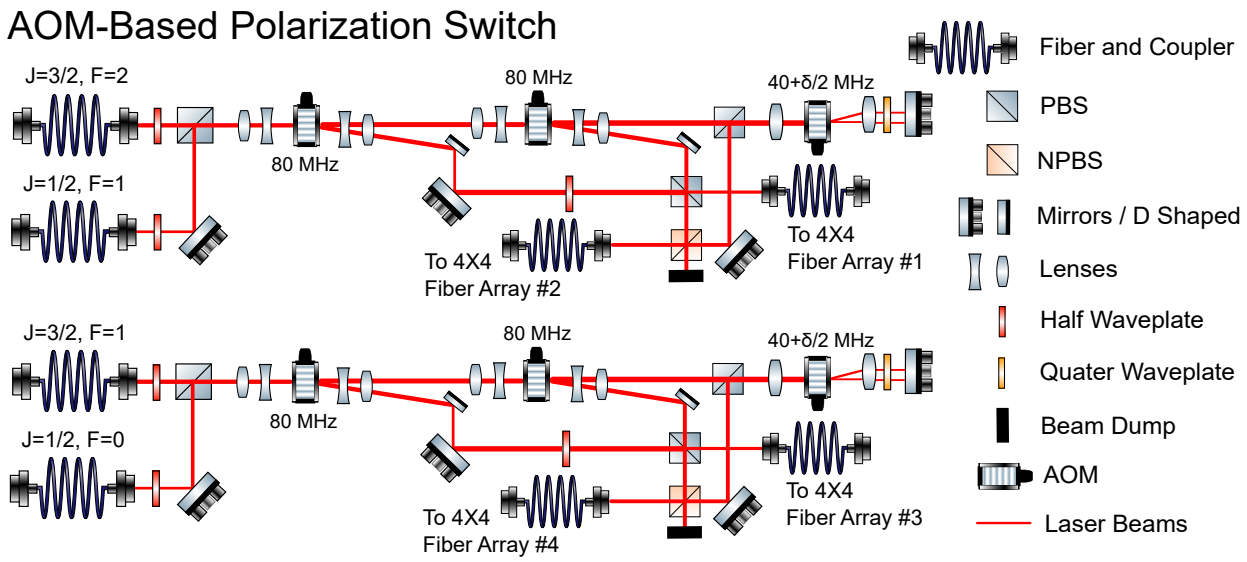

Figure 7.10: Schematic of the AOM-based polarization switching setup. With an appropriate AOM control sequence, the design shown here is compatible for both rf MOT and dc blue-detuned conveyor-belt MOT.

two AOMs. As a result, to couple four hyperfine states at the same time, 4-by-4 fiber arrays are needed. Three of the outputs are used for the three MOT arms, and the remaining one could be used as a monitor. This configuration bypasses the need to combining four hyperfine lasers through non-polarizing beam splitters (NPBSs) to send to the Pockels cell, thus does not have additional power loss during this process. Following the suggestions from the CaOH and CaF team in the Doyle group, we purchased the fiber array from Evanescent Optics Inc., where they guarantee PM for both vertical and horizontal axes over all inputs and outputs. At the time this thesis is written, the team has tested it with the rf MOT, the extension to the dc blue-detuned conveyor-belt MOT is still work in progress. With these implemented, an ODT with several hundred up to a thousand CaH molecules should be possible.

7.4.3 To Improve the Overall Yield

For any scientific purposes, the higher the molecule or atom number the better. During the exploration, there is evidence showing that we are not fundamentally limited to the thousand molecule level we just described, further improvements are possible with further investigations.

Compared to atoms, the first and maybe the most important limitation for molecules is the lower flux, and CaH has an even lower flux compared to other molecules. The reason CaH is performing sub-optimally comes from several aspects. First, the reaction to produce CaH molecules is highly endothermic. One might notice that the reactions to produce hydroxide molecules are also endothermic, however, they can be made exothermic if promoting the metal (Ca, Sr, or Yb) to the metastable $^3P_1$ state through laser excitation [179]. Unfortunately, the same technique does not work for CaH, where we tried exciting Ca to the $4s4p\ ^3P_1$ state. To make sure we are not doing anything wrong, we tried enhancing Ca + $H_2O \rightarrow$ CaOH production in our own cell, and it worked exactly as in other experiments. The main reason for this is that the excited state energy is still not enough to break the H_2 bond and there are no additional exothermic pathways due to the simple structure. Promoting Ca to states with higher energies is a possible solution to this. We have experimentally identified the Ca $4s12s\ ^1S_0 \leftarrow 4s4p\ ^1P_1$ transition, the energy of the Rydberg state

should make the reaction exothermic. We have not observed any enhancement with this, but in part could be from the low laser power available in our laboratory now in this wavelength (~408 nm). It is worth trying another time once we have more laser power. Moreover, the reaction may also be enhanced with vibrational excitation of H_2 molecules. The reaction network model required to describe the observed CaH yield in the Ca + H_2 → CaH reaction shown in Chapter 3 indicates the important role of higher vibrational states of H_2. Enhancing the reaction with laser excitation of H_2 [180] is possible.

Another limitation of CaH comes from its small binding energy (and the reaction is still highly endothermic even with this small binding energy). This causes the predissociation problem as mentioned in Chapter 5. A way to bypass this problem is to use the A state for ($v = 1$) repump. However, as one can tell, this will limit the overall photon scattering rate and thus lead to a weaker slowing force, which will also result in a low number of trappable molecules in the MOT. But we do not know yet whether this will work better or worse than repumping ($v = 1$) using the B state without trying. Moreover, with a good 2D transverse cooling, repumping through the A state might ultimately work better with a longer slowing distance.

Further improvement is possible with a colder cryogenic system, which could lead to a higher overall molecule production and a lower forward velocity. The problem is still the large rotational constant of CaH that makes the ($N = 1$) population peak at ~10 K. If with a ~3 K cell as other molecule experiments, most of the CaH molecules produced will reside the ($N = 0$) state. A population transfer scheme with $A^2\Pi_{1/2}(v' = 0,\ J' = 1/2,\ -) \leftarrow X^2\Sigma^+(v = 0,\ N = 0,\ +)$ laser excitation and $A^2\Pi_{1/2}(v' = 0,\ J' = 1/2,\ +) \leftarrow A^2\Pi_{1/2}(v = 0,\ J = 1/2,\ -)$ microwave mixing is possible. Integrating the ~26 GHz microwave with the cryogenic system posses some engineering challenge but is not impossible. The colder cryogenic system and population transfer should give us the best signal in the end.

Chapter 8: Extension to the Fermionic Isotopologue CaD

When we were trying to think of new ideas for the experiment, we realized that, if we can laser cool and trap CaH molecules and get ultracold hydrogen atoms, what about deuterium atoms, or even tritium atoms. Starting as a side project, it actually brought us nice surprises. Now with the successful demonstration of a CaH 3D MOT, we think a CaD 3D MOT may not be far away. In this chapter, I describe the first laser cooling of the fermionic CaD molecules, which paves the way toward ultracold deuterium for precision spectroscopy.

8.1 Why CaD

Fermionic molecules possess many favorable properties for quantum science applications. Being less prone to collisional loss than their bosonic counterparts due to the p-wave barrier [22], fermionic molecules are an important ingredient in ultracold chemistry experiments. The combination of Fermi-Dirac statistics and long-range interactions of polar molecules can enable the realization of topological superfluid phases [181] and lattice-spin models [28]. A fermionic cycling center M can be employed for precision measurements of nuclear-spin-dependent parity violation (NSD-PV) [182, 183] and axionlike dark matter searches [2]. This has motivated recent studies with fermionic ^{137}BaF [184] and ^{171,173}YbOH [185], with the demonstration of rotational closure for the latter. Compared to the hyperfine complexity that plagues the molecules listed above, CaD turns out to be the easiest fermionic molecule to laser cool in the near term.

Cold CaH and CaD isotopologues have astrophysical significance as they have been observed in stellar and interstellar media [186, 187, 188]. Studying their ultracold chemical reactions in the laboratory would improve our understanding of fundamental chemical processes [26]. Moreover, CaD is a promising precursor for producing ultracold atomic deuterium, in analogy to the pro-

posals for CaH dissociation [99, 97]. High-precision measurements with hydrogen and deuterium allow testing quantum electrodynamics [189], determining fundamental constants such as the proton charge radius [92, 190], and probing new physical forces and particles [191]. In addition, a degenerate Fermi gas of ultracold deuterium atoms would enable a new paradigm in quantum simulation with the simplest Fermi liquid [192]. Even without dissociation, the fermionic nature of CaD could allow it to reach lower temperatures and achieve better shielding from collisional losses in a conservative trap, creating a promising playground for quantum simulation experiments. The existence of an electron spin in the ground state of CaD provides an additional degree of freedom compared to bialkali molecules. The relative simplicity and extensive applications make CaD an interesting laser-cooling candidate. Here, we demonstrate the production and 1D laser cooling of CaD, which, to our knowledge, is the first fermionic molecule to have been directly cooled.

8.2 Synthesis of CaD_2

When this experiment was carried out, we did not have the chemical production approach. As a result, production of a CaD molecular beam relies on ablation of CaD_2 samples. However, although some deuterated compounds are commercially available, CaD_2 is not. We produce the molecules by following a procedure for CaH_2 outlined in Ref. [193]. We build a high pressure, high temperature reactor using readily available components [Fig. 8.1(a)]. The body of the reactor is composed of a standard CF 2.75" stainless steel nipple. The bottom of the nipple is blanked off using a nickel gasket and constitutes the main reaction area wrapped with an electrical heating coil and a thermocouple connected to a temperature controller. The top is a CF to $1/4$" VCR adapter and the subsequent connections are all made with standard stainless steel VCR connectors. Such connections are rated for pressures $>5,000$ psi and temperatures >500 °C. However, CF flanges are only rated for pressures below atmospheric pressure and temperatures up to 450 °C.

Once assembled, we stress test the reactor using inert helium gas. We confirm that the system is leak-tight first at atmospheric pressure and 450 °C, then up to 80 psi at room temperature, and finally up to 80 psi at 450 °C. With no leaks appearing at any point during these tests, we deem our

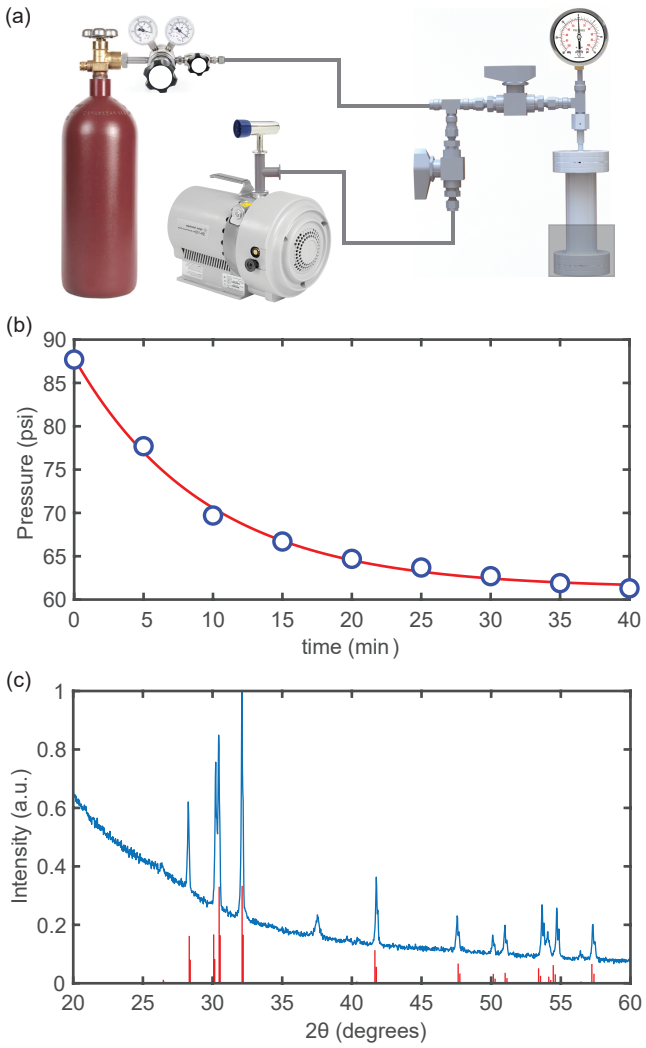

Figure 8.1: Synthesis of CaD_2. (a) Illustration of the home-built setup used for the synthesis. The main reactor is a standard CF 2.75", 5" long 304 stainless steel nipple. The base is wrapped with heating tape connected to a variac via a temperature controller (Extech 48VFL). A standard J-type thermocouple attached to the base is used for temperature stabilization. A high-pressure gauge (MG1-100-A-9V-R) is placed close to the top of the reactor. All connections henceforth are VCR type. The reactor connects to a scroll pump and a Convectron gauge (MKS 275) via a tee. The other end of the tee connects to a D_2 cylinder using a long flexible hose. The regulator on the cylinder allows for control of the charging pressure, while the valves shown are used to direct the flow. (b) Pressure measured on the high-pressure gauge as a function of time at 450 °C. The reactor contains 3 g of Ca pieces. From an exponential fit, we obtain a reaction rate of $k = 0.11$ min^{-1}. (c) Powder x-ray diffraction study of the resulting sample. Red lines are the known CaD_2 peaks. Almost all measured peaks match with the known CaD_2 values except for the peak at $2\theta = 37°$. This peak could be attributed to CaO or $Ca(OH)_2$, possibly resulting from short contact with air. The results suggest very high conversion efficiency from Ca to CaD_2.

reactor safe for operation with deuterium gas. We use Ca pieces of >99% purity from Millipore Sigma (327387-25G) and 99.8% pure deuterium gas from Cambridge Isotope Labs (DLM-408-100).

We charge our reactor with 3 g of Ca metal pieces measuring a few millimeters in size. Powderizing the Ca target is expected to improve reaction yield due to larger surface area but this is avoided since it would require pressing to form a target. The reactor is charged and sealed in an inert nitrogen environment to avoid contamination. Then we gradually heat the sample under vacuum to 450 °C over 2 hours. Care is taken to avoid large thermal gradients in the system that could lead to a formation of leaks. Since Ca melts at 840 °C, this temperature only enhances the rate of deuterating the Ca pieces. We then charge the hot reactor instantly with D_2 gas to 88 psi. With the D_2 reservoir valved off, the pressure in the reactor starts decreasing immediately, signaling that the reaction is underway. The pressure decreases to 62 psi after 40 min and the rate of change stagnates. This implies that the first phase of the reaction, surface deuteration, is complete [Fig. 8.1(b)]. The measured reaction rate is $k = 0.11$ min^{-1}. We leave the reactor charged and hot overnight, and after 9 hours the pressure decreases to ~50 psi. During this time, D_2 molecules diffuse through the Ca surface and penetrate into the bulk.

Once the system has cooled down to room temperature, we open the reactor in a nitrogen environment. Since the temperature is not high enough to melt Ca, the pieces do not change their shape or size. However, they turn from a dark silvery gray to a light powdery gray. We perform a powder x-ray diffraction (PXRD) analysis of the sample and find that it predominantly consists of CaD_2 [Fig. 8.1(c)]. This confirms our assumption that D_2 molecules can easily diffuse through the metal surface and cause deuteration in the bulk of the Ca pieces with high efficiency.

8.3 1D Cooling with MOT Chamber as Beamline

Figure 8.2(a) illustrates the experimental setup. The experiment starts with a CBGB source of CaD molecules, generated through a pulsed Nd:YAG laser ablation on the CaD_2 target we produced and buffer gas cooling with He flowed into the cell. The extracted molecular beam

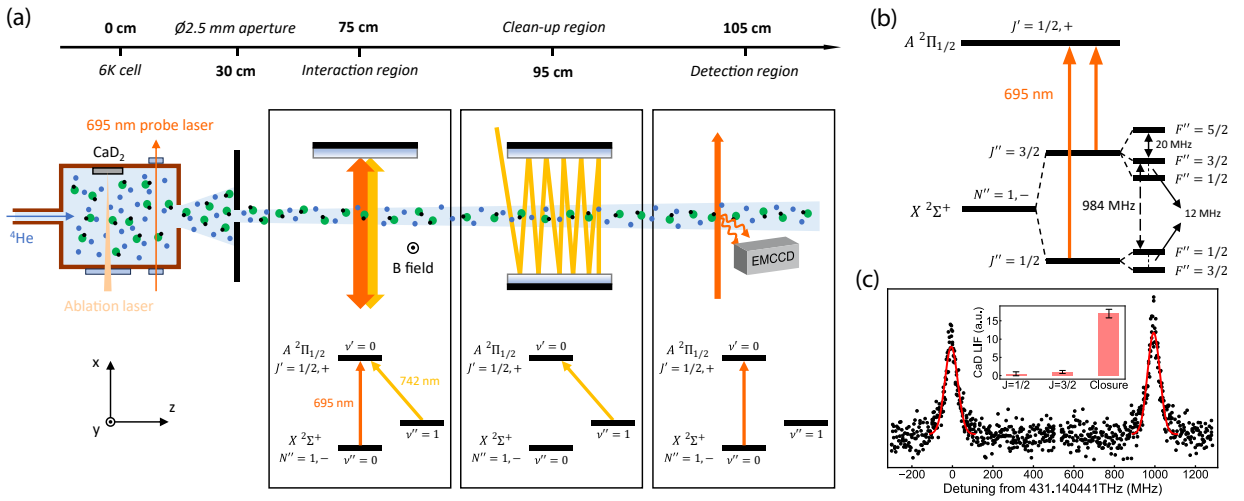

Figure 8.2: (a) Schematic of the experiment viewed from above. CaD molecules are generated in a ∼6 K CBGB source. The molecular beam is collimated by a 2.5 mm diameter aperture and enters the interaction region where it is addressed by the main cooling laser, copropagating with the ($v = 1$) repump laser. The laser beam is expanded to (10.8 mm × 5.4 mm) $1/e^2$ diameter and retroreflected to form a standing wave. The molecules then enter the clean-up region where only the ($v = 1$) repump laser is applied in a multipass configuration and are finally detected in the ($v = 0$) state. (b) Level structure of the main cycling transition $A^2\Pi_{1/2}(v' = 0,\ J' = 1/2,\ +) \leftarrow X^2\Sigma^+(v'' = 0,\ N'' = 1,\ -)$. The hyperfine splittings are adapted from Ref. [186]. (c) In-beam spectroscopy of the transition. The inset shows signal enhancement with rotational closure.

are collimated with a 2.5 mm diameter aperture to 16(1) mK transverse temperature (estimated with MC simulations as in Sec. 8.4.2) before entering the interaction region where we perform laser cooling. The molecules then enter the clean-up region and are detected through LIF with an EMCCD camera. During this experiment, our ultrahigh-vacuum chamber is already set up in a 3D rf MOT configuration, with the MOT chamber here serving as the interaction region. We apply magnetic field using the in-vacuum MOT coils in the Helmholtz configuration. Compared to CaH, we find an overall ∼5× higher yield under a full range of experimental parameters such as helium flow rate, ablation laser energy, and ablation laser-beam waist. This may be attributed to differences in crystalline chemistry between the species.

Figure 8.2(b) shows the level structure of the main cycling transition $A^2\Pi_{1/2}(v' = 0,\ J' = 1/2,\ +) \leftarrow X^2\Sigma^+(v'' = 0,\ N'' = 1,\ -)$ used for laser cooling. We are able to locate the transition in Fig. 8.2(c) within ∼200 MHz of available spectroscopic data [187, 188]. The hyperfine splittings

of the $J = 1/2$ and $J = 3/2$ states are adapted from Ref. [186], which we are unable to resolve due to Doppler broadening of the beam. This is of particular advantage compared to CaH where the spacings are ~50–100 MHz [66]. We show our ability to rotationally close the transition by adding the two spin-rotation components $J = 1/2$ and $J = 3/2$ in the inset of Fig. 8.2(c). The LIF is normalized to that of $J = 3/2$ only and we observe a ~15× higher fluorescence when both components are present. This also confirms that the $A^2\Pi_{1/2}(v' = 0,\ J' = 1/2,\ +)$ excited-state hyperfine levels are unresolved.

Again, a key requirement to directly laser cool a molecule is the ability to continuously scatter photons at a relatively fast rate (~10^6 s^{-1}). The VBRs of the molecule should be diagonal so that a practical number of lasers can mitigate loss to higher vibrational states. The VBRs for CaD have been calculated [188] and are shown in Table 8.1. Since the electronic potential energy surface does not depend on the mass of the nuclei, we do not expect large isotope shifts in the VBRs. However, the mass change leads to a significant shift of fundamental vibrational frequencies, from 37 THz in CaH to 27 THz in CaD. Overall, we assume the VBRs for CaD to be the same as our measured VBRs for CaH in order to calculate the number of scattered photons.

We perform laser cooling on the $A^2\Pi_{1/2}(v' = 0,\ J' = 1/2,\ +) \leftarrow X^2\Sigma^+(v'' = 0,\ N'' = 1,\ -)$ transition, together with a $(v = 1)$ repump laser addressing the $A^2\Pi_{1/2}(v' = 0,\ J' = 1/2,\ +) \leftarrow$

Table 8.1: Measured CaH VBRs and calculated CaH and CaD VBRs [188]. The calculated VBRs for CaH are in good agreement with our own calculations in Chapter 5 and Ref. [97].

Transition	Vibrational Quanta (v'')	CaH VBR Measured ($q_{0v''}$)	CaH VBR Calculated ($q_{0v''}$)	CaD VBR Calculated ($q_{0v''}$)
$A \rightarrow X$	0	0.9680(29)	0.9820	0.9758
	1	0.0296(24)	0.0175	0.0235
	2	$2.4(1.8)\times10^{-3}$	4.61×10^{-4}	7.18×10^{-4}
	3	–	2.0×10^{-5}	3.2×10^{-5}
$B \rightarrow X$	0	0.9853(11)	0.9790	0.9688
	1	0.0135(11)	0.0202	0.0295
	2	$1.2(0.2)\times10^{-3}$	7.5×10^{-4}	1.5×10^{-3}
	3	–	6.7×10^{-5}	1.5×10^{-4}

$X^2\Sigma^+(v''=1,\ N''=1,\ -)$ transition. This allows us to scatter around $\sum_{v''=0}^{1} 1/(1-\mathrm{VBR}_{0v''}) \approx$ 400 photons before populating higher vibrational states. The frequencies of the lasers used are presented in Table 8.2. The spectroscopy of the $A^2\Pi_{1/2}(v'=0,\ J'=1/2,\ +) \leftarrow X^2\Sigma^+(v''=0,\ N''=1,\ -)$ main cycling transition is done in a quasirotationally-closed configuration. We scan the frequency of one spin-rotation component while holding the other on resonance. This provides higher SNR because of the enhancement in LIF due to optical cycling. With the hyperfine levels unresolved [Fig. 8.2(c)], we fit the spectra to Gaussians with fixed spacing and relative amplitude, according to the hyperfine splittings obtained from Ref. [186] and state degeneracies. However, there are no previously measured hyperfine splittings for the $X^2\Sigma^+(v''=1,\ N''=1,\ -)$ state. We instead fit the $(v=1)$ repump transition with a single Gaussian for each spin-rotation component. All the frequencies are measured using a HighFinesse WS7-60 wavemeter. In order to generate the sidebands for the ground-state spin-rotation and hyperfine splittings of the main cycling transition, we use two EOMs operating at 980 MHz and 11 MHz in series. Specifically, we use the −1st and 0th order of the 980 MHz EOM for the $(J=3/2)$ and $(J=1/2)$ spin-rotation components, respectively, and the 0th, ±1st, ±2nd orders of the 11 MHz EOM for the hyperfine levels. We note that the +1st order of the 980 MHz EOM is unused in the cooling experiment because it is far-off resonant, resulting in a ∼30% decrease in the effective laser intensity. For the $(v=1)$ repump, we use a 978 MHz EOM and a high-Q 4.185 MHz EOM. The 4.185 MHz EOM generates an array of sidebands (±5 orders) to cover the hyperfine levels in the $(v=1)$ manifold.

Table 8.2: CaD transition frequencies. The uncertainties are ∼10 MHz statistical and ∼60 MHz systematic from the wavemeter.

Ground	v''	N''	J''	F''	Excited	v'	N'	J'	Frequency (THz)
X	0	1	3/2	5/2	A	0	–	1/2	431.140421
				3/2					431.140441
				1/2					431.140453
			1/2	3/2					431.141437
				1/2					431.141425
X	1	1	3/2	5/2, 3/2, 1/2	A	0	–	1/2	403.852444
			1/2	3/2, 1/2					403.853423

The main cooling laser and the repump laser are combined with a polarizing beam splitter (PBS) and coupled to a single-mode polarization-maintaining optical fiber. They are expanded to $(2w_1 \times 2w_2) = (10.8\ \text{mm} \times 5.4\ \text{mm})\ 1/e^2$ diameter and retroreflected in the interaction region to form a standing wave. The polarization of the main cooling laser ($v = 0$) is set to 45° with respect to the applied magnetic field along the y axis for efficient dark-state remixing. In the clean-up region, only the ($v = 1$) repump laser is applied in a multipass configuration. Finally we detect the molecules that remain in the ($v = 0$) state using the main cycling transition. The total power of the lasers shown in the schematic are 475, 180, 180, and 45 mW, corresponding to the main cooling laser, ($v = 1$) repump laser in the interaction region, ($v = 1$) repump laser in the clean-up region, and the detection laser, respectively.

8.4 Magnetically Assisted Sisyphus Cooling of CaD

Figures 8.3(a)–8.3(c) show the molecular-beam profile detected on the EMCCD camera, with a magnetic field $|\vec{B}| = 1.7$ G applied along the y axis in the interaction region. The image in Fig. 8.3(a) is taken when the main cooling laser is absent, representing the unperturbed molecular-beam profile in the ($v = 0,\ 1$) states. The fluorescence along the x axis indicates the size of the molecular beam in the detection region, while the z-axis width is determined by the detection laser beam. In Fig. 8.3(b) the main cooling laser is applied at +40 MHz detuning from resonance and we observe an accumulation of molecules near the center of the beam due to Sisyphus cooling. In Fig. 8.3(c) the laser is detuned by −40 MHz and we observe an expulsion of molecules from the center due to Sisyphus heating. We integrate the images along the z axis and obtain the 1D profile shown in Fig. 8.3(d). We note that because of the limited interaction time of $\sim 40\ \mu$s, we only deplete the population to 93(3)% even when the main cooling laser is set on resonance. This corresponds to 30(13) photons scattered at a rate of $0.7(3)\times10^6\ \text{s}^{-1}$. This number further decreases in Sisyphus cooling and heating configurations due to the laser detuning. With the limited number of scattered photons, the integrated LIF signals under Sisyphus cooling and heating configurations are essentially unchanged from an unperturbed beam, as in Fig. 8.3(d). We note that the estimated

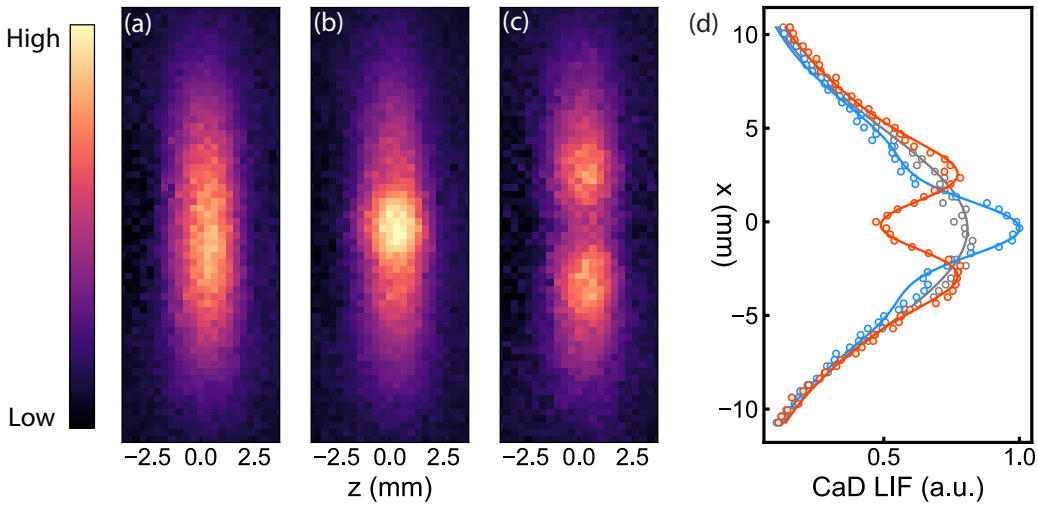

Figure 8.3: Molecular-beam profile with Sisyphus cooling and heating. (a)–(c) Beam images under unperturbed, Sisyphus cooling at +40 MHz, and Sisyphus heating at −40 MHz configurations, respectively. (d) Integrated 1D profile. Sisyphus cooling narrows the width of the center of the molecular beam (blue), while Sisyphus heating expels molecules away from the center (red). Unperturbed beam is shown as gray. Solid lines show the fits to the beam profile.

scattering rate is roughly half of the maximum scattering rate due to the fact that both ($v = 0$) and ($v = 1$) lasers address the same excited state $A^2\Pi_{1/2}(v' = 0,\ J' = 1/2,\ +)$.

We fit the 1D profile with a phenomenological model capable of describing both Sisyphus cooling and heating. The model combines a Gaussian and a second derivative of a Gaussian, the latter serving as a modulation of the amplitude. The function is given by

$$f(x) = A \times g_{x_0,\sigma_0}(x) \times (1 - \Delta h \times g''_{x_0,\sigma_S}(x)), \tag{8.1}$$

where $g_{x_0,\sigma_0}(x) = \exp(-(x - x_0)^2/(2\sigma_0^2))$ and $g''_{x_0,\sigma_S}(x) = ((x - x_0)^2/\sigma_S^2 - 1) \times \exp(-(x - x_0)^2/(2\sigma_S^2))$. The parameters A, x_0, and σ_0 represent the amplitude, center position, and width of an unperturbed beam, while Δh and σ_S represent the fractional peak height change and the width of the region where Sisyphus cooling or heating is effective. The shape of the second derivative of a Gaussian qualitatively reproduces how Sisyphus cooling or heating affects the central part of the molecular beam. The fits are shown as solid lines in Fig. 8.3(d).

The characteristic feature of the Sisyphus effect arises from the finite capture velocity v_c of the

Sisyphus force. In the Sisyphus cooling configuration, only molecules with $v < v_c$ can experience the Sisyphus force and get cooled. The Sisyphus cooled molecules reach a transverse temperature of 2.7(2) mK. In the Sisyphus heating configuration, on the contrary, slower molecules are heated and pushed away from the center. From the position of the two peaks in the Sisyphus heating profile, we determine a capture velocity of ~1 m/s.

8.4.1 Characterization of the Sisyphus Effect

We characterize the Sisyphus effect for the following experimental parameters: laser detuning, intensity, and magnetic field. The Sisyphus effect as a function of laser detuning is shown in Fig. 8.4(a), taken at $|\vec{B}| = 1.7$ G. Here we use peak height change Δh in Eq. (8.1) as a proxy for the strength, its sign representing cooling (positive) or heating (negative). The Sisyphus effect is antisymmetric around zero detuning, and the optimal detuning for cooling and heating are found to be at ~±40 MHz, respectively, which corresponds to ~±10Γ. Here $\Gamma \approx (2\pi) \times 3.8$ MHz represents the natural linewidth of the main cycling transition and is estimated from Ref. [188]. The relatively large optimal detunings primarily result from the small hyperfine splittings, since

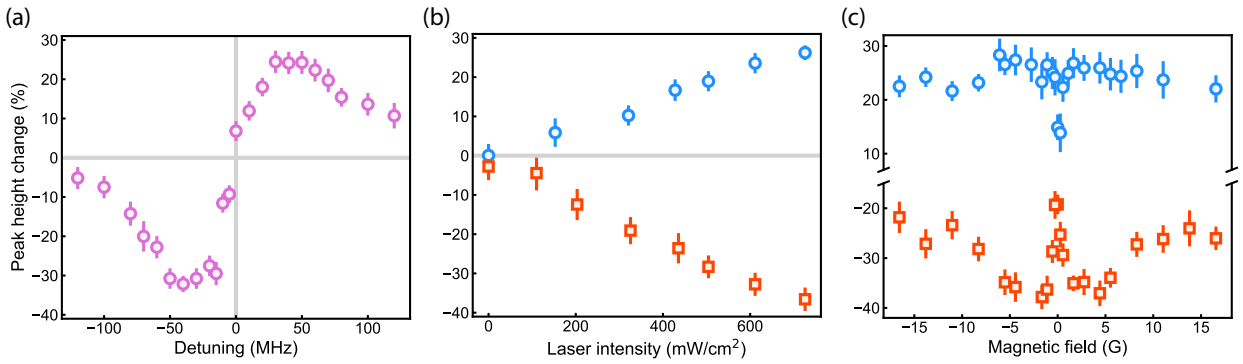

Figure 8.4: Parameter scans of the Sisyphus effect. (a) Peak height change as a function of the main laser detuning, taken with magnetic field $|\vec{B}| = 1.7$ G and at 45° with respect to laser polarization. (b) Sisyphus cooling (blue circles) and heating (red squares) as a function of the main laser intensity, taken at ±40 MHz detuning and the same magnetic field configuration as in (a). Saturation is not observed. The gray lines are guides to the eye for the unperturbed scenario (horizontal) and zero detuning [vertical in (a)]. (c) Sisyphus cooling (blue circles) and heating (red squares) as a function of applied magnetic field, taken at ±40 MHz detuning and maximum laser intensity. A sharp decrease in the strength of Sisyphus effect is observed when $|\vec{B}| \approx 0$. Error bars represent the 95% confidence intervals.

at small detunings all the sidebands introduced to address the hyperfine structure of the ground state compete with each other. Figure 8.4(b) shows the laser-intensity dependence of Sisyphus cooling (blue circles) and heating (red squares). Laser intensity here is defined as the mean intensity of the Gaussian beam in a $1/e^2$-diameter area ($P_{\text{tot}}/\pi w_1 w_2$), with only the effective laser sidebands accounted. We are not able to saturate the Sisyphus effect primarily due to the limited interaction time, and the scattering rate increases linearly with laser intensity in this regime. Figure 8.4(c) shows the magnetic-field response of the Sisyphus effect, taken at maximum laser intensity and ±40 MHz detuning for cooling (blue circles) and heating (red squares). We observe a sharp decrease of strength in both cooling and heating at $|\vec{B}| \approx 0$, when dark-state remixing is the least efficient. At higher magnetic fields, Sisyphus effect is again suppressed due to large Zeeman shifts. We also note that the Sisyphus effect cannot be completely eliminated by tuning the magnetic field in the standing-wave configuration for two reasons. First, the magnetic field cannot be perfectly canceled throughout the entire interaction region due to the presence of the Earth's magnetic field. Second, polarization gradient cooling could occur due to imperfect linear polarizations.

8.4.2 Beam Temperature Estimation

The transverse temperature of the molecular beam is estimated using MC beam propagation. We generate a uniform spatial distribution of 10^5 particles at the location of the aperture with a Boltzmann-distributed forward velocity of 250 m/s with 40 m/s as standard deviation and a transverse velocity $v_\perp$. We vary $v_\perp$ and calculate the molecular-beam width at the position of the detector. Matching this value to our measured unperturbed beam width ($\sigma \approx 5.4$ mm) gives us an estimate of $T_\perp \approx 16(1)$ mK. Next, we perform the same computation but now compare the calculated beam width to the measured width of the central peak of the Sisyphus cooled profile [Fig. 8.3(d)], $\sigma \approx 2.3$ mm. This provides a rough estimate of the Sisyphus-cooled beam temperature of 2.7(2) mK. We note that this temperature estimate is approximate and only serves as an indicator of cooling efficiency.

8.5 Doppler Cooling of CaD

In addition to sub-Doppler Sisyphus cooling, we also perform 1D Doppler cooling of the CaD molecular beam. The measured Doppler cooling and heating curve as a function of laser detuning is shown in Fig. 8.5. Because of the large capture velocity of the Doppler force, cooling and heating manifest as a change in Gaussian width ($\Delta\sigma$) of the molecular beam. We can switch from a Sisyphus to a Doppler configuration by multipassing the interaction laser and ensuring little overlap between neighboring passes.

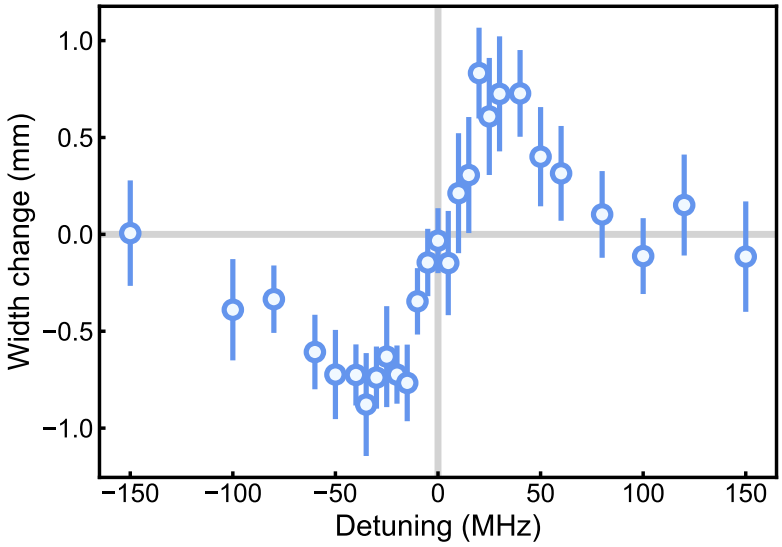

Figure 8.5: Doppler cooling and heating as a function of laser detuning, A change in the molecular-beam width demonstrates Doppler cooling (negative) and heating (positive). Error bars represent the 95% confidence intervals.

Chapter 9: Conclusion and Outlook

To summarize this thesis, we have extended the technique of laser cooling and trapping to a new class of molecules, diatomic metal hydrides. The specific molecule we work with is calcium monohydride, CaH. We have demonstrated 1D laser cooling on the molecular beam. We have also characterized the additional predissociative loss channel with relevance to laser cooling, according to which, we have designed a laser cooling scheme that possesses a high enough photon budget that could facilitate laser slowing and MOT. In the pursuit of the MOT, we upgraded our CBGB source and observed an unexpected endothermic CaH production in this regime for the first time. With careful and thorough investigation, we were able to achieve efficient laser slowing with molecules down to near zero velocities. With every difficulty tackled, small or big, we successfully created a 3D MOT of CaH molecules. We also show that the same technique can be extended to its fermionic isotopologue, CaD. Laser cooling of the fermionic CaD was demonstrated for the first time.

Looking forward, there is no doubt but hope and opportunities. With CaH molecules cooled and trapped at ultracold temperatures, a pathway toward ultracold trapped hydrogen is cleared. The predissociation hurts us in laser cooling, but once we cross the laser cooling phase, which we have, it can in turn facilitate controlled photodissociation. On this front, we calculated the line strengths of between different vibrational states between the ground X state and excited A and B states, as shown in Fig. 9.1. The B state is clearly less diagonal as compared to the A state. An efficient two-photon vibrational excitation (up-leg at 512.7 nm and down-leg at 1744.7 nm) is identified. With the predissociative nature of the B state, direct dissociation with a two-photon process is possible. An ultracold and trapped sample of atomic hydrogen for precision spectroscopy should be achievable in the next few years. On the other hand, as a new class of molecules to be trapped at ultracold temperatures, new opportunities open up for ultracold quantum chemistry. Because of hydrogen, CaH is one of the first molecules that could be treated fully quantum mechanically

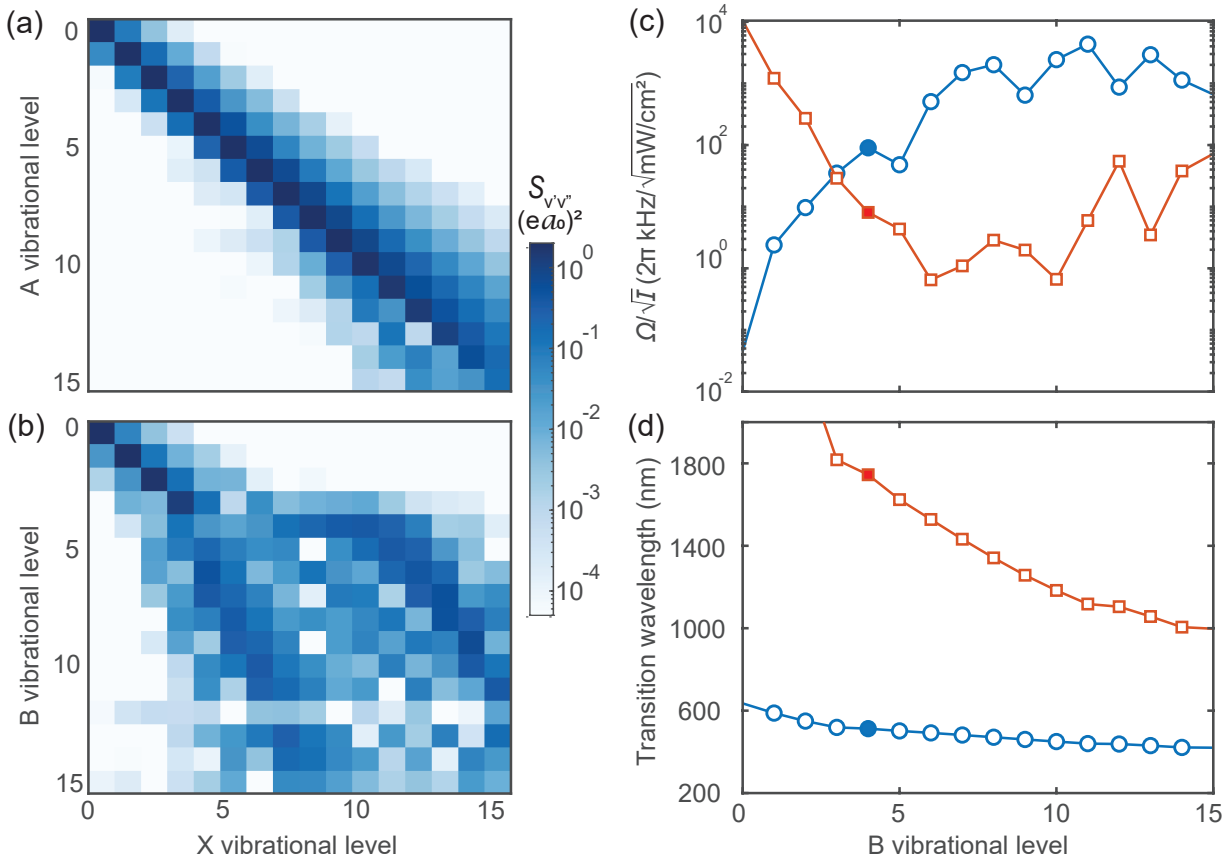

Figure 9.1: Suggested controlled dissociation pathway for CaH molecules. Line strengths ($S_{v'v''}$) in atomic units for dipole allowed transitions: (a) $X^2\Sigma^+$ (v'') $\rightarrow A^2\Pi_{1/2}$ (v') and (b) $X^2\Sigma^+$ (v'') $\rightarrow B^2\Sigma^+$ (v'). The A state potential is more harmonic as is reflected by the diagonal $S_{v'v''}$. The B state, however, significantly deviates from the diagonal starting around $v' = 4$ because of the second potential minimum at ~6 a_0 [Fig. 5.1(a)]. Note that $B(v' = 4)$ has comparable line strengths between $X(v'' = 0)$ and $X(v'' = 15)$. (c) Intensity-normalized Rabi rate ($\Omega/\sqrt{I} = \sqrt{S_{v'v''}}/\hbar$) for dipole transitions $X(v'' = 0) \rightarrow B(v')$ (red squares) and $B(v') \rightarrow X(v = 15)$ (blue circles). Around $v' = 4$ (shaded points), the Rabi rates are comparable. (d) Wavelengths in nanometers for optical transitions $X(v'' = 0) \rightarrow B(v')$ (blue circles) and $B(v') \rightarrow X$(continuum) (red squares). The theoretical energy differences were adjusted by a common offset of 240 cm^{-1} to match experimental data for $X(v'' = 0) \rightarrow B(v' = 0,\ 1,\ 2)$ transitions [108]. The wavelengths corresponding to $v' = 4$ (shaded points) are 512.7 nm and 1744.7 nm.

in computational quantum chemistry. This new platform will be invaluable for both applications here. As for now, the experiment is moving toward a direction that could be compatible with both applications at the same time.

References

[1] W. D. Phillips, "Nobel lecture: Laser cooling and trapping of neutral atoms," *Rev. Mod. Phys.*, vol. 70, pp. 721–741, 1998.

[2] M. S. Safronova, D. Budker, D. DeMille, D. F. J. Kimball, A. Derevianko, and C. W. Clark, "Search for new physics with atoms and molecules," *Rev. Mod. Phys.*, vol. 90, p. 025 008, 2018.

[3] A. D. Ludlow, M. M. Boyd, J. Ye, E. Peik, and P. O. Schmidt, "Optical atomic clocks," *Rev. Mod. Phys.*, vol. 87, pp. 637–701, 2015.

[4] M. Saffman, T. G. Walker, and K. Mølmer, "Quantum information with Rydberg atoms," *Rev. Mod. Phys.*, vol. 82, pp. 2313–2363, 2010.

[5] I. Bloch, J. Dalibard, and S. Nascimbène, "Quantum simulations with ultracold quantum gases," *Nat. Phys.*, vol. 8, pp. 267–276, 2012.

[6] The ACME Collaboration et al., "Order of magnitude smaller limit on the electric dipole moment of the electron," *Science*, vol. 343, pp. 269–272, 2014.

[7] V. Andreev et al., "Improved limit on the electric dipole moment of the electron," *Nature*, vol. 562, pp. 355–360, 2018.

[8] W. B. Cairncross et al., "Precision measurement of the electron's electric dipole moment using trapped molecular ions," *Phys. Rev. Lett.*, vol. 119, p. 153 001, 2017.

[9] T. S. Roussy et al., "An improved bound on the electron's electric dipole moment," *Science*, vol. 381, pp. 46–50, 2023.

[10] D. DeMille, J. M. Doyle, and A. O. Sushkov, "Probing the frontiers of particle physics with tabletop-scale experiments," *Science*, vol. 357, pp. 990–994, 2017.

[11] C. Cesarotti, Q. Lu, Y. Nakai, A. Parikh, and M. Reece, "Interpreting the electron EDM constraint," *J. High Energy Phys.*, vol. 2019, p. 59, 2019.

[12] B. C. Regan, E. D. Commins, C. J. Schmidt, and D. DeMille, "New limit on the electron electric dipole moment," *Phys. Rev. Lett.*, vol. 88, p. 071 805, 2002.

[13] R. H. Parker et al., "First measurement of the atomic electric dipole moment of ^{225}Ra," *Phys. Rev. Lett.*, vol. 114, p. 233 002, 2015.

[14] B. Graner, Y. Chen, E. G. Lindahl, and B. R. Heckel, "Reduced limit on the permanent electric dipole moment of ^{199}Hg," *Phys. Rev. Lett.*, vol. 116, p. 161 601, 2016.

[15] D. DeMille, S. Sainis, J. Sage, T. Bergeman, S. Kotochigova, and E. Tiesinga, "Enhanced sensitivity to variation of m_e/m_p in molecular spectra," *Phys. Rev. Lett.*, vol. 100, p. 043 202, 2008.

[16] I. Kozyryev, Z. Lasner, and J. M. Doyle, "Enhanced sensitivity to ultralight bosonic dark matter in the spectra of the linear radical SrOH," *Phys. Rev. A*, vol. 103, p. 043 313, 2021.

[17] P. W. Graham, D. E. Kaplan, and S. Rajendran, "Cosmological relaxation of the electroweak scale," *Phys. Rev. Lett.*, vol. 115, p. 221 801, 2015.

[18] J. P. Gordon, H. J. Zeiger, and C. H. Townes, "The maser—new type of microwave amplifier, frequency standard, and spectrometer," *Phys. Rev.*, vol. 99, pp. 1264–1274, 1955.

[19] K. H. Leung et al., "Terahertz vibrational molecular clock with systematic uncertainty at the 10^{-14} level," *Phys. Rev. X*, vol. 13, p. 011 047, 2023.

[20] E. Tiberi, M. Borkowski, B. Iritani, R. Moszynski, and T. Zelevinsky, "Searching for new fundamental interactions via isotopic shifts in molecular lattice clocks," *Phys. Rev. Res.*, vol. 6, p. 033 013, 2024.

[21] Y. Liu and K.-K. Ni, "Bimolecular chemistry in the ultracold regime," *Annu. Rev. Phys. Chem.*, vol. 73, pp. 73–96, 2022.

[22] R. Bause, A. Christianen, A. Schindewolf, I. Bloch, and X.-Y. Luo, "Ultracold sticky collisions: Theoretical and experimental status," *J. Phys. Chem. A*, vol. 127, pp. 729–741, 2023.

[23] Y.-X. Liu et al., "Quantum interference in atom-exchange reactions," *Science*, vol. 384, pp. 1117–1121, 2024.

[24] Y.-X. Liu et al., "Hyperfine-to-rotational energy transfer in ultracold atom–molecule collisions of Rb and KRb," *Nat. Chem.*, vol. 17, pp. 688–694, 2025.

[25] J. Lim, M. D. Frye, J. M. Hutson, and M. R. Tarbutt, "Modeling sympathetic cooling of molecules by ultracold atoms," *Phys. Rev. A*, vol. 92, p. 053 419, 2015.

[26] T. V. Tscherbul and J. Kłos, "Magnetic tuning of ultracold barrierless chemical reactions," *Phys. Rev. Res.*, vol. 2, p. 013 117, 2020.

[27] B. Gadway and B. Yan, "Strongly interacting ultracold polar molecules," *J. Phys. B: At. Mol. Opt. Phys.*, vol. 49, p. 152 002, 2016.

[28] A. Micheli, G. K. Brennen, and P. Zoller, "A toolbox for lattice-spin models with polar molecules," *Nat. Phys.*, vol. 2, pp. 341–347, 2006.

[29] N. Y. Yao et al., "Topological flat bands from dipolar spin systems," *Phys. Rev. Lett.*, vol. 109, p. 266 804, 2012.

[30] B. Capogrosso-Sansone, C. Trefzger, M. Lewenstein, P. Zoller, and G. Pupillo, "Quantum phases of cold polar molecules in 2D optical lattices," *Phys. Rev. Lett.*, vol. 104, p. 125 301, 2010.

[31] D. DeMille, "Quantum computation with trapped polar molecules," *Phys. Rev. Lett.*, vol. 88, p. 067 901, 2002.

[32] J. A. Blackmore et al., "Ultracold molecules for quantum simulation: Rotational coherences in CaF and RbCs," *Quantum Sci. Technol.*, vol. 4, p. 014 010, 2018.

[33] C. M. Holland, Y. Lu, and L. W. Cheuk, "On-demand entanglement of molecules in a reconfigurable optical tweezer array," *Science*, vol. 382, pp. 1143–1147, 2023.

[34] Y. Bao et al., "Dipolar spin-exchange and entanglement between molecules in an optical tweezer array," *Science*, vol. 382, pp. 1138–1143, 2023.

[35] L. R. B. Picard et al., "Entanglement and iSWAP gate between molecular qubits," *Nature*, vol. 637, pp. 821–826, 2025.

[36] D. K. Ruttley, T. R. Hepworth, A. Guttridge, and S. L. Cornish, "Long-lived entanglement of molecules in magic-wavelength optical tweezers," *Nature*, vol. 637, pp. 827–832, 2025.

[37] Y. Lu, S. J. Li, C. M. Holland, and L. W. Cheuk, "Raman sideband cooling of molecules in an optical tweezer array," *Nat. Phys.*, vol. 20, pp. 389–394, 2024.

[38] Y. Bao et al., "Raman sideband cooling of molecules in an optical tweezer array to the 3D motional ground state," *Phys. Rev. X*, vol. 14, p. 031 002, 2024.

[39] K.-K. Ni et al., "A high phase-space-density gas of polar molecules," *Science*, vol. 322, pp. 231–235, 2008.

[40] P. K. Molony et al., "Creation of ultracold $^{87}Rb^{133}Cs$ molecules in the rovibrational ground state," *Phys. Rev. Lett.*, vol. 113, p. 255 301, 2014.

[41] J. W. Park, S. A. Will, and M. W. Zwierlein, "Ultracold dipolar gas of fermionic $^{23}Na^{40}K$ molecules in their absolute ground state," *Phys. Rev. Lett.*, vol. 114, p. 205 302, 2015.

[42] M. Guo et al., "Creation of an ultracold gas of ground-state dipolar $^{23}Na^{87}Rb$ molecules," *Phys. Rev. Lett.*, vol. 116, p. 205 303, 2016.

[43] T. M. Rvachov et al., "Long-lived ultracold molecules with electric and magnetic dipole moments," *Phys. Rev. Lett.*, vol. 119, p. 143 001, 2017.

[44] I. Stevenson et al., "Ultracold gas of dipolar NaCs ground state molecules," *Phys. Rev. Lett.*, vol. 130, p. 113 002, 2023.

[45] C. He et al., "Efficient creation of ultracold ground state ^{6}Li^{40}K polar molecules," *Phys. Rev. Lett.*, vol. 132, p. 243 401, 2024.

[46] L. D. Marco, G. Valtolina, K. Matsuda, W. G. Tobias, J. P. Covey, and J. Ye, "A degenerate Fermi gas of polar molecules," *Science*, vol. 363, pp. 853–856, 2019.

[47] A. Schindewolf et al., "Evaporation of microwave-shielded polar molecules to quantum degeneracy," *Nature*, vol. 607, pp. 677–681, 2022.

[48] N. Bigagli et al., "Observation of Bose–Einstein condensation of dipolar molecules," *Nature*, vol. 631, pp. 289–293, 2024.

[49] S. Zhang et al., "Observation of self-bound droplets of ultracold dipolar molecules," *Nature*, vol. 651, pp. 601–606, 2026.

[50] K. H. Leung, E Tiberi, B Iritani, I Majewska, R Moszynski, and T Zelevinsky, "Ultracold $^{88}Sr_2$ molecules in the absolute ground state," *New J. Phys.*, vol. 23, p. 115 002, 2021.

[51] D. K. Ruttley et al., "Formation of ultracold molecules by merging optical tweezers," *Phys. Rev. Lett.*, vol. 130, p. 223 401, 2023.

[52] N. R. Hutzler, H.-I. Lu, and J. M. Doyle, "The buffer gas beam: An intense, cold, and slow source for atoms and molecules," *Chem. Rev.*, vol. 112, pp. 4803–4827, 2012.

[53] H. L. Bethlem, G. Berden, and G. Meijer, "Decelerating neutral dipolar molecules," *Phys. Rev. Lett.*, vol. 83, pp. 1558–1561, 1999.

[54] A. Osterwalder, S. A. Meek, G. Hammer, H. Haak, and G. Meijer, "Deceleration of neutral molecules in macroscopic traveling traps," *Phys. Rev. A*, vol. 81, p. 051 401, 2010.

[55] H.-I. Lu, I. Kozyryev, B. Hemmerling, J. Piskorski, and J. M. Doyle, "Magnetic trapping of molecules via optical loading and magnetic slowing," *Phys. Rev. Lett.*, vol. 112, p. 113 006, 2014.

[56] B. L. Augenbraun et al., "Zeeman-Sisyphus deceleration of molecular beams," *Phys. Rev. Lett.*, vol. 127, p. 263 002, 2021.

[57] H. Sawaoka et al., "Zeeman-Sisyphus deceleration for heavy molecules with perturbed excited-state structure," *Phys. Rev. A*, vol. 107, p. 022 810, 2023.

[58] S. Chervenkov et al., "Continuous centrifuge decelerator for polar molecules," *Phys. Rev. Lett.*, vol. 112, p. 013 001, 2014.

[59] X. Wu, T. Gantner, M. Koller, M. Zeppenfeld, S. Chervenkov, and G. Rempe, "A cryofuge for cold-collision experiments with slow polar molecules," *Science*, vol. 358, pp. 645–648, 2017.

[60] M. Zeppenfeld et al., "Sisyphus cooling of electrically trapped polyatomic molecules," *Nature*, vol. 491, pp. 570–573, 2012.

[61] E. S. Shuman, J. F. Barry, and D. DeMille, "Laser cooling of a diatomic molecule," *Nature*, vol. 467, pp. 820–823, 2010.

[62] M. T. Hummon, M. Yeo, B. K. Stuhl, A. L. Collopy, Y. Xia, and J. Ye, "2D magneto-optical trapping of diatomic molecules," *Phys. Rev. Lett.*, vol. 110, p. 143 001, 2013.

[63] E. Chae et al., "One-dimensional magneto-optical compression of a cold CaF molecular beam," *New J. Phys.*, vol. 19, p. 033 035, 2017.

[64] J. Lim et al., "Laser cooled YbF molecules for measuring the electron's electric dipole moment," *Phys. Rev. Lett.*, vol. 120, p. 123 201, 2018.

[65] R. L. McNally, I. Kozyryev, S. Vazquez-Carson, K. Wenz, T. Wang, and T. Zelevinsky, "Optical cycling, radiative deflection and laser cooling of barium monohydride (^{138}Ba^{1}H)," *New J. Phys.*, vol. 22, p. 083 047, 2020.

[66] S. F. Vázquez-Carson, Q. Sun, J. Dai, D. Mitra, and T. Zelevinsky, "Direct laser cooling of calcium monohydride molecules," *New J. Phys.*, vol. 24, p. 083 006, 2022.

[67] J. Dai, Q. Sun, B. C. Riley, D. Mitra, and T. Zelevinsky, "Laser cooling of a fermionic molecule," *Phys. Rev. Res.*, vol. 6, p. 033 135, 2024.

[68] Y. Zhang, Z. Zeng, Q. Liang, W. Bu, and B. Yan, "Doppler cooling of buffer-gas-cooled barium monofluoride molecules," *Phys. Rev. A*, vol. 105, p. 033 307, 2022.

[69] M. Rockenhäuser, F. Kogel, T. Garg, S. A. Morales-Ramírez, and T. Langen, "Laser cooling of barium monofluoride molecules using synthesized optical spectra," *Phys. Rev. Res.*, vol. 6, p. 043 161, 2024.

[70] I. Kozyryev et al., "Sisyphus laser cooling of a polyatomic molecule," *Phys. Rev. Lett.*, vol. 118, p. 173 201, 2017.

[71] B. L. Augenbraun et al., "Laser-cooled polyatomic molecules for improved electron electric dipole moment searches," *New J. Phys.*, vol. 22, p. 022 003, 2020.

[72] L. Baum et al., "1D magneto-optical trap of polyatomic molecules," *Phys. Rev. Lett.*, vol. 124, p. 133 201, 2020.

[73] D. Mitra et al., "Direct laser cooling of a symmetric top molecule," *Science*, vol. 369, pp. 1366–1369, 2020.

[74] J. F. Barry, D. J. McCarron, E. B. Norrgard, M. H. Steinecker, and D. DeMille, "Magneto-optical trapping of a diatomic molecule," *Nature*, vol. 512, pp. 286–289, 2014.

[75] L. Anderegg et al., "Radio frequency magneto-optical trapping of CaF with high density," *Phys. Rev. Lett.*, vol. 119, p. 103 201, 2017.

[76] A. L. Collopy et al., "3D magneto-optical trap of yttrium monoxide," *Phys. Rev. Lett.*, vol. 121, p. 213 201, 2018.

[77] N. B. Vilas et al., "Magneto-optical trapping and sub-Doppler cooling of a polyatomic molecule," *Nature*, vol. 606, pp. 70–74, 2022.

[78] Z. Zeng, S. Deng, S. Yang, and B. Yan, "Three-dimensional magneto-optical trapping of barium monofluoride," *Phys. Rev. Lett.*, vol. 133, p. 143 404, 2024.

[79] Z. D. Lasner et al., "Magneto-optical trapping of a heavy polyatomic molecule for precision measurement," *Phys. Rev. Lett.*, vol. 134, p. 083 401, 2025.

[80] J. E. Padilla-Castillo et al., "Magneto-optical trapping of aluminum monofluoride," *Phys. Rev. Lett.*, vol. 135, p. 243 401, 2025.

[81] J. Dai, B. Riley, Q. Sun, D. Mitra, and T. Zelevinsky, "Magneto-optical trapping of a metal hydride molecule," *arXiv:2512.22350*, 2025.

[82] J. J. McClelland, A. V. Steele, B. Knuffman, K. A. Twedt, A. Schwarzkopf, and T. M. Wilson, "Bright focused ion beam sources based on laser-cooled atoms," *Appl. Phys. Rev.*, vol. 3, p. 011 302, 2016.

[83] C. J. Baker et al., "Laser cooling of antihydrogen atoms," *Nature*, vol. 592, pp. 35–42, 2021.

[84] S. F. Cooper, C Rasor, R. G. Bullis, A. D. Brandt, and D. C. Yost, "Optical deceleration of atomic hydrogen," *New J. Phys.*, vol. 25, p. 093 038, 2023.

[85] N. Bohr, "I. On the constitution of atoms and molecules," *Philos. Mag.*, vol. 26, pp. 1–25, 1913.

[86] W. E. Lamb and R. C. Retherford, "Fine structure of the hydrogen atom by a microwave method," *Phys. Rev.*, vol. 72, pp. 241–243, 1947.

[87] P. J. Mohr, D. B. Newell, B. N. Taylor, and E. Tiesinga, "CODATA recommended values of the fundamental physical constants: 2022," *Rev. Mod. Phys.*, vol. 97, p. 025 002, 2025.

[88] C. L. Cesar et al., "Two-photon spectroscopy of trapped atomic hydrogen," *Phys. Rev. Lett.*, vol. 77, pp. 255–258, 1996.

[89] C. G. Parthey et al., "Improved measurement of the hydrogen 1*S*–2*S* transition frequency," *Phys. Rev. Lett.*, vol. 107, p. 203 001, 2011.

[90] A. Beyer et al., "The Rydberg constant and proton size from atomic hydrogen," *Science*, vol. 358, pp. 79–85, 2017.

[91] N. Bezginov, T. Valdez, M. Horbatsch, A. Marsman, A. C. Vutha, and E. A. Hessels, "A measurement of the atomic hydrogen Lamb shift and the proton charge radius," *Science*, vol. 365, pp. 1007–1012, 2019.

[92] A. Grinin et al., "Two-photon frequency comb spectroscopy of atomic hydrogen," *Science*, vol. 370, pp. 1061–1066, 2020.

[93] A. D. Brandt, S. F. Cooper, C. Rasor, Z. Burkley, A. Matveev, and D. C. Yost, "Measurement of the $2S_{1/2} - 8D_{5/2}$ transition in hydrogen," *Phys. Rev. Lett.*, vol. 128, p. 023 001, 2022.

[94] L. Maisenbacher et al., "Sub-part-per-trillion test of the Standard Model with atomic hydrogen," *Nature*, vol. 650, pp. 845–851, 2026.

[95] R. G. Bullis et al., "Precision spectroscopy of 2S-nS transitions in atomic hydrogen: A determination of the proton charge radius," *Phys. Rev. Lett.*, vol. 136, p. 123 001, 2026.

[96] D. G. Fried et al., "Bose-Einstein condensation of atomic hydrogen," *Phys. Rev. Lett.*, vol. 81, pp. 3811–3814, 1998.

[97] Q. Sun et al., "Probing the limits of optical cycling in a predissociative diatomic molecule," *Phys. Rev. Res.*, vol. 5, p. 043 070, 2023.

[98] Q. Sun et al., "Chemistry in a cryogenic buffer gas cell," *J. Phys. Chem. Lett.*, vol. 17, pp. 640–646, 2026.

[99] I. C. Lane, "Production of ultracold hydrogen and deuterium via Doppler-cooled Feshbach molecules," *Phys. Rev. A*, vol. 92, p. 022 511, 2015.

[100] S Hofsäss et al., "Optical cycling of AlF molecules," *New J. Phys.*, vol. 23, p. 075 001, 2021.

[101] J. R. Daniel et al., "Hyperfine structure of the $A^1\Pi$ state of AlCl and its relevance to laser cooling and trapping," *Phys. Rev. A*, vol. 108, p. 062 821, 2023.

[102] N. H. Pilgram, B. W. Baldwin, D. S. La Mantia, S. P. Eckel, and E. B. Norrgard, "Spectroscopy of laser-cooling transitions in MgF," *Phys. Rev. A*, vol. 110, p. 023 110, 2024.

[103] K. Kwon, S. Roh, Y. Cho, Y. Lee, and E. Chae, "Optical cycling of MgF molecules within the hyperfine states in X(N=1) state," *Sci. Rep.*, vol. 16, p. 102, 2025.

[104] J. F. Barry, "Laser cooling and slowing of a diatomic molecule," Ph.D. dissertation, Yale University, 2013.

[105] J. M. Brown and A. Carrington, *Rotational Spectroscopy of Diatomic Molecules*. Cambridge University Press, 2003.

[106] M. Liu, T. Pauchard, M. Sjödin, O. Launila, P. van der Meulen, and L.-E. Berg, "Time-resolved study of the $A^2\Pi$ state of CaH by laser spectroscopy," *J. Mol. Spectrosc.*, vol. 257, pp. 105–107, 2009.

[107] L.-E. Berg, K. Ekvall, and S. Kelly, "Radiative lifetime measurement of vibronic levels of the $B^2\Sigma^+$ state of CaH by laser excitation spectroscopy," *Chem. Phys. Lett.*, vol. 257, pp. 351–355, 1996.

[108] A. Shayesteh, R. S. Ram, and P. F. Bernath, "Fourier transform emission spectra of the $A^2\Pi \rightarrow X^2\Sigma^+$ and $B^2\Sigma^+ \rightarrow X^2\Sigma^+$ band systems of CaH," *J. Mol. Spectrosc.*, vol. 288, pp. 46–51, 2013.

[109] Y. Gao and T. Gao, "Laser cooling of the alkaline-earth-metal monohydrides: Insights from an *ab initio* theory study," *Phys. Rev. A*, vol. 90, p. 052 506, 2014.

[110] M. Ramanaiah and S. Lakshman, "True potential energy curves and Franck-Condon factors of a few alkaline earth hydrides," *Physica B+C*, vol. 113, pp. 263–270, 1982.

[111] G. Z. Iwata, "A cryogenic buffer-gas cooled beam of barium monohydride for laser slowing, cooling, and trapping," Ph.D. dissertation, Columbia University, 2018.

[112] Y. Bao, "Ultracold molecules in an optical tweezer array: From dipolar interaction to ground state cooling," Ph.D. dissertation, Harvard University, 2024.

[113] J. F. Barry, E. S. Shuman, and D. DeMille, "A bright, slow cryogenic molecular beam source for free radicals," *Phys. Chem. Chem. Phys.*, vol. 13, pp. 18 936–18 947, 2011.

[114] N. E. Bulleid, S. M. Skoff, R. J. Hendricks, B. E. Sauer, E. A. Hinds, and M. R. Tarbutt, "Characterization of a cryogenic beam source for atoms and molecules," *Phys. Chem. Chem. Phys.*, vol. 15, pp. 12 299–12 307, 2013.

[115] V. Jorapur, "Towards a Bose-Einstein condensate of SrF molecules," Ph.D. dissertation, Yale University, 2024.

[116] H.-I. Lu, J. Rasmussen, M. J. Wright, D. Patterson, and J. M. Doyle, "A cold and slow molecular beam," *Phys. Chem. Chem. Phys.*, vol. 13, pp. 18 986–18 990, 2011.

[117] H.-I. Lu, "Magnetic trapping of molecules via optical loading and magnetic slowing," Ph.D. dissertation, Harvard University, 2013.

[118] N. Vilas, "Laser cooling, optical trapping, and quantum control of polyatomic molecules," Ph.D. dissertation, Harvard University, 2025.

[119] S. Truppe et al., "A buffer gas beam source for short, intense and slow molecular pulses," *J. Mod. Opt.*, vol. 65, pp. 648–656, 2018.

[120] X. Liu et al., "The chemistry of AlF and CaF production in buffer gas sources," *J. Chem. Phys.*, vol. 157, p. 074 305, 2022.

[121] X. Zhao, X. Xu, and H. Xu, "High-temperature non-equilibrium atom–diatom collisional energy transfer," *J. Chem. Phys.*, vol. 161, p. 231 101, 2024.

[122] D. G. Truhlar and J. T. Muckerman, "Reactive scattering cross sections III: Quasiclassical and semiclassical methods," in *Atom-molecule collision theory: A guide for the experimentalist*, Plenum Press, New York, 1979, pp. 505 –561.

[123] J. Pérez-Ríos, "Cold chemical reactions between molecular ions and neutral atoms," in *An introduction to cold and ultracold chemistry: Atoms, molecules, ions and Rydbergs*, Springer International Publishing, 2020, pp. 215 –234.

[124] R. Koots and J. Pérez-Ríos, "PyQCAMS: Python quasi-classical atom-molecule scattering," *Atoms*, vol. 12, p. 5, 2024.

[125] R. Koots, "Classical and semiclassical dynamics of few body systems," Ph.D. dissertation, Stony Brook University, 2025.

[126] S. M. Skoff et al., "Diffusion, thermalization, and optical pumping of YbF molecules in a cold buffer-gas cell," *Phys. Rev. A*, vol. 83, p. 023 418, 2011.

[127] P. C. Souers, C. K. Briggs, J. W. Pyper, and R. T. Tsugawa, "Hydrogen vapor pressures from 4 to 30 K: A review," Lawrence Livermore Laboratory, Report UCRL-52226, 1977.

[128] H. J. Hoge and R. D. Arnold, "Vapor pressures of hydrogen, deuterium, and hydrogen deuteride and dew-point pressures of their mixtures," *J. Res. Natl. Bur. Stand.*, vol. 47, p. 2, 1951.

[129] R. McNally, "Laser cooling of BaH molecules, and new ideas for the detection of dark matter," Ph.D. dissertation, Columbia University, 2021.

[130] R. J. Hendricks, D. A. Holland, S. Truppe, B. E. Sauer, and M. R. Tarbutt, "Vibrational branching ratios and hyperfine structure of ^{11}BH and its suitability for laser cooling," *Front. Phys.*, vol. 2, 2014.

[131] E. B. Norrgard, D. J. McCarron, M. H. Steinecker, M. R. Tarbutt, and D. DeMille, "Submillikelvin dipolar molecules in a radio-frequency magneto-optical trap," *Phys. Rev. Lett.*, vol. 116, p. 063 004, 2016.

[132] O. Emile, R. Kaiser, C. Gerz, H. Wallis, A. Aspect, and C. Cohen-Tannoudji, "Magnetically assisted Sisyphus effect," *J. Phys. II France*, vol. 3, pp. 1709–1733, 1993.

[133] B. Sheehy, S.-Q. Shang, P. van der Straten, S. Hatamian, and H. Metcalf, "Magnetic-field-induced laser cooling below the Doppler limit," *Phys. Rev. Lett.*, vol. 64, pp. 858–861, 1990.

[134] M. Zeppenfeld et al., "Sisyphus cooling of electrically trapped polyatomic molecules," *Nature*, vol. 491, pp. 570–573, 2012.

[135] J. A. Devlin and M. R. Tarbutt, "Three-dimensional Doppler, polarization-gradient, and magneto-optical forces for atoms and molecules with dark states," *New J. Phys.*, vol. 18, p. 123 017, 2016.

[136] J. A. Devlin and M. R. Tarbutt, "Laser cooling and magneto-optical trapping of molecules analyzed using optical Bloch equations and the Fokker-Planck-Kramers equation," *Phys. Rev. A*, vol. 98, p. 063 415, 2018.

[137] Q. Sun, "From laser cooled molecules to novel quantum matter," Ph.D. dissertation, Columbia University, 2025.

[138] G. Herzberg, *Molecular Spectra and Molecular Structure, I. Spectra of Diatomic Molecules*. D.Van Nostrand Company Inc., 1950.

[139] W. Demtröder, *Mol. Phys.* John Wiley & Sons, Ltd, 2005.

[140] J. von Neumann and E. Wigner, "Uber merkwürdige diskrete eigenwerte. uber das verhalten von eigenwerten bei adiabatischen prozessen," *Phys. Z.*, vol. 30, p. 467, 1929.

[141] E. Teller, "The crossing of potential surfaces.," *J. Phys. Chem.*, vol. 41, pp. 109–116, 1937.

[142] C. A. Mead, "The "noncrossing" rule for electronic potential energy surfaces: The role of time-reversal invariance," *J. Chem. Phys.*, vol. 70, pp. 2276–2283, 1979.

[143] C. E. Dickerson, "Designing molecules for quantum technology," Ph.D. dissertation, University of California, Los Angeles, 2024.

[144] P. K. H-J. Werner et al., "Molpro, version 2022.3, a package of ab initio programs, see https://www.molpro.net," 2022.

[145] H.-J. Werner, P. J. Knowles, G. Knizia, F. R. Manby, and M. Schütz, "Molpro: A general-purpose quantum chemistry program package," *WIREs Comput. Mol. Sci*, vol. 2, pp. 242–253, 2012.

[146] H.-J. Werner et al., "The Molpro quantum chemistry package," *J. Chem. Phys.*, vol. 152, p. 144 107, 2020.

[147] A. Shayesteh, S. F. Alavi, M. Rahman, and E. Gharib-Nezhad, "Ab initio transition dipole moments and potential energy curves for the low-lying electronic states of CaH," *Chem. Phys. Lett.*, vol. 667, pp. 345–350, 2017.

[148] J. Koput and K. A. Peterson, "Ab initio potential energy surface and vibrational-rotational energy levels of $X^2\Sigma^+$ CaOH," *J. Phys. Chem. A*, vol. 106, pp. 9595–9599, 2002.

[149] T. H. Dunning Jr, "Gaussian basis sets for use in correlated molecular calculations. I. The atoms boron through neon and hydrogen," *J. Chem. Phys.*, vol. 90, pp. 1007–1023, 1989.

[150] P. J. Knowles and H.-J. Werner, "An efficient second-order MC SCF method for long configuration expansions," *Chem. Phys. Lett.*, vol. 115, pp. 259–267, 1985.

[151] H.-J. Werner and P. J. Knowles, "An efficient internally contracted multiconfiguration–reference configuration interaction method," *J. Chem. Phys.*, vol. 89, pp. 5803–5814, 1988.

[152] P. J. Knowles and H.-J. Werner, "Internally contracted multiconfiguration-reference configuration interaction calculations for excited states," *Theor. Chim. Acta.*, vol. 84, pp. 95–103, 1992.

[153] K. Shamasundar, G. Knizia, and H.-J. Werner, "A new internally contracted multi-reference configuration interaction method," *J. Chem. Phys.*, vol. 135, p. 054 101, 2011.

[154] A. Berning, M. Schweizer, H.-J. Werner, P. J. Knowles, and P. Palmieri, "Spin-orbit matrix elements for internally contracted multireference configuration interaction wavefunctions," *Mol. Phys.*, vol. 98, pp. 1823–1833, 2000.

[155] D. T. Colbert and W. H. Miller, "A novel discrete variable representation for quantum mechanical reactive scattering via the S-matrix kohn method," *J. Chem. Phys.*, vol. 96, pp. 1982–1991, 1992.

[156] T. Busch, A. D. Esposti, and H.-J. Werner, "Analytical energy gradients for multiconfiguration self-consistent field wave functions with frozen core orbitals," *J. Chem. Phys.*, vol. 94, pp. 6708–6715, 1991.

[157] R. Baer, *Electron density functional theory*. Fritz Haber Center for Molecular Dynamics, 2016.

[158] D. Neuhauser and M. Baer, "The application of wave packets to reactive atom-diatom systems: A new approach," *J. Chem. Phys.*, vol. 91, pp. 4651–4657, 1989.

[159] D. Neuhauser, "State-to-state reactive scattering amplitudes from single-arrangement propagation with absorbing potentials," *J. Chem. Phys.*, vol. 93, pp. 7836–7842, 1990.

[160] D. Neuhauser, "Molecular scattering: Very-short-range imaginary potentials, absorbing-potentials, and flux-amplitude expressions," *J. Chem. Phys.*, vol. 103, pp. 8513–8527, 1995.

[161] D. Neuhasuer and M. Baer, "The time-dependent Schrödinger equation: Application of absorbing boundary conditions," *J. Chem. Phys.*, vol. 90, pp. 4351–4355, 1989.

[162] B. Efron, "Bootstrap methods: Another look at the jackknife," *Ann. Statist.*, vol. 7, pp. 1–26, 1979.

[163] B. Efron and R. J. Tibshirani, *An Introduction to the Bootstrap*. Chapman & Hall/CRC, 1993.

[164] A. C. Davison and D. V. Hinkley, *Bootstrap Methods and their Application*. Cambridge University Press, 1997.

[165] C. M. Holland, Y. Lu, and L. W. Cheuk, "Synthesizing optical spectra using computer-generated holography techniques," *New J. Phys.*, vol. 23, p. 033 028, 2021.

[166] B. Hemmerling et al., "Laser slowing of CaF molecules to near the capture velocity of a molecular MOT," *J. Phys. B: At. Mol. Opt. Phys.*, vol. 49, p. 174 001, 2016.

[167] J. F. Barry, E. S. Shuman, E. B. Norrgard, and D. DeMille, "Laser radiation pressure slowing of a molecular beam," *Phys. Rev. Lett.*, vol. 108, p. 103 002, 2012.

[168] G. Li, J. J. Harrison, R. S. Ram, C. M. Western, and P. F. Bernath, "Einstein A coefficients and absolute line intensities for the $E^2\Pi$–$X^2\Sigma^+$ transition of CaH," *J. Quant. Spectrosc. Radiat. Transf.*, vol. 113, pp. 67–74, 2012.

[169] M. D. Di Rosa, "Laser-cooling molecules," *Eur. Phys. J. D*, vol. 31, pp. 395–402, 2004.

[170] P Kaebert et al., "Characterizing the Zeeman slowing force for $^{40}Ca^{19}F$ molecules," *New J. Phys.*, vol. 23, p. 093 013, 2021.

[171] S Truppe et al., "Molecules cooled below the Doppler limit," *Nat. Phys.*, vol. 13, pp. 1173–1176, 2017.

[172] L. Anderegg et al., "Laser cooling of optically trapped molecules," *Nat. Phys.*, vol. 14, pp. 890–893, 2018.

[173] J. J. Burau, P. Aggarwal, K. Mehling, and J. Ye, "Blue-detuned magneto-optical trap of molecules," *Phys. Rev. Lett.*, vol. 130, p. 193 401, 2023.

[174] V. Jorapur, T. K. Langin, Q. Wang, G. Zheng, and D. DeMille, "High density loading and collisional loss of laser-cooled molecules in an optical trap," *Phys. Rev. Lett.*, vol. 132, p. 163 403, 2024.

[175] S. J. Li, C. M. Holland, Y. Lu, and L. W. Cheuk, "Blue-detuned magneto-optical trap of CaF molecules," *Phys. Rev. Lett.*, vol. 132, p. 233 402, 2024.

[176] C. Hallas, G. K. Li, N. B. Vilas, P. Robichaud, L. Anderegg, and J. M. Doyle, "High compression blue-detuned magneto-optical trap of polyatomic molecules," *Phys. Rev. Lett.*, vol. 136, p. 133 402, 2026.

[177] S. S. Yu et al., "A conveyor-belt magneto-optical trap of CaF," *Nat. Commun.*, vol. 17, p. 1175, 2026.

[178] Z. Zeng, S. Yang, S. Deng, and B. Yan, "Direct loading of BaF molecules with a conveyor-belt magneto-optical trap," *Phys. Rev. Lett.*, vol. 136, p. 073 402, 2026.

[179] A. Jadbabaie, N. H. Pilgram, J. Kłos, S. Kotochigova, and N. R. Hutzler, "Enhanced molecular yield from a cryogenic buffer gas beam source via excited state chemistry," *New J. Phys.*, vol. 22, p. 022 002, 2020.

[180] N. Mukherjee, W. E. Perreault, and R. N. Zare, "Stark-induced adiabatic Raman ladder for preparing highly vibrationally excited quantum states of molecular hydrogen," *J. Phys. B: At. Mol. Opt. Phys.*, vol. 50, p. 144 005, 2017.

[181] N. R. Cooper and G. V. Shlyapnikov, "Stable topological superfluid phase of ultracold polar fermionic molecules," *Phys. Rev. Lett.*, vol. 103, p. 155 302, 2009.

[182] E. B. Norrgard, D. S. Barker, S. Eckel, J. A. Fedchak, N. N. Klimov, and J. Scherschligt, "Nuclear-spin dependent parity violation in optically trapped polyatomic molecules," *Commun. Phys.*, vol. 2, p. 77, 2019.

[183] Y. Hao et al., "Nuclear spin-dependent parity-violating effects in light polyatomic molecules," *Phys. Rev. A*, vol. 102, p. 052 828, 2020.

[184] F. Kogel, M. Rockenhäuser, R. Albrecht, and T. Langen, "A laser cooling scheme for precision measurements using fermionic barium monofluoride (^{137}Ba^{19}F) molecules," *New J. Phys.*, vol. 23, p. 095 003, 2021.

[185] Y. Zeng, A. Jadbabaie, A. N. Patel, P. Yu, T. C. Steimle, and N. R. Hutzler, "Optical cycling in polyatomic molecules with complex hyperfine structure," *Phys. Rev. A*, vol. 108, p. 012 813, 2023.

[186] C. I. Frum, J. J. Oh, E. A. Cohen, and H. M. Pickett, "Rotational spectra of the $X^2\Sigma^+$ states of CaH and CaD," *Astrophys. J.*, vol. 408, pp. L61–L64, 1993.

[187] E. GharibNezhad, A. Shayesteh, and P. Bernath, "Fourier transform emission spectra of the $A^2\Pi \rightarrow X^2\Sigma^+$ and $B^2\Sigma^+ \rightarrow X^2\Sigma^+$ transitions of CaD," *J. Mol. Spectrosc.*, vol. 281, pp. 47–50, 2012.

[188] S. F. Alavi and A. Shayesteh, "Einstein A coefficients for rovibronic lines of the $A^2\Pi \rightarrow X^2\Sigma^+$ and $B^2\Sigma^+ \rightarrow X^2\Sigma^+$ transitions of CaH and CaD," *Mon. Not. R. Astron. Soc.*, vol. 474, pp. 2–11, 2018.

[189] M. Boshier et al., "Precision spectroscopy of hydrogen and deuterium," *Nature*, vol. 330, pp. 463–465, 1987.

[190] R. Pohl et al., "Laser spectroscopy of muonic deuterium," *Science*, vol. 353, pp. 669–673, 2016.

[191] R. M. Potvliege, A. Nicolson, M. P. A. Jones, and M. Spannowsky, "Deuterium spectroscopy for enhanced bounds on physics beyond the standard model," *Phys. Rev. A*, vol. 108, p. 052 825, 2023.

[192] M. Zaghoo, T. R. Boehly, J. R. Rygg, P. M. Celliers, S. X. Hu, and G. W. Collins, "Breakdown of Fermi degeneracy in the simplest liquid metal," *Phys. Rev. Lett.*, vol. 122, p. 085 001, 2019.

[193] A. D. Bulanov, O. Y. Troshin, and V. V. Balabanov, "Synthesis of high-purity calcium hydride," *Russ. J. Appl. Chem.*, vol. 77, pp. 875–877, 2004.